Understanding the Dynamics of Radiation Belt Electrons by Means of Data Assimilation

JUAN SEBASTIÁN CERVANTES VILLA

Univ.-Diss.
zur Erlangung des akademischen Grades
"doctor rerum naturalium"
(Dr. rer. nat.)
in der Wissenschaftsdisziplin "Computational Physics"

eingereicht an der
Mathematisch-Naturwissenschaftlichen Fakultät
Institut für Physik und Astronomie
der Universität Potsdam
und
Deutsches GeoForschungsZentrum

30. August 2021

Unless otherwise indicated, this work is licensed under a Creative Commons License
Attribution 4.0 International.
This does not apply to quoted content and works based on other permissions.
To view a copy of this license visit:
https://creativecommons.org/licenses/by/4.0

Betreuer:

Prof. Dr. Yuri Shprits
Dr. Reiner Friedel

Gutachter*in:

Dr. Reiner Friedel
Dr. Drew Turner
Prof. Dr. Minna Palmroth

Published online on the
Publication Server of the University of Potsdam:
https://doi.org/10.25932/publishup-51982
https://nbn-resolving.org/urn:nbn:de:kobv:517-opus4-519827

Declaration

I, Juan Sebastián Cervantes Villa, declare that this thesis entitled, "Understanding the Dynamics of Radiation Belt Electrons by Means of Data Assimilation" and the work presented in it are my own. I confirm that:

- I have fully acknowledged and referenced the ideas and work of others.
- This dissertation has not been submitted for any other degree or qualification.
- I have acknowledged all main sources of help.

JUAN SEBASTIÁN CERVANTES VILLA

"Success is not final, failure is not fatal: it is the courage to continue that counts."

– Winston Churchill

Abstract

The Earth's electron radiation belts exhibit a two-zone structure, with the outer belt being highly dynamic due to the constant competition between a number of physical processes, including acceleration, loss, and transport. The flux of electrons in the outer belt can vary over several orders of magnitude, reaching levels that may disrupt satellite operations. Therefore, understanding the mechanisms that drive these variations is of high interest to the scientific community.

In particular, the important role played by loss mechanisms in controlling relativistic electron dynamics has become increasingly clear in recent years. It is now widely accepted that radiation belt electrons can be lost either by precipitation into the atmosphere or by transport across the magnetopause, called magnetopause shadowing. Precipitation of electrons occurs due to pitch-angle scattering by resonant interaction with various types of magnetospheric waves, including whistler mode chorus, plasmaspheric hiss, and electromagnetic ion cyclotron (EMIC) waves. In addition, the compression of the magnetopause due to increases in solar wind dynamic pressure can substantially deplete electrons at high L shells where they find themselves in open drift paths, whereas electrons at low L shells can be lost through outward radial diffusion. Nevertheless, the role played by each physical process during electron flux dropouts still remains a fundamental puzzle.

Differentiation between these processes and quantification of their relative contributions to the evolution of radiation belt electrons requires high-resolution profiles of phase space density (PSD). However, such profiles of PSD are difficult to obtain due to restrictions of spacecraft observations to a single measurement in space and time, which is also compounded by the inaccuracy of instruments. Data assimilation techniques aim to blend incomplete and inaccurate spaceborne data with physics-based models in an optimal way. In the Earth's radiation belts, it is used to reconstruct the entire radial profile of electron PSD, and it has become an increasingly important tool in validating our current understanding of radiation belt dynamics, identifying new physical processes, and predicting the near-Earth hazardous radiation environment.

In this study, sparse measurements from Van Allen Probes A and B and Geostationary Operational Environmental Satellites (GOES) 13 and 15 are assimilated into the three-dimensional Versatile Electron Radiation Belt (VERB-3D) diffusion model, by means of a split-operator Kalman filter over a four-year period from 01 October 2012 to 01 October 2016. In comparison to previous works, the 3D model accounts for more physical processes, namely mixed pitch angle-energy diffusion, scattering by EMIC waves, and magnetopause shadowing. It is shown how data assimilation, by means of the innovation vector, i.e. the residual between observations and model forecast, can be used to account for missing physics in the model. This method is used to identify the radial distances from the Earth and the geomagnetic conditions where the model is inconsistent with the measured PSD for different values of the adiabatic invariants μ and K. As a result, the Kalman filter adjusts the predictions in order to match the observations, and this is interpreted as evidence of where and when additional source or loss processes are active.

Furthermore, two distinct loss mechanisms responsible for the rapid dropouts of radiation belt electrons are investigated: EMIC wave-induced scattering and magnetopause shadowing. The innovation vector is inspected for values of the invariant μ ranging from 300 to 3000 MeV/G, and a statistical analysis is performed to quantitatively assess the effect of both processes as a function of various geomagnetic indices, solar wind parameters, and radial distance from the Earth. The results of this work are in agreement with previous studies that demonstrated the energy dependence of these two mechanisms. EMIC wave scattering dominates loss at lower L shells and it may amount to between 10%/hr to 30%/hr of the maximum value of PSD over all L shells for fixed first and second adiabatic invariants. On the other hand, magnetopause shadowing is found to deplete electrons across all energies, mostly at higher L shells, resulting in loss from 50%/hr to 70%/hr of the maximum PSD. Nevertheless, during times of enhanced geomagnetic activity, both processes can operate beyond such location and encompass the entire outer radiation belt.

The results of this study are two-fold. Firstly, it demonstrates that the 3D data assimilative code provides a comprehensive picture of the radiation belts and is an important step toward performing reanalysis using observations from current and future missions. Secondly, it achieves a better understanding and provides critical clues of the dominant loss mechanisms responsible for the rapid dropouts of electrons at different locations over the outer radiation belt.

Zusammenfassung

Die Elektronenstrahlungsgürtel der Erde weisen eine Zwei-Zonen-Struktur auf, wobei der äußere Gürtel aufgrund des ständigen Zusammenspiels zwischen einer Reihe von physikalischen Prozessen, einschließlich Beschleunigung, Verlust und Transport, eine hohe Dynamik aufweist. Der Elektronenfluss im äußeren Gürtel kann über mehrere Größenordnungen variieren und Werte erreichen, die den Satellitenbetrieb stören können. Daher ist das Verständnis der Mechanismen, die diese Variabilität bewirken, von hohem Interesse für die wissenschaftliche Gemeinschaft.

Insbesondere die wichtige Rolle die Verlustmechanismen bei der Kontrolle der relativistischen Elektronendynamik spielen ist in den letzten Jahren immer deutlicher geworden. Es ist inzwischen weithin anerkannt, dass Strahlungsgürtelelektronen entweder durch Interaktion mit der Atmosphäre oder durch Transport über die Magnetopause, das so genannte Magnetopauseshadowing, verloren gehen können. Der Verlust von Elektronen in der Atmosphäre erfolgt aufgrund von Pitchwinkelstreuung durch resonante Wechselwirkung mit verschiedenen Arten von magnetosphärischen Wellen, einschließlich plasmasphärischem Hiss, Whistler-Mode-Chorus, und elektromagnetischen Ionenzyklotron-Wellen (EMIC). Darüber hinaus kann die Komprimierung der Magnetopause aufgrund der Erhöhungen des dynamischen Drucks des Sonnenwindes dazu führen, dass Elektronen an hohen L-Shells, wo sie sich in offenen Driftpfaden befinden, erheblich in ihrer Dichte reduziert werden, während Elektronen an niedrigen L-Shells durch radiale Diffusion nach außen verloren gehen können. Nichtsdestotrotz bleibt die Rolle, die jeder physikalische Prozess bei der schnellen Reduktion des Elektronenflusses spielt, nach wie vor ein grundlegendes Rätsel.

Die Unterscheidung zwischen diesen Prozessen und die Quantifizierung ihrer relativen Beiträge zur Entwicklung der Strahlungsgürtelelektronen erfordert hochauflösende Profile der Phasenraumdichte (PSD). Solche Profile der PSD sind jedoch schwierig zu bestimmen, da die Beobachtungen von Raumfahrzeugen auf eine einzige Messung in Raum und Zeit beschränkt sind, was auch durch die Ungenauigkeit der Instrumente erschwert wird. Datenassimilationstechniken zielen darauf ab, unvollständige und ungenaue raumgestützte Daten mit physikalisch basierten Modellen auf optimale Weise zu kombinieren. In den Strahlungsgürteln der Erde werden sie verwendet, um das gesamte radiale Profil der Elektronen-PSD zu rekonstruieren, und sie sind zu einem immer wichtigeren Werkzeug geworden, um unser derzeitiges Verständnis der Dynamik der Strahlungsgürtel zu validieren, neue physikalische Prozesse zu identifizieren und die erdnahe gefährliche Strahlungsumgebung vorherzusagen.

In dieser Studie werden Messungen der Van-Allen-Probes A und B und der Geostationary-Operational-Environmental-Satellites (GOES) 13 und 15 mit Hilfe eines Split-Operator-Kalman-Filters über einen Zeitraum von vier Jahren vom 01. Oktober 2012 bis zum 01. Oktober 2016 in das dreidimensionale Versatile Electron Radiation Belt-3D-Diffusionsmodell (VERB-3D) integriert. Im Vergleich zu früheren Arbeiten berücksichtigt das 3D-Modell mehr physikalische Prozesse, nämlich gemischte Diffusion, Streuung durch EMIC-Wellen und Magnetopausenverluste. Es

wird gezeigt, wie die Datenassimilation mit Hilfe des Innovationsvektors, d.h. des Residuums zwischen Beobachtungen und Modellprognose, genutzt werden kann, um fehlende physikalische Prozesse im Modell zu berücksichtigen. Diese Methode wird verwendet, um die radialen Entfernungen von der Erde und die geomagnetischen Bedingungen zu identifizieren, bei denen unser Modell für verschiedene Werte der adiabatischen Invarianten μ und K nicht mit der gemessenen PSD übereinstimmt. Infolgedessen passt der Kalman-Filter die Vorhersagen an die Beobachtungen an, und dies wird als Nachweis dafür interpretiert, wo und wann zusätzliche Quellen- oder Verlustprozesse aktiv sind.

Darüber hinaus werden zwei unterschiedliche Verlustmechanismen untersucht, die für die schnellen Verluste von Strahlungsgürtelelektronen verantwortlich sind: EMIC-Wellen-induzierte Streuung und Magnetopausenverluste. Der Innovationsvektor wird bei Werten der Invariante μ im Bereich von 300 bis 3000 MeV/G untersucht, und es wird eine statistische Analyse durchgeführt, um die Wirkung beider Prozesse in Abhängigkeit von verschiedenen geomagnetischen Indizes, Sonnenwindparametern und der radialen Entfernung von der Erde quantitativ zu bewerten. Die Ergebnisse dieser Arbeit stehen in Übereinstimmung mit früheren Studien, die die Energieabhängigkeit dieser beiden Mechanismen nachgewiesen haben. Die EMIC-Wellenstreuung dominiert den Verlust bei niedrigen L-Shells und kann zwischen 10%/hr bis 30%/hr des Maximalwertes der PSD über alle L-Shells für feste Werte der ersten und zweiten adiabatische Invarianten betragen. Andererseits wird festgestellt, dass bei den Magnetopausenverlusten über alle Energien hinweg, meist bei höheren L-Shells, Elektronen Verluste zeigen, was zu einer Verstärkung des Verlustes von 50%/hr auf 70%/hr der maximalen PSD führt. Nichtsdestotrotz können beide Prozesse in Zeiten erhöhter geomagnetischer Aktivität über diese L-Shells hinaus wirken und den gesamten äußeren Strahlungsgürtel umfassen.

Die Ergebnisse dieser Studie sind zweifacher Art. Erstens zeigt sie, dass der 3D-Daten-Assimilationscode ein umfassendes Bild der Strahlungsgürtel liefert und ein wichtiger Schritt zur Durchführung einer Reanalyse unter Verwendung von Beobachtungen aus aktuellen und zukünftigen Missionen ist. Zweitens erreicht er ein besseres Verständnis und liefert entscheidende Hinweise auf die vorherrschenden Verlustmechanismen, die für die schnellen Verluste von Elektronen an verschiedenen Orten im äußeren Strahlungsgürtel verantwortlich sind.

Acknowledgements

First and foremost, I have to express my sincere appreciation to my supervisor, Prof. Yuri Shprits. Without his assistance and dedicated involvement, this work would have never been accomplished. I would like to thank him very much for his support and understanding over these past four years, and for steering me in the right direction whenever he thought I needed it. I am also grateful to my secondary supervisor, Prof. Reiner Friedel, for sharing expertise and for the continuous encouragement. I would also like to show gratitude to my committee, including Dr. Drew Turner, Prof. Minna Palmroth, Prof. Philipp Richter, and Prof. Claudia Stolle.

The Magnetospheric Physics section at GFZ has played the role of supporting colleagues and provided a base where I have enjoyed coming to work and felt welcomed and encouraged. I would especially like to acknowledge Hayley Allison, Dedong Wang, Nikita Aseev, Ingo Michaelis, Irina Zhelavskaya, Alexander Drozdov, Adam Kellerman, Frederic Effenberger, and Angelica Castillo for their numerous feedback and motivating discussions that helped me to broaden my horizon, and for the suggestions that led to significant improvements in the papers that we co-authored. I also wish to recognise Martina Krüger, Antje Timmermann, Sandra Paulin, Melanie Burns, Dominika Boneberg, and Alex Jordan for their invaluable administrative and technical assistance during all these times.

Getting through my dissertation required more than academic support, and I have many people to thank for listening to and, at times, having to tolerate me over the past four years. I must express my very profound gratitude to Toño and Sanja for providing me with unfailing support and continuous encouragement. This accomplishment would not have been possible without them. I also wish to acknowledge the support and great love of my family and my friends back home: Fernanda, Ivonne, Leire, Unai, Nancy, Thalia, Fer, Oscar, Jorge, Anthony, and Aaron. They kept me going on and I cannot express my gratitude and appreciation for their friendship. Thanks also to Eva, Jenny, Robin, Eduard, Stefan, and the ZUU crew for the much-needed sportive leisure.

Last, but not least, I would like to acknowledge the Deutsche Forschungsgemeinschaft (DFG) - SFB1294/1 - 318763901, for providing the funds necessary for the completion of my PhD. The SFB1294 "Data Assimilation" has been a source of insightful training for which I am grateful. Without their support and funding, this project could not have reached its goal.

I also place on record, my sense of gratitude to one and all, who directly or indirectly, have lent their hand in this venture.

Contents

List of Figures

List of Tables

List of Abbreviations

AE	Auroral electrojet index
CIR	Corotating interaction region
CME	Coronal mass ejection
CRAND	Cosmic ray albedo neutron decay
CRRES	Combined Release and Radiation Effects Satellite
DOB	Drift orbit bifurcation
Dst	Disturbance storm time index
ECT	Energetic Particle, Composition, and Thermal Plasma suite
EKF	Extended Kalman filter
ELF	Extremely low frequency (waves)
EnKF	Ensemble Kalman filter
EPEAD	Energetic Proton, Electron, and Alpha Detector
EPS	Energetic Particle Sensor
EMIC	Electromagnetic ion cyclotron (waves)
GEO	Geosynchronous orbit
GOES	Geostationary Operational Environmental Satellites
GPS	Global Positioning System
HEPAD	High Energy Proton and Alpha Detector
HOPE	Helium Oxygen Proton Electron sensor
IMF	Interplanetary magnetic field
IRBEM	International Radiation Belt Environment Modelling library
KF	Kalman filter
Kp	Planetary K index
LCDS	Last closed drift shell
LEO	Low-Earth orbit
MAGED	Magnetospheric Electron Detector
MagEIS	Magnetic Electron Ion Spectrometer
MEO	Medium-Earth orbit
MLT	Magnetic local time
PSD	Phase space density
RBSP	Radiation Belt Storm Probes
REPT	Relativistic Electron Proton Telescope
SAA	South Atlantic Anomaly
SI	International System of Units
THEMIS	Time History of Events and Macroscale Interactions during Substorms mission
TS07	Tsyganenko and Sitnov (2007) magnetic field model
ULF	Ultra low frequency (waves)
VERB	Versatile Electron Radiation Belt model
VLF	Very low frequency (waves)

List of Symbols

$\mathbf{A}$	Electromagnetic vector potential
A	Area
$\mathbf{B}$	Magnetic field
B_a	Magnetic field intensity at the top of the atmosphere ($\sim$ 100 km)
B_0	Mean value of the magnetic field on the equator at the Earth's surface
B_{eq}	Magnetic field in the equatorial plane not at the Earth's surface
B_r, B_θ, B_ϕ	Components of geomagnetic field in spherical coordinates
B_m	Magnetic field at the mirror point of a particle
B_w	Wave amplitude
c	Velocity of light in vacuum
D_{ij}	Diffusion coefficients (scattering rates)
D_{pp}	Energy diffusion coefficient
$D_{\alpha_{\text{eq}}\alpha_{\text{eq}}}$	Pitch-angle diffusion coefficient
$D_{\alpha_{\text{eq}}p}, D_{p\alpha_{\text{eq}}}$	Mixed pitch angle-energy diffusion coefficient
$D_{L^*L^*}$	Radial diffusion coefficient
$\mathbf{E}, \mathbf{E}_\perp, \mathbf{E}_\parallel$	Electric field, perpendicular, and parallel components
$\mathbf{E}_{\text{conv}}$	Convection electric field
$\mathbf{E}_{\text{cor}}$	Corrotation electric field
$\mathbb{E}$	Expectation operator
E	Kinetic energy of a particle
E_0	Rest energy of a particle
$\mathbf{F}_R$	Centrifugal force
f	Phase space density, wave linear frequency
f_{ce}	Electron gyrofrequency (in Hz)
$\mathbf{H}$	Observation matrix
H	Horizontal component of the geomagnetic field
$\mathbf{I}$	Identity matrix
I	Second adiabatic invariant
J	Adiabatic invariant
J_1, J_2, J_3	First, second, and third adiabatic invariants
j	Particle flux
$\mathbf{K}$	Kalman gain matrix
K	Combination of the first and second adiabatic invariants
$k, k_\parallel$	Wave vector and its parallel component
L	Magnetic shell parameter, McIlwain L value
L^*	Roederer L value
L_{pp}	Plasmapause location
$\mathbf{M}$	Model matrix
m	Mass of a particle, azimuthal wave number
m_0	Rest mass of a particle
N	Number of particles
n	Harmonic number

n_e	Electron density
$\mathbf{P}$	Canonical momentum of a charged particle
$\mathbf{P}^a$	Analysis error covariance matrix
$\mathbf{P}^f$	Forecast error covariance matrix
P_{dyn}	Solar wind dynamic pressure
$\mathbf{p}, \mathbf{p}_\perp, \mathbf{p}_\parallel$	Particle momentum, perpendicular, and parallel components
$\mathbf{Q}$	Model error covariance matrix
q	Electric charge
q_i	Position coordinate conjugate to momentum coordinate p_i
$\mathbf{R}$	Observational error matrix
$\mathbf{R}_c$	Radius of curvature
$\mathrm{R_E}$	Earth's radius
R_0	Distance from the center of the Earth to the equatorial crossing of a magnetic field line
$\mathbf{r}$	Position vector
r, θ, ϕ	Spherical polar coordinates
r_g	Gyroradius
S	Area
s	Distance measured along a magnetic field line
s_m, s'_m	Mirror point (and its conjugate) location on a magnetic field line
T_e	Electron temperature
$T(\alpha_{\text{eq}})$	Function related to the particle's bounce motion
t	Time
$\mathbf{v}, \mathbf{v}_\perp, \mathbf{v}_\parallel$	Particle velocity, perpendicular, and parallel components
$\mathbf{v}_E$	$\mathbf{E} \times \mathbf{B}$ drift velocity
$\mathbf{v}_R$	Curvature drift velocity
$\mathbf{v}_d$	Velocity of reference frame
$\mathbf{v}_g$	Gyration part of particle velocity
$\mathbf{v}_1$	Small perturbation to particle velocity
$\mathbf{v}_\nabla$	Gradient drift velocity
$\mathbf{x}$	Generalised vector coordinate, state vector
$\mathbf{x}^a$	Assimilated (analysis) state vector
$\mathbf{x}^f$	Forecast state vector
$\mathbf{x}^i, \Delta\mathbf{x}^i$	Innovation vector, difference of innovation vectors
$\mathbf{y}^o$	Observation vector

α	Pitch angle of particle in a magnetic field
α_{eq}	Pitch angle of particle measured at the equatorial plane
α_{LC}	Bounce loss cone pitch angle
β	Velocity of a particle relative to the speed of light
γ	Relativistic factor
$\delta\theta$	Width of wave normal angle
$\delta\omega$	Frequency bandwidth
ϵ^m	Model error
ϵ^o	Observational error
θ_{lc}	Lower cutoff frequency of wave normal angle
θ_m	Wave normal angle where peak of wave power occurs
θ_{uc}	Upper cutoff frequency of wave normal angle
λ	Geomagnetic latitude
μ	Magnetic moment, first adiabatic invariant

τ	Electron lifetime
τ_b	Bounce period of a trapped particle
τ_d	Longitudinal drift period of a trapped particle
τ_g	Gyroperiod of a trapped particle
Φ	Magnetic flux, third adiabatic invariant
$\mathbf{\Omega}_\mathrm{E}$	Angular velocity of Earth's rotation
Ω	Solid angle
Ω_σ	Gyrofrequency of particle σ (in rad/s)
ω	Wave angular frequency
ω_d	Drift frequency of a trapped particle
ω_g	Gyrofrequency of a trapped particle (in rad/s)
ω_{lc}	Lower cutoff frequency of wave
ω_m	Central frequency of wave
ω_{uc}	Upper cutoff frequency of wave

Chapter 1

Introduction

1.1 Motivation

The first scientific measurements of the Space Age were performed more than 50 years ago. Those observations established that the Earth is enshrouded by a population of highly energetic particles (Van Allen et al., 1958; Vernov and Chudakov, 1960). Bearing the name of the scientist credited with their discovery, the Van Allen radiation belts are large-scale regions of geomagnetically trapped particles that pose a significant risk to orbiting spacecraft and humans in space (e.g. Baker et al., 1998; Baker, 2002; Green, Likar, and Shprits, 2017; Baker et al., 2018). With the increasing number of satellites operating in this region, and the hazards that energetic electrons pose to orbital hardware, the formation and dynamics of the radiation belts is currently of paramount importance to the scientific community. This was highlighted by the launch of the Van Allen Probes mission in August 2012, paving the way for a new era in radiation belt research (Mauk et al., 2012; Stratton, Harvey, and Heyler, 2012).

The Earth's outer electron radiation belt is very dynamic in space and time. The flux of electrons in the outer belt can change by many orders of magnitude on timescales ranging from years and months, down to hours and minutes. The variability in the responses of the outer belt to geomagnetic disturbances has been attributed to the complex competing nature of acceleration and loss, which increase and reduce radiation belt populations, respectively (e.g. Friedel, Reeves, and Obara, 2002; Reeves et al., 2003; Millan and Thorne, 2007; Shprits et al., 2008; Millan and Baker, 2012). In order to obtain a global and accurate physical understanding of the dynamics of the outer Van Allen belt, it is necessary to investigate which processes are dominant and under which conditions, how they are coupled, and how their relative contributions superpose to produce the observed response.

Of particular interest are loss mechanisms during radiation belt dropouts, when the electron fluxes drop by several orders of magnitude in just a few hours (e.g. Bortnik et al., 2006; Morley et al., 2010; Turner et al., 2012a; Xiang et al., 2017). Where do electrons go during these events? Which mechanisms contribute to the observed response? How much loss is caused by each physical process? Many open questions still remain on the nature of loss of radiation belt electrons. Up until recently, most of the research aimed towards answering these questions concentrated either on the analysis of data from individual or multiple spacecraft (e.g. Green et al., 2004; Turner et al., 2014b; Boynton, Mourenas, and Balikhin, 2016; Boynton, Mourenas, and Balikhin, 2017; Xiang et al., 2017), or on the utilisation of diffusion models (e.g. Shprits et al., 2006c; Su et al., 2011; Yu, Koller, and Morley, 2013).

Observational analysis of a variety of spacecraft measurements provides a means to understand the mechanisms responsible for the dynamic evolution of the outer

radiation belt. However, such analysis does not allow for inferring the global evolution of the radiation environment, as in-situ satellite observations are often restricted to a limited range of radial distances and energies. Automated analysis of satellite observations is also complicated by the fact that measurements have different instrumental errors. These limitations hinder the calculation of the radial profiles of phase space density, which is essential for investigating the role of various acceleration and loss processes in the evolution of radiation belt electrons.

On the other hand, numerical modelling of the radiation belts has the advantage that by switching on and off the mechanisms of interest, their relative contribution to the dynamics of radiation belt electrons can be revealed. Nevertheless, several important approximations (e.g. composition of the magnetospheric plasma, location of magnetopause boundary), and errors in model parameters (e.g. diffusion rates derived from statistical models of waves) and in the initial and boundary conditions, may lead to significant uncertainties in the estimation of the actual effect of a specific mechanism.

It is evident from the above description that, in order to globally study the outer electron radiation belt at all spatial locations, energies, and pitch angles, it is imperative to utilise an approach that combines satellite observations from various orbits and physics-based models. Data assimilation provides such tools which allow us to correct inaccurate measurements, fill in the gaps left by sparse in-situ measurements, and bring the model predictions closer to reality.

The potential of data assimilation to significantly improve the capabilities of radiation belt models has been shown by a number of studies (e.g. Naehr and Toffoletto, 2005; Shprits et al., 2007; Koller et al., 2007; Bourdarie and Maget, 2012; Kellerman et al., 2014). These previous works have demonstrated how data assimilation can be used to reconstruct the dynamic evolution of the Van Allen belts and to identify and adjust for missing processes in physics-based models. Other studies have focused on the sensitivity of data assimilation, for instance, to the initial condition and the location of the outer boundary (Daae et al., 2011), and to empirical external magnetic field models (Ni et al., 2009). However, systematic investigations of the role of acceleration and loss on the variability of radiation belt electrons, by relying on the assimilation of multiple spacecraft data in a diffusion model, have not been carried out until this dissertation.

1.2 Objectives and Scientific Contribution

The research presented in this thesis addresses the complex physics of the dynamics of the Van Allen belts. The main goal is to contribute to the understanding of loss of trapped electrons from the outer radiation belt by focusing on two distinct processes: scattering by electromagnetic ion cyclotron waves and magnetopause shadowing. In order to reveal the nature of each mechanism, the temporal evolution of the outer belt is reconstructed by assimilating multiple spacecraft data into a diffusion model via a split-operator Kalman filter (Shprits et al., 2013a). Satellite measurements are obtained from the twin Van Allen Probes and from the Geostationary Operational Environmental Satellites fleet. The model employed in this work is the three-dimensional Versatile Electron Radiation Belt (VERB-3D) code (Shprits et al., 2008; Subbotin and Shprits, 2009).

This study is guided by the following science questions:

1. How can sparse in-situ measurements be blended with a physics-based model in order to reconstruct the long-term evolution of the Van Allen belts? (Chapters 7 and 8)
2. How can the difference between observations and predictions help towards identifying missing processes in a model? (Chapter 7)
3. Which physical loss mechanisms control the dynamic evolution of radiation belt electrons? (Chapter 8)

The specific objectives of this thesis are to:

1. Implement the following physical processes absent in previous data assimilation schemes: (1) mixed pitch angle-energy diffusion by hiss and chorus waves, (2) pitch-angle scattering by electromagnetic ion cyclotron waves, and (3) magnetopause shadowing (Chapter 7).
2. Assimilate multi-satellite data into the VERB-3D model by means of a Kalman filter, and reconstruct the evolution of the Van Allen belt electrons from 01 October 2012 to 01 October 2016 (Chapters 7 and 8).
3. Employ the innovation vector, a measure on how observations and model predictions differ, as a means to quantify the loss effect of pitch-angle diffusion driven by electromagnetic ion cyclotron waves and magnetopause shadowing (Chapters 7 and 8).
4. Compare the contribution of the two above-mentioned loss mechanisms for different levels of geomagnetic activity and for electron energies ranging from relativistic ($\sim$ 800 keV) to ultrarelativistic ($\sim$ 3.6 MeV) (Chapter 8).

The primary contributions of this research can be summarised as follows:

1. Performed a long-term reconstruction of the Van Allen belts spanning various levels of geomagnetic activity over four years, resulting in a product available to the broader scientific community (Cervantes et al., 2020a; Cervantes et al., 2020b).
2. Carried out the first assimilation of the state-of-the-art Van Allen Probes data into a three-dimensional diffusion model, reconstructing the global dynamic evolution of radiation belt electrons for the above-mentioned period (Cervantes et al., 2020a; Cervantes et al., 2020b).
3. Derived a new metric based on the Kalman filter and the innovation vector to quantify the effect of two distinct loss processes: scattering by electromagnetic ion cyclotron waves and magnetopause shadowing (Cervantes et al., 2020b).

1.3 Outline

This thesis is divided into three main parts, with Chapters 2 and 3 describing background information, Chapters 4 to 6 presenting the methodology and databases, and Chapters 7 to 9 summarising the key findings of this work. Chapter 2 gives a short introduction to basic space plasma physics, adiabatic theory, and the solar-terrestrial

environment; and Chapter 3 focuses on the dynamics of the electrons populating the outer radiation belt. Chapter 4 describes how the temporal evolution of electrons in the radiation belts is modelled, and it presents the numerical model employed in this study. Chapter 5 presents the instrumentation and satellite missions which provided data for this thesis; and Chapter 6 defines the concept of data assimilation, as the overarching algorithm blending model predictions and data, by means of a split-operator Kalman filter. Chapter 7 discusses how the innovation, a measure calculated by the Kalman filter, adds a source and loss term to the diffusion model; and Chapter 8 employs the innovation to estimate the effect of the two above-mentioned loss mechanisms during radiation belt dropouts. Finally, Chapter 9 provides a summary of this work and makes recommendations for future studies.

Chapter 2

The Sun-Earth System

More than 50 years ago, at the dawn of the Space Age, a population of high-energy particles enshrouding the Earth was unexpectedly discovered by the flight of the Explorer 1, Sputnik 3, and Explorer 3 spacecraft. This was an astounding surprise and represented the founding of what is now called magnetospheric physics. Over the following decades, several missions have expanded and evolved our knowledge of the particles and waves that define the near-Earth space environment.

The first section of this chapter introduces the motion of charged particles inside magnetic and electric fields, and describes how these particles become trapped in the geomagnetic field. Then, several plasma populations which exist in the Earth's magnetosphere, either of terrestrial or solar origin, are presented. Finally, the last section discusses major disturbances of the terrestrial magnetosphere that arise from the complex interplay between the Sun and the geomagnetic field.

2.1 Single Charged Particle Motion

The fundamental equation describing the motion of a test charged particle in a magnetic field $\mathbf{B}$ and an electric field $\mathbf{E}$ is the Lorentz equation, given in SI units as:

$$m\frac{\mathrm{d}\mathbf{v}}{\mathrm{d}t} = q(\mathbf{E} + \mathbf{v} \times \mathbf{B}), \tag{2.1}$$

where q denotes the particle charge and $\mathbf{v}$ its velocity. If purely an electric field is considered ($\mathbf{B} = 0$), any acceleration experienced by the particle will be in the direction parallel to the field. Considering purely a magnetic field ($\mathbf{E} = 0$), any acceleration will occur perpendicular to both the magnetic field direction and the velocity of the particle.

2.1.1 Gyration

Under the absence of an electric field ($\mathbf{E} = 0$), and assuming a uniform and constant magnetic field, equation 2.1 reduces to:

$$m\frac{\mathrm{d}\mathbf{v}}{\mathrm{d}t} = q(\mathbf{v} \times \mathbf{B}). \tag{2.2}$$

Splitting this into velocity components parallel and perpendicular to $\mathbf{B}$ yields:

$$\left(m\frac{\mathrm{d}\mathbf{v}}{\mathrm{d}t}\right)_{\parallel} = q(\mathbf{v}_{\parallel} \times \mathbf{B}) = 0, \tag{2.3}$$

and:

$$\left(m\frac{\mathrm{d}\mathbf{v}}{\mathrm{d}t}\right)_{\perp} = q(\mathbf{v}_{\perp} \times \mathbf{B}). \tag{2.4}$$

Integrating equation 2.3 gives:

$$m\mathbf{v}_{\parallel} = \text{constant}. \tag{2.5}$$

This indicates that the particle moves parallel to **B** with a constant speed. Equation 2.4 shows that the velocity change resulting from the Lorentz force is perpendicular to both the uniform field **B** and $\mathbf{v}_{\perp}$. Therefore $\mathbf{v}_{\perp}$ remains constant in magnitude and the particle follows a circular trajectory with radius r_g, when projected on to a plane perpendicular to the magnetic field (Walt, 1994).

The Lorentz force must balance the centrifugal force giving:

$$qv_{\perp}B = \frac{mv_{\perp}^2}{r_g}. \tag{2.6}$$

The radius of this circular motion around the magnetic field (gyromotion) is known as gyroradius r_g, and is defined as:

$$r_g = \frac{mv_{\perp}}{qB}. \tag{2.7}$$

The gyroperiod τ_g is the time a particle takes to complete one rotation:

$$\tau_g = 2\pi\frac{m}{qB}, \tag{2.8}$$

and the angular frequency of the gyration, the gyrofrequency, is given by:

$$\omega_g = \frac{2\pi}{\tau_g} = \frac{qB}{m}. \tag{2.9}$$

The direction of acceleration of a particle depends on the charge of the particle. Electrons gyrate anticlockwise and ions clockwise around the magnetic field. The centre of this orbit is called the guiding centre.

In addition to the circular motion around the magnetic field, a particle may also have a constant velocity parallel to the field, $v_{\parallel}$. The sum of these velocity vectors causes the particle to travel with a helical trajectory, an example of which is shown in Figure 2.1. The pitch angle α of the helix is the angle between the particle velocity and the magnetic field, and is given by:

$$\alpha = \tan^{-1}\left(\frac{v_{\perp}}{v_{\parallel}}\right). \tag{2.10}$$

Particles with pitch angles near 0° move predominantly parallel to **B**, whereas particles with large pitch angles near 90° move essentially in circles (Walt, 1994).

2.1.2 Bounce Motion

In a converging magnetic field charged particles display a motion known as magnetic mirroring. As the particles spiral along the field, they experience an increased field strength. Provided that the change of the field is small over one gyroradius in one gyroperiod, then the field can be approximated as being static, doing no work on the particle (Baumjohann and Treumann, 2012). Therefore, by Faraday's law, the

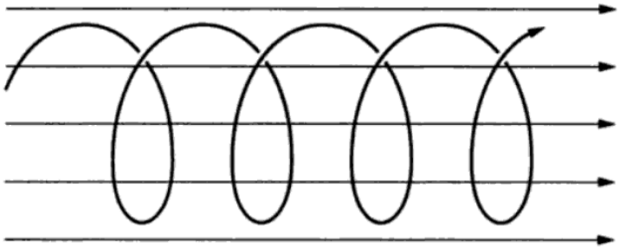

FIGURE 2.1: Helical motion of an ion in a uniform magnetic field (Baumjohann and Treumann, 2012).

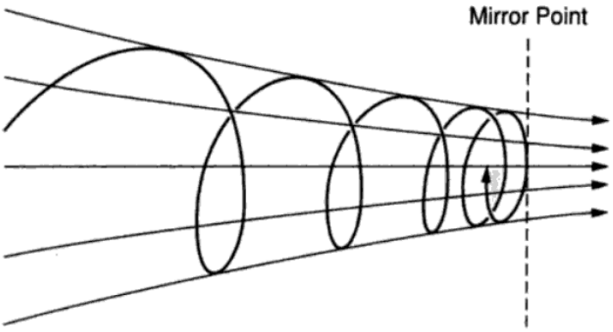

FIGURE 2.2: Orbit of an ion along a converging magnetic field geometry reflected at its mirror point (Baumjohann and Treumann, 2012).

magnetic flux Φ enclosed by a circle with radius equal to the particle's gyroradius is constant and is given by:

$$\Phi = B\pi r_g^2 = \frac{\pi m^2 v_\perp^2}{q^2 B} = \text{constant.} \tag{2.11}$$

As π, q, and m are constants for a single particle, and expressing equation 2.11 in terms of the particle's pitch angle α, it follows that:

$$\frac{v^2 \sin^2\alpha}{B} = \text{constant.} \tag{2.12}$$

For a particle moving from a region with lower magnetic field strength B_1, to a region with higher field strength B_2, it can be stated that:

$$\frac{\sin^2\alpha_1}{B_1} = \frac{\sin^2\alpha_2}{B_2}. \tag{2.13}$$

As the magnetic field B experienced by the particle increases (as it moves into a converging field), α increases accordingly, up to 90°. At this point the magnetic field strength is such that the particle's velocity is completely in the plane perpendicular to the magnetic field (i.e. $v = v_\perp$), and all motion parallel to the magnetic field ceases. This location is called the mirror point, and the particle cannot penetrate any further, as visualised in Figure 2.2. After reaching this point the particle reverses its motion parallel to the magnetic field and spirals back in the direction it came, towards a weaker magnetic field. As a result, the particle is reflected and it bounces back due to the force exerted by the field gradient. This process is called magnetic mirroring.

In the geomagnetic field (see Section 2.3.2), with a minimum intensity in the magnetic equatorial plane and converging field lines on both hemispheres, a particle may bounce back and forth between its mirror points and become trapped. It is this mirror effect which causes the radiation belt and ring current particles in the Earth's magnetosphere to become trapped (Section 2.3.3). This back and forth motion between conjugate mirror points in the northern and southern hemispheres is called the particle's bounce motion. The bounce period is the time it takes a particle to move from the equatorial plane to one mirror point, then to the other in the opposite hemisphere, and finally back to the equatorial plane.

The equatorial pitch angle α_{eq} is the pitch angle of the particle at the geomagnetic equator, where the field strength B_{eq} along the field line is minimum. The pitch angle at any point along a field line can be given in terms of the equatorial values B_{eq} and α_{eq} (Walt, 1994):

$$\sin \alpha(B) = \sqrt{\frac{B}{B_{\text{eq}}}} \sin\alpha_{\text{eq}}, \tag{2.14}$$

or in terms of the values at the mirror point B_m as follows:

$$\sin \alpha(B) = \sqrt{\frac{B}{B_m}}. \tag{2.15}$$

2.1.3 Drift Motion

A geomagnetically trapped particle gyrates around magnetic field lines, bounces from one hemisphere to the other, and drifts longitudinally around the Earth. The latter arises from large scale magnetospheric electric fields and inhomogeneities in the geomagnetic field.

2.1.3.1 $\mathbf{E} \times \mathbf{B}$ Drift

The presence of an external electrostatic field modifies the motion of a particle gyrating around the uniform magnetic field. An electrostatic field $\mathbf{E}_{\parallel}$ parallel to the magnetic field accelerates particles along a field line. Ions are accelerated in the direction of $\mathbf{E}_{\parallel}$ and electrons in the opposite direction. This charge displacement produces an additional electrostatic field which cancels out the original parallel electric field. Therefore, most parallel electric fields cannot be sustained. Such parallel electric fields are rarely found in the trapping region of the magnetosphere. However, they are important in accelerating particles in the aurora (Walt, 1994).

Moderate electrostatic fields perpendicular to a uniform $\mathbf{B}$ result in a drift perpendicular to both $\mathbf{B}$ and $\mathbf{E}_{\perp}$. This effect can be understood by using a reference system moving at velocity $\mathbf{v}_d$ perpendicular to $\mathbf{B}$. The electric field in the moving system is:

$$\mathbf{E}' = \mathbf{E} + \mathbf{v}_d \times \mathbf{B}. \tag{2.16}$$

In order to eliminate the electric field in the moving frame $\mathbf{E}'$, $\mathbf{v}_d$ is chosen such that $\mathbf{E}' = 0$. The vector product between $\mathbf{B}$ and equation 2.16 gives:

$$\mathbf{B} \times \mathbf{E}' = \mathbf{B} \times (\mathbf{E} + \mathbf{v}_d \times \mathbf{B}). \tag{2.17}$$

Setting $\mathbf{E}' = 0$ and using the vector triple product yields:

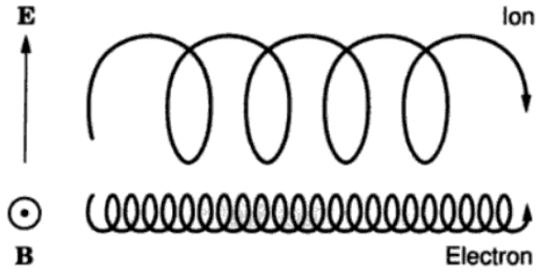

FIGURE 2.3: Particle drifts in uniform **E** and **B** fields (Baumjohann and Treumann, 2012).

$$0 = \mathbf{B} \times \mathbf{E} + \mathbf{B} \times (\mathbf{v}_d \times \mathbf{B}) = \mathbf{B} \times \mathbf{E} + (\mathbf{B} \cdot \mathbf{B})\mathbf{v}_d - (\mathbf{B} \cdot \mathbf{v}_d)\mathbf{B}, \tag{2.18}$$

where $\mathbf{B} \cdot \mathbf{B} = B^2$ and, because $\mathbf{B} \cdot \mathbf{v}_d = 0$:

$$0 = \mathbf{B} \times \mathbf{E} + B^2 \mathbf{v}_d. \tag{2.19}$$

The required frame velocity is:

$$\mathbf{v}_d = \frac{\mathbf{E} \times \mathbf{B}}{B^2} \equiv \mathbf{v}_E. \tag{2.20}$$

In a frame moving with velocity $\mathbf{v}_E$, the electric field vanishes and the particle moves helically as described in Section 2.1.1. In a stationary frame the motion is a deformed gyromotion drifting at velocity $\mathbf{v}_E$.

Figure 2.3 shows the acceleration and deceleration effects of a perpendicular electric field. An ion has greatest energy and largest gyroradius when it is accelerated in the direction of the electric field. In the second half of its orbit it is decelerated, and its gyroradius decreases. An electron circles in the opposite sense and has its largest gyroradius when moving antiparallel to the electric field, and is decelerated when moving parallel. Over several gyrations the different gyroradii shift the position of the guiding centre in a direction perpendicular to both $\mathrm{E}_\perp$ and **B**, causing a net displacement, or drift. This drift of the guiding centre is called the $\mathbf{E} \times \mathbf{B}$ drift and has the form in equation 2.20. The $\mathbf{E} \times \mathbf{B}$ drift is independent of the sign of the charge, and therefore electrons and ions move in the same direction.

2.1.3.2 Gradient Drift

The motion of a charged particle can be further modified if the magnetic field in which it travels is weakly inhomogeneous. In the case of the Earth, the geomagnetic field strength decreases with increasing radial distance. Such a gradient in the field in the direction perpendicular to **B** causes the magnetic field strength experienced by the gyrating particle to change in magnitude throughout its gyromotion. According to equation 2.7, the gyroradius of the particle changes as it moves from a region of stronger magnetic field to a weaker field region. Over several gyroperiods, this varying radius results in the particle drifting perpendicular to both **B** and $\nabla\mathbf{B}$ (Baumjohann and Treumann, 2012).

Assuming that the magnetic field gradient is such that the magnitude of **B** does not change appreciably on the scale of the particle gyroradius, then the particle velocity can be split into a gyration part $\mathbf{v}_g$, and a small perturbation $\mathbf{v}_1$:

$$\mathbf{v} = \mathbf{v}_g + \mathbf{v}_1. \tag{2.21}$$

The magnetic field vector can be Taylor-expanded around $\mathbf{x} = 0$ as follows:

$$\mathbf{B} = \mathbf{B}_0 + \mathbf{x} \cdot \nabla \mathbf{B}, \tag{2.22}$$

where $\mathbf{x}$ is the position vector. Assuming that $\mathbf{E} = 0$ and inserting equations 2.21 and 2.22 in equation 2.1 we obtain:

$$\frac{\mathrm{d}(\mathbf{v}_g + \mathbf{v}_1)}{\mathrm{d}t} = \frac{q}{m}[(\mathbf{v}_g \times \mathbf{B}_0) + (\mathbf{v}_1 \times \mathbf{B}_0) + (\mathbf{v}_g \times (\mathbf{x} \cdot \nabla \mathbf{B})) + (\mathbf{v}_1 \times (\mathbf{x} \cdot \nabla \mathbf{B}))]. \tag{2.23}$$

In a uniform magnetic field, equation 2.23 becomes:

$$\frac{\mathrm{d}\mathbf{v}_g}{\mathrm{d}t} = \left(\frac{q}{m}\mathbf{v}_g \times \mathbf{B}_0\right). \tag{2.24}$$

In order to isolate the perturbation velocity we subtract equation 2.24 from equation 2.23. Furthermore, using $(\mathbf{v}_1 \times (\mathbf{x} \cdot \nabla \mathbf{B})) \sim 0$ as perturbations are small, yields:

$$\frac{\mathrm{d}\mathbf{v}_1}{\mathrm{d}t} = \frac{q}{m}[(\mathbf{v}_1 \times \mathbf{B}_0) + (\mathbf{v}_g \times (\mathbf{x} \cdot \nabla \mathbf{B}))]. \tag{2.25}$$

The time average of $\mathbf{v}_1$ over one gyroperiod τ_g is the drift velocity $\mathbf{v}_\nabla$:

$$\mathbf{v}_\nabla = \langle \mathbf{v}_1 \rangle = \frac{1}{\tau_g} \int_0^T \mathbf{v}_1 \, \mathrm{d}t. \tag{2.26}$$

Taking the time average of equation 2.25 results in:

$$\mathbf{v}_\nabla \times \mathbf{B}_0 + \langle \mathbf{v}_g \times (\mathbf{x} \cdot \nabla \mathbf{B}) \rangle = 0, \tag{2.27}$$

assuming a constant drift velocity. Since the average is performed over a gyroperiod, the gyromotion trajectory is described by $\mathbf{x}$. If $\mathbf{B} = B(x, y)\hat{\mathbf{z}}$, we can express the gyromotion as:

$$\mathbf{v}_\nabla = v_g(\cos(\omega_g t + \phi)\hat{\mathbf{x}} - \sin(\omega_g t + \phi)\hat{\mathbf{y}}), \tag{2.28}$$

and the position vector for the gyromotion trajectory as:

$$\mathbf{x} = \frac{v_g}{\omega_g}(\sin(\omega_g t + \phi)\hat{\mathbf{x}} - \cos(\omega_g t + \phi)\hat{\mathbf{y}}). \tag{2.29}$$

Substituting equations 2.28 and 2.29 in the second term of equation 2.27 and taking into account that $\langle \sin^2(\omega_g t + \phi) \rangle = \langle \cos^2(\omega_g t + \phi) \rangle = 1/2$ and $\langle \sin(\omega_g t + \phi)\cos(\omega_g t + \phi) \rangle = 0$ yields:

$$\mathbf{v}_\nabla \times \mathbf{B}_0 = \frac{v_g^2}{2\omega_g}\frac{\partial B}{\partial x}\hat{\mathbf{x}} + \frac{v_g^2}{2\omega_g}\frac{\partial B}{\partial y}\hat{\mathbf{y}}, \tag{2.30}$$

and using equation 2.9:

$$\mathbf{v}_\nabla \times \mathbf{B}_0 = \frac{m v_g^2}{2qB}\left(\frac{\partial B}{\partial x}\hat{\mathbf{x}} + \frac{\partial B}{\partial y}\hat{\mathbf{y}}\right), \tag{2.31}$$

which can be rewritten as:

$$\mathbf{v}_\nabla \times \mathbf{B}_0 = \frac{m v_g^2}{2qB}\nabla \mathbf{B}. \tag{2.32}$$

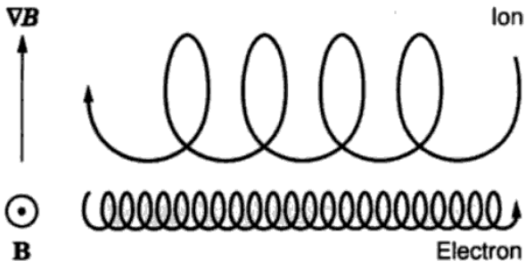

FIGURE 2.4: Particle drifts in uniform **E** and **B** fields (Baumjohann and Treumann, 2012).

Taking the cross product of $\mathbf{B}_0$ and equation 2.32 and using the triple vector product rule give:

$$\mathbf{v}_\nabla B^2 - \mathbf{B}_0(\mathbf{B}\cdot\mathbf{v}_\nabla) = \frac{mv_g^2}{2qB}\mathbf{B}\times\nabla\mathbf{B}. \tag{2.33}$$

Since the drift velocity is perpendicular to the field direction $\mathbf{B}\cdot\mathbf{v}_\nabla = 0$, equation 2.33 can be rewritten as:

$$\mathbf{v}_\nabla = \frac{mv_g^2}{2qB^3}\mathbf{B}\times\nabla\mathbf{B}. \tag{2.34}$$

If $\mathbf{v}_\nabla << \mathbf{v}_g$, then the component of the particle velocity perpendicular to the magnetic field $v_\perp$, is approximately equal to the gyrovelocity, resulting in the following relation for the gradient drift:

$$\mathbf{v}_\nabla = \frac{mv_\perp^2}{2qB^3}\mathbf{B}\times\nabla\mathbf{B}. \tag{2.35}$$

The gradient drift is charge-dependent and therefore, as visualised in Figure 2.4, electrons and ions drift in opposite directions.

2.1.3.3 Curvature Drift

The drift due to a magnetic field gradient is just one component of the drift motion to occur in an inhomogeneous magnetic field. If the field lines are curved or bent, as is the case of the geomagnetic field, a curvature drift appears. Due to its parallel velocity $v_\parallel$, a charged particle will experience a centrifugal force:

$$\mathbf{F}_R = mv_\parallel^2\frac{\mathbf{R}_c}{R_c^2}, \tag{2.36}$$

where $\mathbf{R}_c$ is the local radius of curvature of the magnetic field line. This force is equivalent to an electric field with magnitude $\mathbf{E}_c = mv_\parallel^2\mathbf{R}_c/qR_c^2$. Substituting this electric field in equation 2.20 yields the curvature drift:

$$\mathbf{v}_R = \frac{mv_\parallel^2}{q}\frac{\mathbf{R}_c\times\mathbf{B}}{R_c^2B^2}. \tag{2.37}$$

The curvature drift is proportional to the parallel energy of the particle, and is perpendicular to both the magnetic field and its curvature radius. The particle charge dictates the direction of $\mathbf{v}_R$, and hence electrons and ions drift in opposite directions. In the case of the Earth, the gradient and curvature drift are eastward for electrons

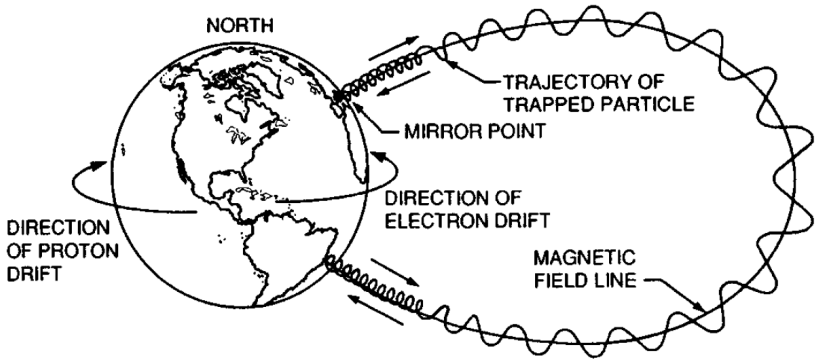

FIGURE 2.5: Trajectories of particles trapped on closed field lines experiencing magnetic mirroring and gradient-curvature drift in the geomagnetic field (Walt, 1994).

and westward for ions, as sketched in Figure 2.5. The drift equations derived in this section are the fundamental elements that lead to particle trapping in the geomagnetic field (Walt, 1994).

2.2 Adiabatic Invariants

The previous section introduced the three types of periodic motion charged particles in the geomagnetic field undergo: rapid gyration around the field lines, north-south oscillation between mirror points, and slow longitudinal drift around the Earth. Each type of periodic motion is associated with an adiabatic invariant, which stays approximately constant under slow variations of parameters of the system, compared to the period of the corresponding motion. A general expression of the adiabatic invariant J_i is given by the following integral (Landau and Lifshits, 1973):

$$J_i = \oint_i p_i \, \mathrm{d}q_i, \tag{2.38}$$

where the integral is taken over the periodic motion, and p_i and q_i are conjugate momentum and position coordinates, which are canonical coordinates in a Hamiltonian system.

For a charged particle in a magnetic field, the canonical momentum $\mathbf{P}$ is:

$$\mathbf{P} = m\mathbf{v} + q\mathbf{A} = \mathbf{p} + q\mathbf{A}, \tag{2.39}$$

where $\mathbf{A}$ is the electromagnetic vector potential. The three adiabatic invariants of the particle motion are then given by integrating $\mathbf{P}$ over the appropriate periodic orbits.

2.2.1 First Adiabatic Invariant

The first adiabatic invariant is related to the gyromotion of a charged particle around a magnetic field line as described in Section 2.1.1. Integrating equation 2.39 around the gyration orbit, where $\mathrm{d}\mathbf{l}$ is an element of the particle path around the orbit yields:

$$J_1 = \oint [\mathbf{p} + q\mathbf{A}] \cdot \mathrm{d}\mathbf{l} = 2\pi r_g p_\perp + q \oint \mathbf{A} \cdot \mathrm{d}\mathbf{l}, \tag{2.40}$$

where $p_\perp$ is the particle momentum perpendicular to the magnetic field. Using equation 2.7 for r_g and invoking Stoke's theorem gives:

$$J_1 = \frac{2\pi p_\perp^2}{qB} + q \oint \nabla \times \mathbf{A} \cdot \mathrm{d}\mathbf{S}, \tag{2.41}$$

where $d\mathbf{S}$ is an element of the area enclosed by the gyromotion. The curl of the vector potential is equal to the magnetic field ($\nabla \times \mathbf{A} = \mathbf{B}$) and, as the unit vector $d\mathbf{S}$ points in the opposite direction to $\mathbf{B}$, equation 2.41 yields:

$$J_1 = q \oint \mathbf{B} \cdot \mathrm{d}\mathbf{S} = -qB\pi r_g^2 = \frac{-\pi p_\perp^2}{qB}. \tag{2.42}$$

Therefore J_1 becomes:

$$J_1 = \frac{2\pi p_\perp^2}{qB} - \frac{\pi p_\perp^2}{qB} = \frac{\pi p_\perp^2}{qB}. \tag{2.43}$$

Rather than using the above expression for J_1, the first invariant is often taken to be:

$$\mu = \frac{p_\perp^2}{2m_0 B}, \tag{2.44}$$

where m_0 is the particle rest mass. Equation 2.44 is equal to J_1 except for constant factors and is called the magnetic moment, since in the non-relativistic case, it is equal to the current around the particle orbit times the area of the loop. For a particle of kinetic energy E, the relativistic momentum p, is defined as:

$$p^2 = \frac{E^2 + 2m_0 c^2 E}{c^2}, \tag{2.45}$$

where c is the speed of light. In a slowly varying magnetic field (i.e. if changes to the field occur on a time frame much longer than the period of gyration τ_g), the first adiabatic invariant μ, is conserved.

The kinetic energy of a particle can be related to the first adiabatic invariant as:

$$E = E_0 \left\{ \sqrt{\left(\frac{2B\mu}{E_0 \sin^2(\alpha)} + 1 \right)} - 1 \right\}, \tag{2.46}$$

where E_0 is the particle rest energy.

2.2.2 Second Adiabatic Invariant

The second adiabatic invariant is associated with the bounce motion of a particle along a magnetic field line between its mirror points and is defined as:

$$J_2 = \oint [\mathbf{p} + q\mathbf{A}] \cdot \mathrm{d}\mathbf{s}, \tag{2.47}$$

where $d\mathbf{s}$ is an element of length along a field line. Considering the second term and again using Stoke's theorem yields:

$$\oint q\mathbf{A} \cdot \mathrm{d}\mathbf{s} = q \int \nabla \times \mathbf{A} \cdot \mathrm{d}\mathbf{S} = q \int \mathbf{B} \cdot \mathrm{d}\mathbf{S}, \tag{2.48}$$

where $\mathbf{S}$ is the surface enclosed by the bounce motion along a magnetic field line. As the integration path encloses a negligible area and no magnetic flux, then $q \int \mathbf{B} \cdot d\mathbf{S} = 0$. Therefore the second adiabatic invariant is:

$$J_2 = \oint \mathbf{p} \cdot \mathrm{d}\mathbf{s} = \oint p_{\parallel} \cdot \mathrm{d}s = \oint p\cos\alpha \cdot \mathrm{d}s, \tag{2.49}$$

where $p_{\parallel}$ denotes the relativistic momentum parallel to the magnetic field.

The second invariant is called the integral invariant, and is normally designated by J rather than J_2. In order to remove the particle momentum from the definition in equation 2.49 and to express the invariant solely in terms of the magnetic field geometry, a related quantity I, is often used as the integral invariant coordinate. Using equation 2.13 and setting B_2 to be the field strength at the particle mirror point B_m, and thus $\sin^2\alpha_2 = 1$, yields:

$$\cos\alpha = \sqrt{1 - \frac{B(s)}{B_m}}. \tag{2.50}$$

The related quantity I is defined as:

$$I = \frac{J}{2p} = \frac{1}{2}\oint \sqrt{1 - \frac{B(s)}{B_m}}\,\mathrm{d}s = \int_{s_m}^{s'_m} \sqrt{1 - \frac{B(s)}{B_m}}\,\mathrm{d}s, \tag{2.51}$$

where s_m and s'_m are the locations of the mirror points in each hemisphere along a field line. Furthermore, a combination of the first two invariants, known as the K invariant, is usually employed:

$$K = \frac{J}{2\sqrt{2m_0\mu}} = \int_{s_m}^{s'_m} \sqrt{B_m - B(s)}\,\mathrm{d}s. \tag{2.52}$$

The advantage of the K invariant is that it does not depend on the charge or the mass of the particle and is purely a geometric factor.

In a dipole magnetic field, the equatorial pitch angle of electrons can be related to the invariant K as (Schulz and Lanzerotti, 1974):

$$y\sqrt{\frac{L}{0.31}}K - 2.7604(1-y) - 0.6396(y\ln y + 2y - 2\sqrt{y}) = 0, \tag{2.53}$$

where $y = \sin(\alpha_{\mathrm{eq}})$.

The magnetic field strength B at any point in space of an idealised dipole is:

$$B = \sqrt{B_r^2 + B_\theta^2} = B_0\left(\frac{\mathrm{R_E}}{r}\right)^3 \sqrt{1 + 3\cos^2\theta}, \tag{2.54}$$

where B_r and B_θ are the spherical polar coordinates of $\mathbf{B}$, r is the radial distance from the center of the dipole, θ is the polar angle or colatitude, B_0 is the mean value of the field on the equator at the Earth's surface ($r = 1$), and $\mathrm{R_E}$ is the mean radius of the Earth. The equation for a geomagnetic field line in spherical coordinates is given by:

$$r = R_0\sin^2\theta, \tag{2.55}$$

where R_0 is the distance from the center of the Earth to the equatorial crossing point of a magnetic field line. The intensity of the field strength in a dipole along a field line is obtained by substituting equation 2.55 into 2.54, giving:

$$B = B_0\left(\frac{\mathrm{R_E}}{R_0}\right)^3 \frac{\sqrt{1 + 3\cos^2\theta}}{\sin^6\theta}. \tag{2.56}$$

The bounce period of a particle τ_b, introduced in Section 2.1.2, is given by:

$$\tau_b = 2\int_{s_m}^{s'_m} \frac{\mathrm{d}s}{v_{\parallel}(s)} = \frac{2}{v}\int_{s_m}^{s'_m} \frac{\mathrm{d}s}{\sqrt{1-\frac{B(s)}{B_m}}} = \frac{2}{v}\int_{s_m}^{s'_m} \frac{\mathrm{d}s}{\sqrt{1-\frac{B(s)}{B_{\mathrm{eq}}}\sin^2\alpha_{\mathrm{eq}}}}. \tag{2.57}$$

A distance element ds of a field line for a dipole is:

$$\mathrm{d}s = \sqrt{(\mathrm{d}r)^2 + (r\mathrm{d}\theta)^2}. \tag{2.58}$$

By differentiating equation 2.55, dr can be expressed in terms of dθ. Inserting equation 2.56 into 2.57 and changing the variable of integration from s to θ yields:

$$\tau_b = \frac{4R_0}{v}\int_{\theta_m}^{\pi/2} \frac{\sin\theta\sqrt{(1+3\cos^2\theta)}}{\sqrt{1-\sin^2\alpha_{\mathrm{eq}}\csc^6\theta(1+3\cos^2\theta)^{0.5}}}\mathrm{d}\theta. \tag{2.59}$$

In a dipole field, equation 2.59 cannot be evaluated exactly. An approximate formula good to about 0.5% is (Walt, 1994) :

$$\tau_b = 0.117\left(\frac{R_0}{\mathrm{R_E}}\right)\frac{1}{\beta}[1-0.4635\sin^{0.75}\alpha_{\mathrm{eq}}], \tag{2.60}$$

where $\beta = v/c$. If large scale changes in the magnetic field occur on time frames longer than the bounce period τ_b, J (and hence I) is conserved and can be treated as an invariant. This implies that a charged particle will move in such a way that the total length of the particle bounce path will be conserved.

The main use of the second invariant is to trace drift paths and surfaces mapped by the bounce and drift motion of a particle, known as drift shells. In an axisymmetric magnetic field and in the absence of electric fields, this surface will be axisymmetric too, as the gradient and curvature drifts are perpendicular to **B** and ∇B. If the Earth possessed this idealised undistorted dipole magnetic field, the drift path of a particle would circle the Earth and return to its initial field line.

However, the geometry of the distorted asymmetric geomagnetic field varies in such a way that the drift orbit of a particle is not circular when mapped to the equatorial plane. Figure 2.6 illustrates a drift path in an asymmetric field. Consider a particle initially on curve 1 on the right-hand side bouncing and mirroring at B_m in both northern and southern hemispheres. As the particle azimuthally orbits around the Earth, it will encounter field lines of varying geometry, due to the distortion of the geomagnetic field. In addition, at each longitude there exists only one curve between mirror values of B_m having the required J value. For J to be conserved in a distorted magnetic field, a particle initially on magnetic field line 1 will drift to line 2 on the left-hand side, and then return to its initial position on line 1 once it has completed a full drift orbit around the magnetic axis.

Particles initially on the same field line but having different pitch angles (and therefore different K values) will trace out different shells before returning to the initial line after a complete drift orbit. This effect is called drift shell splitting and becomes significant for field lines extending more than $\sim 4\ \mathrm{R_E}$ from the Earth (Walt, 1994).

2.2.3 Third Adiabatic Invariant

The third adiabatic invariant is related to the longitudinal drift of a geomagnetically trapped particle around the Earth. Integrating equation 2.39 over the periodic drift

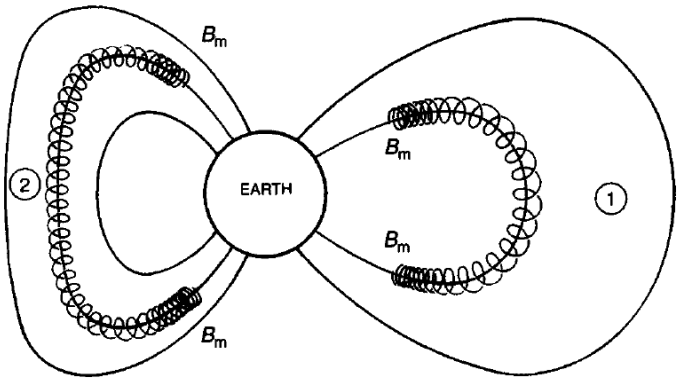

FIGURE 2.6: Schematic representation of a particle mirroring and drifting in the distorted geomagnetic field. If the field is static or changes slowly in comparison to the characteristic timescales of each type of periodic motion, the particle will reflect at fixed B_m, and as it drifts, it will bounce along the field line on which its motion between mirror points conserves the second adiabatic invariant (Walt, 1994).

motion yields the third adiabatic invariant:

$$J_3 = \oint [\mathbf{p} + q\mathbf{A}] \cdot \mathrm{d}\mathbf{l}, \tag{2.61}$$

where d$\mathbf{l}$ is the increment of the longitudinal drift path. The first term of equation 2.61 is usually neglected as the drift velocity of a particle is generally orders of magnitude less than the total particle velocity, and thus the average momentum $\mathbf{p}$ in the direction of d$\mathbf{l}$ is negligible (i.e. $\oint \mathbf{p} \cdot \mathrm{d}\mathbf{l} = 0$). Again, by employing Stoke's theorem:

$$J_3 = q \oint \nabla \times \mathbf{A} \cdot \mathrm{d}\mathbf{S}, \tag{2.62}$$

where d$\mathbf{S}$ is an element of the surface enclosed by the equatorial drift path. Since $\nabla \times \mathbf{A} = \mathbf{B}$, the third invariant can be defined as:

$$J_3 = q \oint \mathbf{B} \cdot \mathrm{d}\mathbf{S} = q\Phi. \tag{2.63}$$

The quantity Φ is the magnetic flux enclosed by the drift path. Therefore, the third invariant is often called the flux invariant and is usually denoted by Φ, omitting the charge q:

$$\Phi = \oint \mathbf{B} \cdot \mathrm{d}\mathbf{S}. \tag{2.64}$$

An approximate expression for the drift period τ_d provided by Walt (1994) and accurate to $\sim 0.5\%$ is:

$$\tau_d = 1.557 \times 10^4 \cdot \left(\frac{\mathrm{R_E}}{R_0}\right) \frac{1}{\gamma\beta^2}[1 - 0.3333\sin^{0.62}\alpha_{\mathrm{eq}}], \tag{2.65}$$

where $\gamma = 1/\sqrt{1 - \frac{v^2}{c^2}}$ is the relativistic factor. As R_0 increases, the drift period decreases, and as the particle velocity increases, the drift period also decreases. The pitch-angle dependence of equation 2.65 shows that particles with 90° equatorial pitch angle drift more rapidly than those mirroring at higher latitudes.

The conservation of the third adiabatic invariant implies that the total amount of flux enclosed within a particle drift shell is constant, if large scale changes of the magnetic field occur on time scales longer than the particle's drift period τ_d. For a dipole field, this requires the drift orbit to be circular and axisymmetric. Based on this, McIlwain (1961) introduced the parameter L, which corresponds to the equatorial radius of a drift shell assuming a dipole for the geomagnetic field and is related to radial distance r and colatitude θ as follows:

$$L = \frac{r}{\mathrm{R_E} \sin^2\theta}. \tag{2.66}$$

The parameter L has units of $\mathrm{R_E}$ and is known as McIlwain's L value (McIlwain, 1961).

A variation of the third adiabatic invariant Φ is the Roederer L^* parameter, which is found by slowly turning off all external field sources in a realistic magnetic field, allowing for an adiabatic change of the trapped particle from a realistic field to a dipole field. Physically, L^* represents the radial distance (in $\mathrm{R_E}$) to the equatorial points of the symmetric shell on which a charged particle would be located if all the non-dipole components of the trapping magnetic field were adiabatically removed. L^* is defined in terms of the field strength B_0 at the magnetic equator on the Earth's surface and the third invariant Φ as (Roederer and Zhang, 2016):

$$L^* = \frac{2\pi B_0 {\mathrm{R_E}}^2}{\Phi}. \tag{2.67}$$

In a perfect dipole field the Roederer L^* is equal to the McIlwain L parameter. An advantage of employing L^* instead of L for studying geomagnetically trapped particles is that, at a constant L^* value, changes in the particle population due to adiabatic variations in the magnetic field can be filtered out. Moreover, in a static or slowly changing magnetic field, a charged particle follows constant L^* for its entire drift path.

Typical frequencies of relativistic ($\sim$ 1 MeV) electrons at $L \sim 4$ to $L \sim 5$ are: $\sim$ kHz for gyration, $\sim$ Hz for bounce motion, and $\sim$ mHz for the gradient-curvature drift. These frequencies are approximately separated by three orders of magnitude, which implies that in a dipole (or approximately dipole) field, the motions corresponding to the three adiabatic invariants are decoupled and do not affect each other. This also means that it is possible to violate higher adiabatic invariants without altering lower invariants. For example, ultra-low frequency (ULF) waves (see Section 3.2.2) can violate the third invariant without changing the first or second invariant, through resonant wave-particle interactions with the gradient-curvature drift motion (Ukhorskiy and Sitnov, 2012).

2.3 The Solar-Terrestrial Environment

The solar-terrestrial environment, also known as geospace, comprises the upper part of the terrestrial atmosphere, the outer part of the geomagnetic field, and the solar emissions that affect them. This is a region of interactions and boundaries: interactions between terrestrial matter and solar radiation, between terrestrial and solar magnetic fields, between electric and magnetic fields and charged particles; and boundaries between terrestrial and solar matter, and between regions dominated by various patterns of flow (Hargreaves, 1992). All these interactions ultimately drive

space weather effects that can influence the performance and reliability of ground-based and space-borne technological systems and endanger human life.

In this section, an overview of the solar-terrestrial environment is provided. First, the Sun and its emissions are briefly discussed, followed by a description of the intrinsic geomagnetic field. Then, the interaction between the solar wind and the geomagnetic field is described and several plasma populations arising from this interaction are presented. Finally, geomagnetic storms and substorms are introduced, and several indices employed to characterise these phenomena are reviewed.

2.3.1 The Sun and the Solar Wind

The Sun constantly ejects plasma at supersonic speeds of approximately 400 km/s (Russell, Luhmann, and Strangeway, 2016) as a result of the expansion of the solar corona. This radial outflow of plasma from the Sun is known as the solar wind, and it primarily consists of electrons and protons, with a small admixture of 5% helium ions. Typical values of the electron temperature and the density in the solar wind near the Earth are $T_e \sim 10^5$ K and $n_e \sim 5$ cm^{-3}, respectively. Due to the high conductivity of the solar wind, the solar magnetic field is transported outwards by the expanding solar wind flow, gradually becoming the interplanetary magnetic field (IMF). Near Earth's orbit the IMF is of the order of ~ 5 nT, although it may fluctuate between 3 nT and occasionally 12 nT (Baumjohann and Treumann, 2012).

The solar wind is normally separated in virtue of its speed into two components, the slow and the fast solar wind. Slow solar wind streams usually have low speed ($<$350 km/s), whereas fast solar wind streams can reach speeds of up to 700 km/s or more (Kivelson and Russell, 1995; Russell, Luhmann, and Strangeway, 2016). The fast solar wind originates from coronal holes on the solar surface. These are regions of open solar magnetic field lines that extend outwards into space. The interaction between fast and slow solar wind results in a stream interface, which typically corresponds to an increase in the solar wind speed and temperature and a decrease in the density (Kataoka and Miyoshi, 2006). This structure is known as a Corotating Interaction Region (CIR) and may recur with a $\sim$ 27 day period (Denton et al., 2006). Coronal holes are relatively stable and can last multiple solar rotations, and thus, their associated CIR may also be observed periodically.

Another example of solar activity are Coronal Mass Ejections (CMEs). These phenomena occur when coronal material is catastrophically ejected from the Sun. CMEs are preceded in time by a sheath of compressed solar wind, which itself is preceded by an interplanetary shock (Borovsky and Denton, 2006). Besides releasing large quantities of matter into space, CMEs are also usually accompanied by electromagnetic radiation. Sudden increases in the IMF strength, solar wind speed, density, and temperature typically signal the occurrence of an interplanetary shock prior to the arrival of a CME (Kataoka and Miyoshi, 2006).

2.3.2 The Earth's Magnetic Field

The Earth's magnetic field, also known as the geomagnetic field, is generated by a number of current systems. By far the primary component of the geomagnetic field stems from the convective motion of conductors, deep in the Earth's fluid outer core. In addition to this source, the geomagnetic field also has components in the crust, the ionosphere, and the magnetosphere. At the Earth's surface the main field can be approximated by a dipole located at the Earth's centre with its magnetic axis offset from the rotation axis by about 11°.

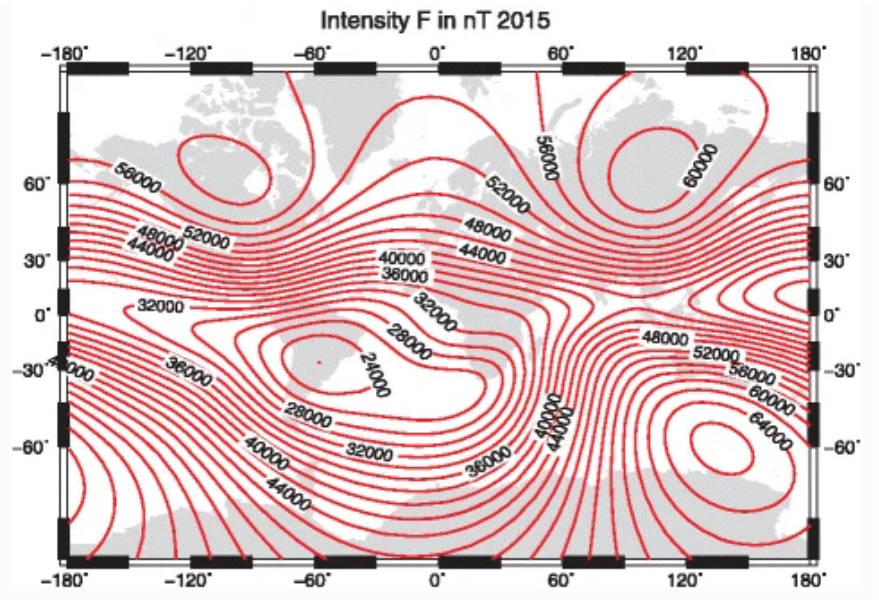

FIGURE 2.7: Map of the total magnetic field intensity at the Earth's surface in 2015 in a Mercator projection. The red dot indicates the minimum intensity. The magnetic field intensities are given in units of nT (Thébault et al., 2015).

If the geomagnetic field were a pure dipole located at the centre of the Earth, contours of constant magnetic field intensity on the Earth's surface would be lines of constant latitude. Nevertheless, due to asymmetries in the interior currents the actual isointensity lines are as depicted in Figure 2.7. The north and south magnetic poles are located over the Canadian Arctic and off the coast of Antarctica, respectively. One particular interesting feature is a large region of reduced field intensity on the east coast of South America, the so-called South Atlantic Anomaly (SAA), over which trapped charged particles mirror at lower altitudes. As a consequence, this is the region where low-Earth orbit (LEO) spacecraft encounter the most intense particle fluxes (Baker et al., 2018).

2.3.3 The Magnetosphere

When the fast moving, magnetised solar wind impinges on the geomagnetic field, it cannot penetrate the field, but rather is decelerated and diverted around it, as shown in Figure 2.8. The solar wind slows abruptly from supersonic to subsonic speeds, producing a bow shock in front of the Earth, where part of the kinetic energy of the solar wind particles is converted into thermal energy. The extended region of subsonic plasma between the bow shock and the outer boundary of the geomagnetic field is called the magnetosheath.

The magnetosphere is the cavity surrounding the Earth where the geomagnetic field is dominant, and a schematic representation of this region is presented in Figure 2.8. The region where the solar wind dynamic pressure is balanced by the pressure created by the geomagnetic field is called the magnetopause. This boundary separates the charged particles forming the solar wind from those trapped in the geomagnetic field. The kinetic pressure of the solar wind distorts the outer part of the dipole-like shape of the geomagnetic field. This interaction acts to compress the field at the dayside, whereas the nightside magnetic field is elongated and stretched out into the magnetotail which reaches beyond the lunar orbit. The outer part

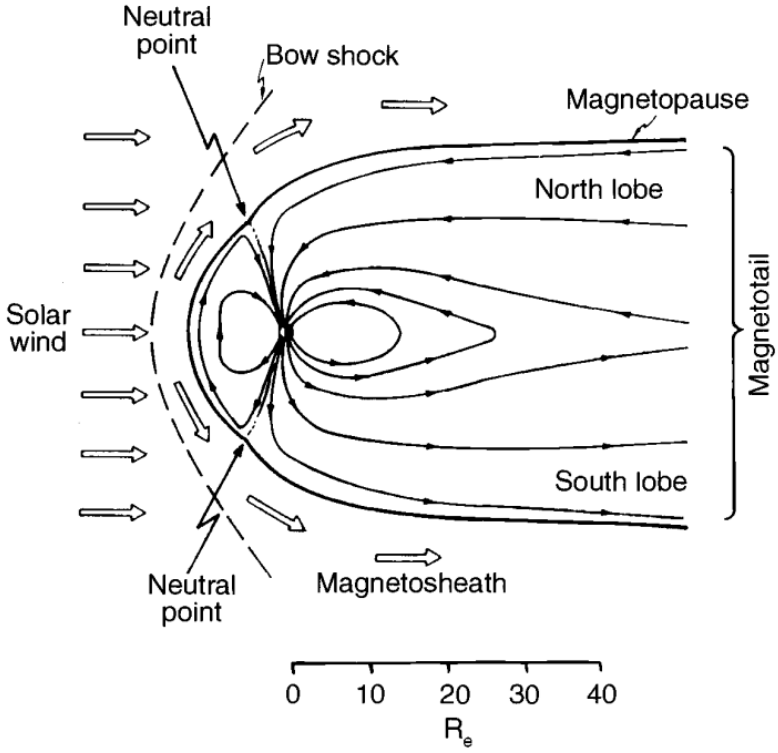

FIGURE 2.8: Schematic representation of the noon-midnight cross section of the magnetosphere (Gombosi, 1998).

of the magnetotail is called the lobe and contains a very low dense plasma, with typical values of electron density and temperature and magnetic field strength of $n_e \sim 10^{-2}$ cm^{-3}, $T_e \sim 5 \times 10^5$ K, and $B \sim 30$ nT, respectively.

The plasma inside the magnetosphere is composed mainly of electrons and protons, whose main sources are the solar wind and the terrestrial ionosphere. Additionally, there are also small fractions of He^+ and O^+ ions of ionospheric origin and He^{++} ions from the solar wind. The plasma inside the magnetosphere is not homogeneously distributed, but is rather grouped into different regions with a variety of densities and temperatures. Some of these regions are depicted in Figure 2.9 and are

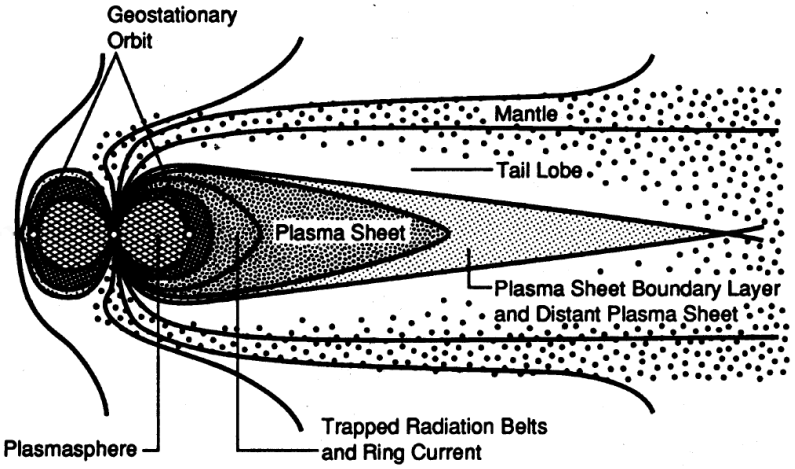

FIGURE 2.9: Schematic representation of plasma regions in the magnetosphere as viewed in the noon-midnight meridian plane (Kivelson and Russell, 1995).

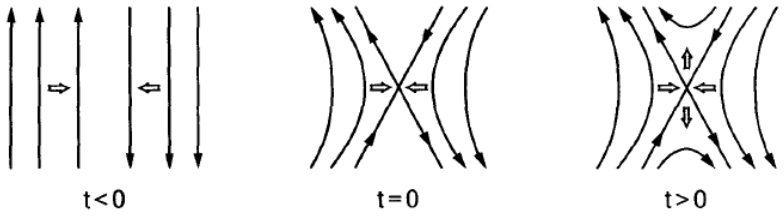

FIGURE 2.10: Schematic representation of the evolution of reconnection of antiparallel magnetic field lines (Baumjohann and Treumann, 2012).

described in the next sections.

2.3.3.1 Magnetic Reconnection and the Dungey Cycle

Magnetic reconnection is a process in which antiparallel field lines embedded in two approaching plasma streams merge and reconnect to other lines, therefore changing the magnetic topology. Consider the antiparallel field lines as depicted in the left-hand sketch of Figure 2.10. For $t < 0$ the two lines move towards each other. At $t = 0$ (middle panel), both encounter each other, and the net magnetic field is zero at the point where they intersect. This particular location is called a magnetic neutral point. For $t > 0$ (right panel), at the neutral point, the antiparallel lines are split into halves and the halves from one side are reconnected to those from the other side. The reconnected field lines are then expelled from the neutral point (as shown by the upward and downwards arrows), and are populated with a mixture of plasma from both approaching streams.

Reconnection of antiparallel magnetic field lines occurs at the dayside magnetosphere, where the northward geomagnetic field lines merge with the southward IMF (denoted by 1 in Figure 2.11), a process originally suggested by Dungey (1961). Both reconnected field lines split into the two open field lines labelled as 2, each of which has one end stretching out into the solar wind and the other connected to the Earth. The solar wind then transports this field line downtail across the polar cap (lines 3 to 6).

In the nightside of the magnetosphere, around 100 to 200 R_E downtail, antiparallel field lines are again in close proximity, and by the same physical process as in the dayside magnetosphere, the two open field line halves meet again and reconnect. The result is a closed and stretched terrestrial field line in the magnetotail and an open solar wind field line (marked by 7 and 8). The magnetic stretched tail line denoted by 8 relaxes owing to magnetic tension and shortens earthwards, transporting plasma with it. This large scale motion of plasma and magnetic field from the dayside magnetosphere, across the polar cap towards the magnetotail, and back around the flanks to the dayside, is known as the Dungey cycle.

2.3.3.2 Convection and Corotation Electric Field

The concurrent drift of plasma in the field lines as a whole is called plasma convection, and its ultimate driver in the Earth's magnetosphere is the momentum of the solar wind flow (Baumjohann and Treumann, 2012). An observer on Earth's fixed frame of reference will detect an electric field $\mathbf{E}_{\text{conv}} = -\mathbf{v} \times \mathbf{B}$ through the Lorentz transformation. $\mathbf{E}_{\text{conv}}$ is the convection electric field and in the equatorial plane it points in the dawn-to-dusk direction. Electric equipotential contours of a uniform

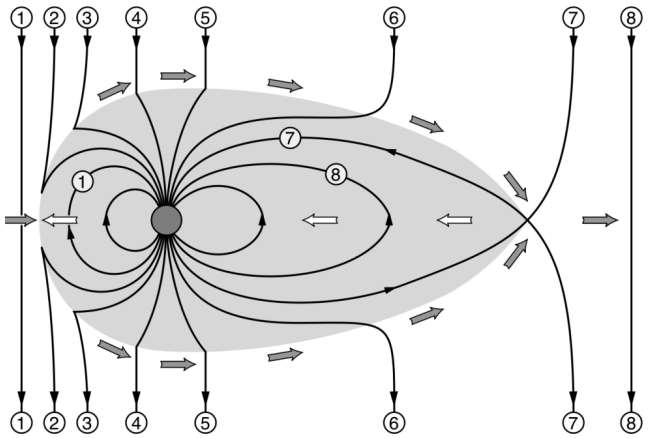

FIGURE 2.11: Diagram of the noon-midnight meridian cross-section of the magnetosphere, showing the Dungey cycle and the field line reconnection (Baumjohann and Treumann, 2012).

convection electric field in the equatorial plane are presented in the left panel of Figure 2.12.

Near the Earth, there is an additional electric field that generates plasma motion. This field is also caused by a movement of the field lines and the plasma tied to them. In this case the plasma motion is due to the Earth's rotation, and the resulting electric field is called corotation electric field. For a non-corotating observer, this field is given by $\mathbf{E}_{\text{cor}} = -(\mathbf{\Omega}_{\text{E}} \times \mathbf{r}) \times \mathbf{B}$, where $\mathbf{E}_{\text{cor}}$ is the corotation field, $\mathbf{\Omega}_{\text{E}}$ is the angular velocity of Earth's rotation, and $\mathbf{r}$ points radially from the center of the Earth. The corotation electric field is directed radially inward at the equator and produces a drift that causes charged particles to corotate with the Earth. The middle panel of Figure 2.12 shows equipotential contours for the corotation electric field.

The total electric field is the superposition of both the convection and the corotation fields, as depicted in the right panel of Figure 2.12. Since the corotation electric potential decreases radially, this leads to a weakening of the influence of corotation with distance. As a result, and ignoring the magnetic drifts presented in Sections 2.1.3.2 and 2.1.3.3, charged particles close to Earth corotate under the influence of the corotation electric field, and move on closed drift paths around the Earth. At larger distances the electric potential is dominated by the convection electric field, and charged particles will drift from the nightside out through the magnetopause

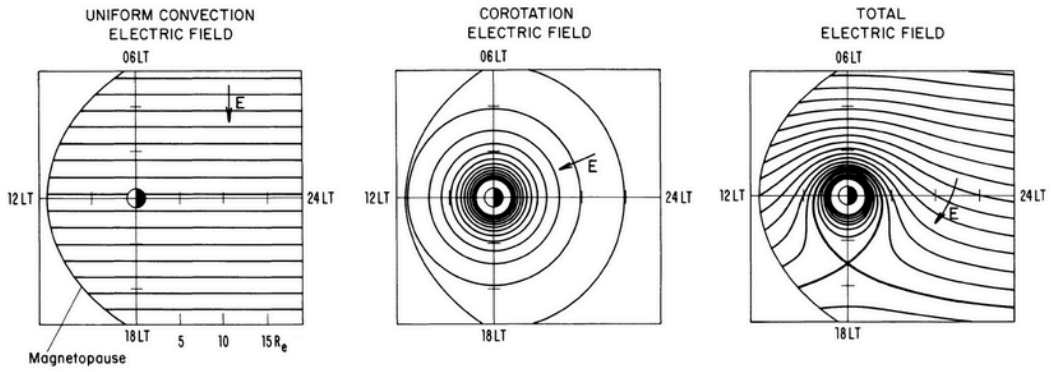

FIGURE 2.12: Equipotential contours of the magnetospheric electric fields in the equatorial plane (Lyons and Williams, 1984).

on open drift paths. A separatrix, known as the Alfvén layer, separates the region where the corotation electric field is dominant, causing closed drift paths, from the region where the convection electric field dominates, and particles drift on open paths, ultimately being lost to the magnetopause.

2.3.3.3 The Plasmasphere

As illustrated in Figure 2.12, there is a region close to the Earth where the equipotential contours are closed and ions and electrons corotate with the Earth. This region is known as the plasmasphere (Figure 2.9), and can be considered as the upwards extension of the ionosphere. In comparison with other plasma populations in the magnetosphere, the plasmasphere is considered cold, with energies in the range of 1 eV (Baumjohann and Treumann, 2012). It is precisely due to the low particle energies that the $\mathbf{E} \times \mathbf{B}$ drift dominates over the gradient and the curvature drift and that particles follow the contours shown in the right panel of Figure 2.12. Owing to the closed particle drift paths, the plasma density in the magnetosphere is of several 10^3 cm^{-3}, significantly larger than the density in the surrounding magnetosphere. The edge of the plasmasphere, known as the plasmapause, is defined by a steep density gradient.

The location of the plasmapause is not constant in time, but rather dependent on solar wind conditions and geomagnetic activity. When the convection electric field increases, the radius of the plasmasphere decreases, and the Alfvén layer moves closer to the Earth. During active periods, e.g. geomagnetic storms, the plasmasphere may shed some of its mass to the magnetosphere and ultimately to the dayside magnetopause, forming a tail-like structure between the plasmasphere and the magnetosphere known as drainage plume. As the enhanced convection electric field subsides, the plasmasphere expands and slowly refills with material from the ionosphere. Park (1974) estimated that the time required for the refilling depends on the L shell, ranging from $\sim$ 1 day at $L = 2.5$ to $\sim$ 8 days at $L = 4$.

2.3.3.4 The Plasmasheet

Most of the plasma in the magnetotail is concentrated around the tail mid-plane in an about 10 R_E thick region known as the plasmasheet (Figure 2.9), which extends far out into the nightside. Average electron densities and temperatures in the plasmasheet are $n_e \sim 0.5$ cm^{-3} and $T_e \sim 5 \times 10^6$ K, with $B \sim 10$ nT (Baumjohann and Treumann, 2012). The plasmasheet consists of both electrons and ions with energies of a few keV, which originate from both the solar wind (via reconnection in the magnetotail) and the ionosphere (via outflow from the polar cap regions).

Since the plasmasheet connects the inner and the outer magnetosphere, it provides a means for the redistribution of energy. The plasmasheet lies between the two oppositely directed magnetic lobes, which can reconnect and then return to dipole form, transferring energy to the plasma. Material in the newly reconnected magnetic field lines convect inwards, to the inner magnetosphere, while a parcel of plasma and magnetic field that does not connect to the Earth or solar wind, known as plasmoid, is ejected downtail. The plasma that is transported earthwards is heated adiabatically during the convective $\mathbf{E} \times \mathbf{B}$-drift inward transport, supplying a source of ring current particles (Baumjohann and Treumann, 2012). Furthermore, the plasmasheet is also considered a source population for the radiation belts (Ganushkina et al., 2014) during times of enhanced convection electric field (Friedel et al., 2001) as

well as substorm injections, followed by acceleration to radiation belt energies via wave-particle interactions (e.g. Boyd et al., 2014; Jaynes et al., 2015).

2.3.3.5 The Ring Current

As presented in Sections 2.1.3.2 and 2.1.3.3, both the gradient and curvature drifts are charge-dependent. The result is that, for particles at energies where magnetic drifts dominate the drift motion, electrons and ions travel azimuthally in opposite directions around the Earth. This differential motion of charged particles results in a westward directed electric current called the ring current, extending at geocentric distances between 2 R_E and 9 R_E (Daglis et al., 1999). As prescribed by Ampere's law, this current creates a magnetic field, which opposes and weakens the geomagnetic field at the equator. Dessler and Parker (1959) and Sckopke (1966) showed theoretically that larger disturbances of the equatorial geomagnetic field during storms are proportional to the total energy of the ring current particles.

Although all trapped particles in the inner magnetosphere contribute to the ring current, it is primarily 10 to 200 keV H^+ and O^+ ions that contribute to the total current density (Gombosi, 1998). The particle sources of the ring current are the plasmasheet and the ionosphere. As explained in Section 2.3.3.4, during the inward transport of particles, the magnetic field increases causing the particles to be adiabatically heated. Such process creates the tens to hundreds of keV ring current ions from the 1 to 10 keV plasmasheet ions (Baumjohann and Treumann, 2012). An additional source of ring current particles is the ionospheric outflow. A variety of successive acceleration mechanisms act on the ionospheric particles to raise their energy from $\sim$ 1 eV to tens of keV (Daglis et al., 1999). As a result, these particles flow up the magnetic field lines and out into the inner magnetosphere, where they may undergo azimuthal drift motion, and hence, contribute to the ring current.

2.3.3.6 The Radiation Belts

The Van Allen radiation belts consist of energetic electrons and protons trapped by the geomagnetic field. They were first discovered when the Geiger counters onboard Explorer 1, a satellite designed to study cosmic ray access to Earth and launched in January 1958, became unexpectedly saturated (Van Allen et al., 1958). The Soviet Sputnik 2 spacecraft launched in November 1957 performed similar measurements (Vernov and Chudakov, 1960). Further missions mapped out the region where these energetic particles are trapped within the magnetosphere, and discovered two toroidal shaped regions (the inner and the outer belt) with a sparsely populated slot region between them, as shown schematically in Figure 2.13.

The inner radiation belt typically extends from $\sim$ 1000 km to $\sim$ 2 R_E and is primarily dominated by highly energetic protons produced by cosmic ray albedo neutron decay (CRAND, Singer, 1958). Solar energetic protons associated with CMEs also become trapped by the geomagnetic field (Hudson et al., 1997) and are the primary source at $E < 50$ MeV for the inner zone (Selesnick, Looper, and Mewaldt, 2007).

Electrons are also found in the inner belt, primarily resulting from the transport of electrons from the outer zone into the inner zone (Li and Hudson, 2019). The viability of CRAND as a source of electrons remains uncertain. Selesnick (2015) showed that neutron albedo generated electrons are too low to account for the observed $E < 1$ MeV inner zone electron fluxes. Recent studies (e.g. Li et al., 2015; Fennell et al., 2015) employed measurements from the twin Van Allen Probes and

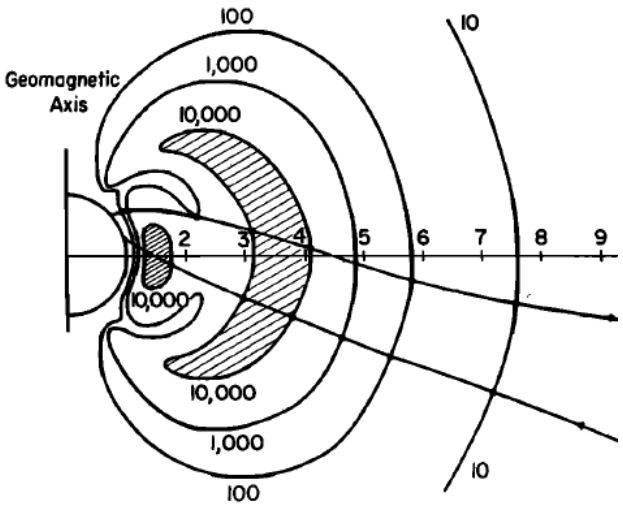

FIGURE 2.13: Diagram showing contours of constant intensity of the trapped radiation from the true counting rates of Geiger tubes carried by Explorer 4 and Pioneer 3. Also shown are the outbound and inbound legs of the trajectory of Pioneer 3. The inner and outer belts are visible, separated by the slot region (Van Allen, 1959).

found that there are essentially no, or very few, $E > 1$ MeV electrons present. This mission has also yielded the concept of "impenetrable barrier", in which loss to the atmosphere dominates the rate of inward radial transport for energies greater than 1 MeV (Baker et al., 2014; Fennell et al., 2015). There are episodic incursions of $E > 1$ MeV electrons into low L regions and into the inner zone, but their presence is not the norm (Baker et al., 2018). For instance, in June 2015, MeV electrons were injected into the inner zone and persisted for months at $L \sim 1.75$ (Claudepierre et al., 2017). In general, the lower the electron energy, the more common are such injections to the lowest L values. Turner et al. (2017) studied "sudden particle enhancements at low L" as a source of inner zone electrons and concluded that enhancements occurred more often for $E < 600$ keV electrons than for those with $E > 600$ keV.

Beyond the inner radiation belt lies the slot region, which extends from roughly $L \sim 2$ to $L \sim 3$ (Baker et al., 2018) and is relatively devoid of energetic electrons. The slot region is formed by a balance between loss to the atmosphere due to pitch-angle scattering and inward radial diffusion (Lyons and Thorne, 1973). However, during strong geomagnetic storms, the slot region can be filled by moderate, and even high energy electrons (e.g. Fennell et al., 2005; Turner et al., 2017).

Finally, the outer radiation belt ranges from $L \sim 3$ to $L \sim 8$ with a flux peak at $L \sim 4$ (Li and Hudson, 2019). This region comprises electrons in the energy range from 1 keV to $\sim$ 10 MeV and varies widely in particle intensity. Compared to the inner belt, fluxes in the outer zone are highly variable (e.g. Rothwell and McIlwain, 1960; Craven, 1966) and dependent on geomagnetic storm time processes (Baker et al., 1986), which leads both to significant electron acceleration and loss in the inner magnetosphere. Fluxes may vary dramatically by up to several orders of magnitude on temporal scales ranging from hours to days, and they can also exhibit significant variations in extent. This high degree of variability is an area of active ongoing research. Many different source and loss processes have been identified and are discussed in Chapter 3.

A large number of commercial, military, and scientific satellites operate in geosynchronous orbit (GEO), medium-Earth orbit (MEO), and low-Earth orbit (LEO). All

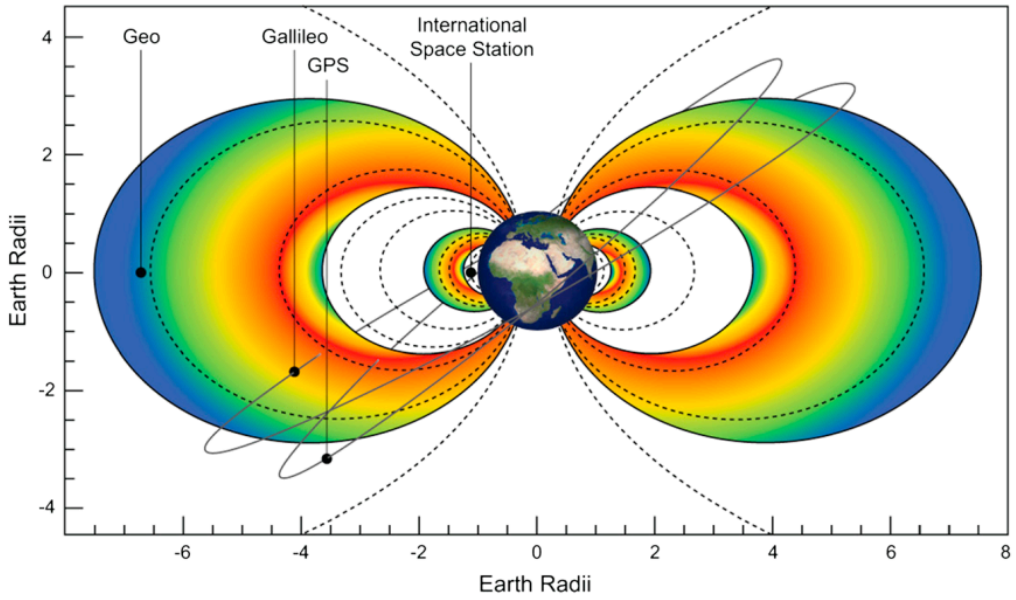

FIGURE 2.14: Schematic of the Earth's radiation belts and slot region, together with the principle satellite orbits which traverse them (Horne et al., 2013).

of these spacecraft and their components such as hardware, solar cells, and integrated circuits, can be damaged by charged particle populations. Figure 2.14 shows a schematic of the Earth's electron radiation belts, together with the main satellite orbits which traverse them. Most telecommunications satellites are located at GEO, at the outer edge of the outer radiation belt. In contrast, most navigation satellites, such as Global Positioning System (GPS) and Galileo, operate in MEO, and therefore they pass through the heart of the outer belt where they may experience much higher levels of radiation. The International Space Station and most Earth-observation satellites operate in LEO and may also experience higher levels of radiation if their orbits traverse the auroral zones or the SAA (Horne et al., 2013). As a result, radiation belt formation, dynamics, and variability are currently of high interest to the scientific community.

2.3.3.7 Geomagnetic Storms

Geomagnetic storms are large, prolonged disturbances of the magnetosphere caused by fluctuations in the solar wind. Many magnetic storms follow CMEs or CIRs (e.g. Borovsky and Denton, 2006; Denton et al., 2006), which produce large interplanetary disturbances that interact with the magnetosphere and drive significant intensifications of the ring current. Figure 2.15 shows an example of a geomagnetic storm and its three distinct phases, as characterised by the *Dst* index (see Section 2.3.4.2).

The initial phase (which does not occur necessarily in all storms) is related to the impulse from the interplanetary disturbance and the consequent compression of the magnetosphere. This phase is observed as a sudden increase in the horizontal component of the geomagnetic field (*H* component), due to an increase in the Chapman-Ferraro currents. This sudden commencement has a typical rise time of a few minutes. The initial phase normally lasts between two to eight hours (Gombosi, 1998).

Most geomagnetic storms are associated with long periods when the IMF has a significant southward component, which is the most favourable configuration for

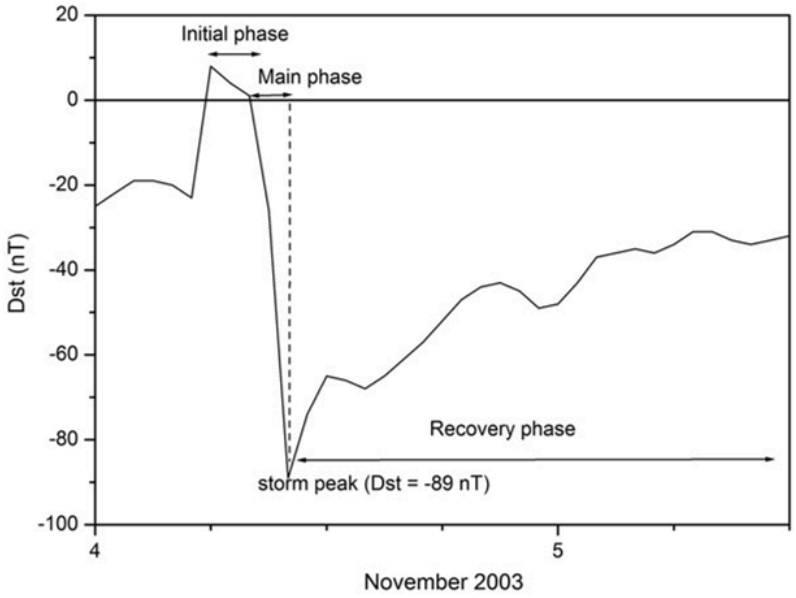

FIGURE 2.15: Example of a geomagnetic storm (04 to 05 November 2003). The initial, main, and recovery phases are highlighted (Echer, Gonzalez, and Tsurutani, 2011).

reconnection at the dayside magnetopause. As a result, extended periods of southward IMF lead to the main phase of storms. The increased dayside reconnection intensifies magnetospheric convection, and consequently, the enhanced duskward electric field increases the amount of particles injected into the ring current. As mentioned in Section 2.3.3.5, the ring current causes a decrease in the horizontal component of the geomagnetic field, measured by the *Dst* index. The main phase corresponds to the time period when the ring current intensifies, and it typically lasts from a few hours to about a day.

As soon as the southward component of the IMF weakens or turns northward, the ring current starts to decay, as particles are lost faster than they are supplied. The decay processes for the ring current include charge exchange, Coulomb collisions within the plasmasphere, and resonant interactions with plasma waves (Gonzalez et al., 1994). Additionally, the horizontal component of the geomagnetic field gradually returns to its normal pre-storm value. This period is known as the recovery phase of the magnetic storm, and it normally extends for several days.

2.3.3.8 Substorms

In Section 2.3.3.1 convection was treated as a stationary process. The magnetic merging between IMF and geomagnetic field lines at the dayside magnetopause was assumed to occur always at the same rate, and dayside and nightside reconnection in the magnetotail were considered to be in equilibrium. If the opening of magnetic flux in the dayside is relatively equal to the closing of magnetic flux on the nightside over an extended period of time, then the polar cap is approximately stable in size, since the amount of open flux is constant.

In contrast, if the rate of dayside reconnection is greater than that occurring in the magnetotail and thus, an unbalanced reconnection rate arises, a substorm may occur. This phenomenon, termed by S. Chapman, normally consists of three phases: growth, expansion, and recovery.

The substorm growth phase is usually triggered by a southward turning of the IMF. Dayside reconnection rate is enhanced, dominating over nightside reconnection. The flux eroded on the dayside magnetopause is transported towards the tail. Part of the flux is reconnected and convected back to the dayside magnetosphere. At the same time, the magnetic flux which is not reconnected accumulates in the tail lobes, causing the polar cap to expand to lower latitudes. The enhanced magnetic field in the tail lobes stretches the field lines in the plasmasheet into a more tail-like configuration. The growth phase normally lasts for an hour. During this period, the aurora appears in the sky in the form of auroral arcs (Gombosi, 1998).

The start of the expansion phase is marked by the substorm onset, although there is controversy as to which exact process triggers it. This time is observed as a sudden brightening of one of the auroral arcs in the midnight sector. At this point, too much magnetic flux has been accumulated in the magnetotail, that it becomes unstable and tries to release its surplus energy. In addition to the increased auroral activity, the enhanced nightside reconnection rapidly closes the open magnetic flux in the tail, and the stretched magnetic field in the plasmasheet becomes more dipolar again. This allows material on the newly reconnected field lines to convect towards the Earth, as well as ejecting a plasmoid tailward downstream in the solar wind. During the expansion phase ions and electrons from the plasmasheet are injected into the inner magnetosphere (Akasofu, 1964; McPherron, Russell, and Aubry, 1973). The substorm expansion phase typically lasts about 30 to 60 minutes (Baumjohann and Treumann, 2012).

About an hour after the substorm onset, the aurora starts to fade, the polar cap contracts and retreats to higher latitudes, and the recovery begins. Typically this phase lasts from one to two hours and ends when the magnetosphere returns to a quiet state.

2.3.4 Geomagnetic Indices

Geomagnetic indices are used to quantify and characterise the disturbed states of the near-Earth plasma environment presented in the previous section. The three most commonly used indices are AE, Dst, and Kp, and they are derived from ground-based magnetic records obtained from equatorial to polar regions.

2.3.4.1 AE Index

The AE index, first introduced by Davis and Sugiura (1966), is a measure of global auroral electrojet activity. Its name refers to ionospheric currents in the auroral region that become enhanced due to increased conductivity during substorms, discussed in Section 2.3.3.8. These currents produce deviations in the geomagnetic field that can be measured by ground-based instrumentation in the auroral zone. AE is based on one-minute readings of the H component, of 12 auroral zone observatories located between about 65° to 70° magnetic latitude. For each of these individual measurements, the average intensity of the five geomagnetically quietest days of the preceding month is subtracted as a baseline correction. The largest and smallest deviations in the H component at each one-minute time window are selected, and AE is defined as the difference between them. This index provides a good proxy for wave-particle interactions (e.g. Meredith et al., 2004; Shprits, Meredith, and Thorne, 2007; Usanova et al., 2012), as it is related to substorm activity and thus, is also associated with the generation of various types of plasma waves, some of which are introduced in the next chapter.

2.3.4.2 Dst Index

The disturbance storm time (*Dst*) index was introduced by Sugiura (1964) to measure the magnetic field and total energy of the westward magnetospheric equatorial ring current. As previously mentioned, the enhancement of the ring current is associated with a reduction of the geomagnetic field during a magnetic storm, since both fields are opposed. As a consequence, *Dst* is typically negative, where a larger negative value indicates a more intense storm. The evolution of *Dst* for a storm on 04 and 05 November 2003 is presented in Figure 2.15.

Dst is derived from hourly averages of the *H* component at four low-latitude observatories, located between 20° and 30° away from the magnetic equator. A quiet time reference baseline is subtracted from data from each observatory. All four magnetic disturbances are then averaged over all four stations, to further reduce local time effects, and multiplied with a correction factor for the variation in latitude. The average of all data defines the *Dst* index, which is often used as a proxy of the ring current intensity and for parametrising the magnitude of geomagnetic storms. Gonzalez et al. (1994) introduced a classification of storms into weak, moderate, and intense, according to the minimum *Dst* reached during the main phase.

2.3.4.3 Kp Index

The *K* index is intended to quantify the disturbance level in the *H* component of the geomagnetic field during storm time activity as measured by a mid-latitude ground-based magnetometer in a three-hour interval, relative to a quiet day (Bartels, Heck, and Johnston, 1939). The total maximum fluctuation is determined by adding together the maximum positive and negative excursions during the three-hour period. The maximum fluctuation is then converted, by means of reference tables specific to each observatory, to a *K* index on a nine-point logarithmic scale, ranging from 0 to 9 with plus and minus designations given between two intervals.

The construction of the planetary *K* index, the Kp, aims to express the worlwide features in geomagnetic disturbances (Bartels and Veldkamp, 1949). The construction of Kp involves the mean of the standardised *K* indices from 13 observatories located between 44° and 60° northern or southern geomagnetic latitude. A $Kp \gtrsim 4$ typically indicates a geomagnetic storm.

Chapter 3

Dynamics of the Outer Electron Radiation Belt

The motion of an individual charged particle in magnetic and electric fields was described in Chapter 2. However, a great number of particles populate the Van Allen belts, and the measurement and description of trapped radiation involves large numbers of particles distributed in space, energy, and pitch angle. Hence, the concept of flux is often used to describe the intensity and characteristics of populations of trapped particles.

The first section of this chapter presents the definition of flux, and shows two examples of the variability of the electron flux in the outer radiation belt as observed by orbiting spacecraft. Then, the theory behind resonant interactions for efficient energy transfer between particles and waves is introduced, and some of the most important magnetospheric plasma waves that can contribute to outer radiation belt variations are outlined. Furthermore, the current understanding of dominant source and loss processes responsible for the variability of electrons in the outer belt is summarised. Finally, the concept of phase space density is introduced, along with its applicability as a tool to distinguish between various mechanisms operating in the outer belt.

3.1 Observations of the Outer Electron Radiation Belt

The description of the particles that populate the radiation belts involve a vast number of them distributed in space, energy, and pitch angle. Therefore, the concept of flux has been introduced in order to describe the content of the Van Allen belts, as well as the intensity and characteristics of this trapped population. This concept is closely related to the output of most space radiation detectors.

For a given location, direction, and energy, the differential directional flux is the number of particles at energy E within unit $\mathrm{d}E$ which cross a unit area perpendicular to the specified direction within a unit solid angle in 1 s. If $\mathrm{d}A$ is an area element, and $\mathrm{d}\Omega$ is an element of solid angle in the direction $\hat{\theta}$, then, at location $\mathbf{r}$ the number of electrons with energies in the range between E and $E + \mathrm{d}E$ passing through $\mathrm{d}A$ in the direction $\hat{\theta}$ within $\mathrm{d}\Omega$ per unit time is (Walt, 1994):

$$\mathrm{d}N(\mathbf{r}, E, \theta) = j(E, \theta)\mathrm{d}A\mathrm{d}E\mathrm{d}\Omega\mathrm{d}t, \tag{3.1}$$

where $j(E, \theta)$ is the differential, directional flux. It is usually presented in units of $\mathrm{cm}^{-2}\mathrm{s}^{-1}\mathrm{sr}^{-1}\mathrm{keV}^{-1}$, and its direction is often given by the particle pitch angle α.

Electron fluxes in the outer radiation belt are highly dynamic in space and time, and geomagnetic activity is the primary cause of these variations. For instance, Figure 3.1 (Xiang et al., 2017) presents a flux dropout event (i.e. a rapid, drastic decrease

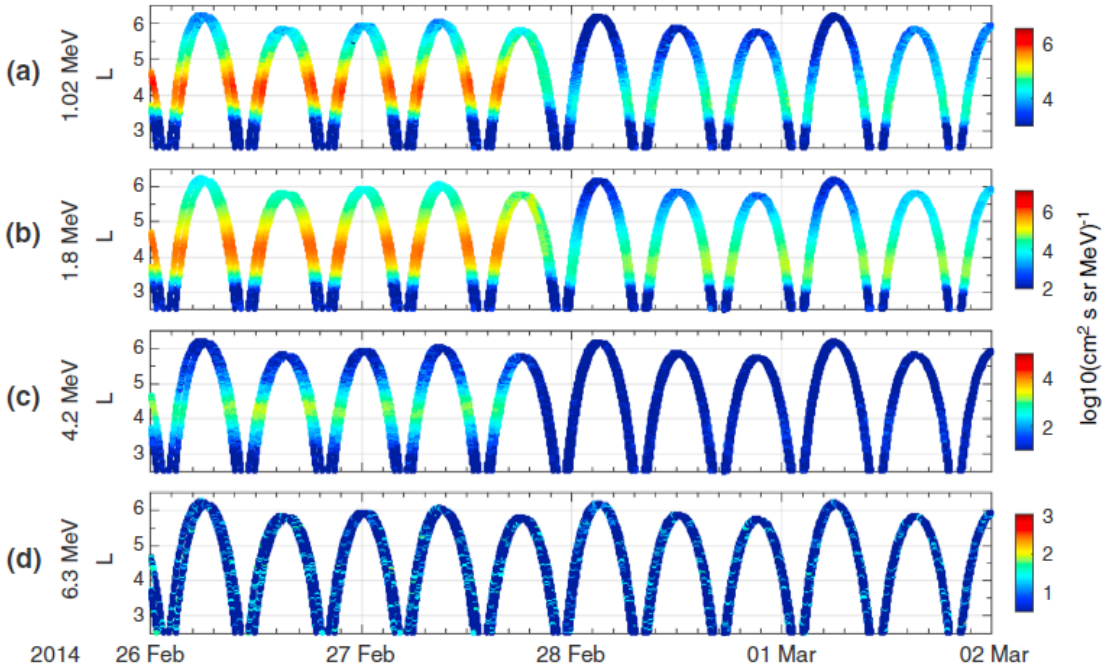

FIGURE 3.1: Flux of electrons at 90° pitch angle as a function of L and time from 26 February to 01 March 2014 measured by the Van Allen Probes. The energy channels are indicated for each panel (Xiang et al., 2017).

in the intensity of the electron radiation belt in only a few hours). This dropout, measured by the Van Allen Probes (Mauk et al., 2012; Stratton, Harvey, and Heyler, 2012), exhibited energy-dependent flux depletions. *Dst* (not shown) reached its minimum value of -101 nT on 27 February 2014 23 UT. The flux of 4.2 MeV electrons showed a substantial drop above $L = 3.3$ late on that same day, and remained low until the end of the period. In contrast, the flux of 1.02 MeV and 1.08 MeV only exhibited a moderate decrease, and gradually started to recover towards 01 March. For this event, Xiang et al. (2017) concluded that a specific type of plasma waves, known as electromagnetic ion cyclotron (EMIC) waves, were found to play a dominant role in scattering electrons. These waves, along others that may drive depletions in the outer belt, are further discussed in Section 3.2, and their effect on radiation belt electrons is thoroughly investigated in Chapters 7 and 8.

A second example, in this case a flux enhancement, is presented in Figure 3.2 (Reeves et al., 2013) which shows an intense relativistic electron acceleration event on 09 October 2012, also observed by the Van Allen Probes. A previous storm on 01 October had strongly depleted the outer belt, and the 2.5 MeV electron flux remained low and gradually decreased until early 09 October, when the flux suddenly rose. This is an exceptional event in that the flux sharply increased around three orders of magnitude in less than 12 hours. Reeves et al. (2013) used these measurements to clearly distinguish between two types of acceleration (radial-diffusive and local wave-particle), and concluded that this event was driven by local acceleration in the heart of the outer belt ($L \sim 4.2$). Both mechanisms are described in more detail in Section 3.3.

Both above-mentioned events illustrate the inconsistent response of the outer belt electrons to geomagnetic activity. For example, a statistical survey of 276 storms from 1989 to 2000 performed by Reeves et al. (2003) found that 53% resulted in an

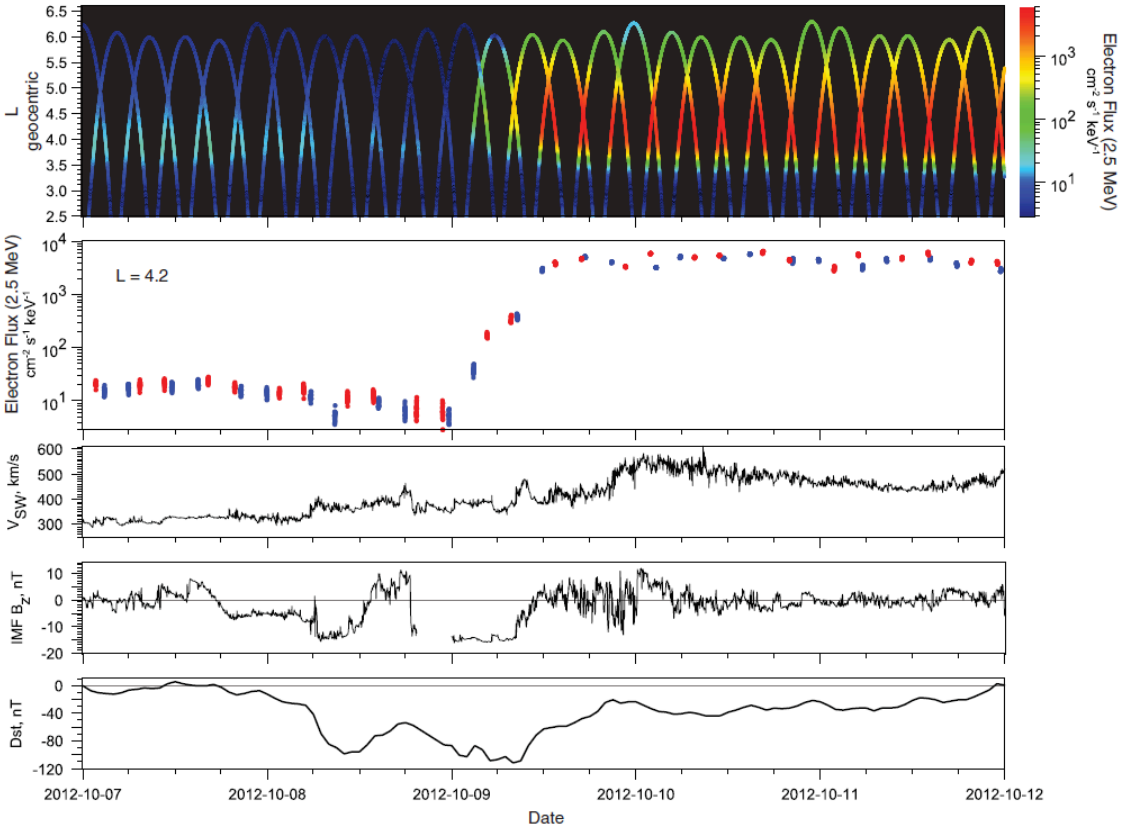

FIGURE 3.2: The top panel shows the flux of 2.5 MeV electrons measured by the Van Allen Probes between 07 October 2012 and 12 October 2012 as a function of L and time. The second graph shows the intensity of the electron outer belt at $L = 4.2$, and the bottom three panels depict the solar wind speed, the IMF north-south component, and the *Dst* index, respectively (Reeves et al., 2013).

increase of 1.8 to 3.5 MeV electron fluxes at GEO altitude, while 19% produced decreased fluxes, and 28% resulted in no change. More recently, Turner et al. (2015) investigated 52 storms throughout the Van Allen Probes mission, from September 2012 to February 2015, and found that relativistic electrons with $E \geq 1$ MeV were nearly equally likely to produce enhancements, depletions, or no-change events in the outer belt. The wide range of responses suggests that both acceleration and loss, caused by a violation of one or more of the adiabatic invariants, are capable of producing dramatic flux changes, are enhanced during different conditions, and ultimately compete to determine the final flux levels (Green et al., 2004). Therefore, in order to understand and predict electron flux variations, it is crucial to study the various mechanisms responsible for enhancements and losses and the balance between them.

3.2 Plasma Waves

Plasma is a dispersive medium which supports the propagation of electromagnetic waves, referred to as plasma waves. As presented in the previous chapter, plasma in the magnetosphere is not homogeneous, and varies widely in magnetic field strength, composition, temperature, and density. Such differences provide an environment in which a number of different plasma waves can exist. These waves can interact with the trapped electrons in the outer Van Allen belt, and alter their pitch

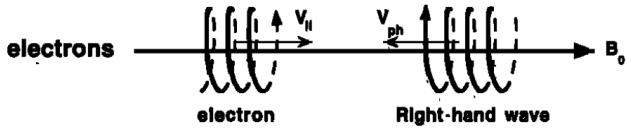

FIGURE 3.3: Normal cyclotron resonant interaction between an electron and a right-handed polarised wave (Tsurutani and Lakhina, 1997).

angle, energy, and drift path. In this section, the interaction between electromagnetic waves and particles in a plasma is discussed, and then, several different modes of plasma waves that exist in the magnetosphere are presented.

3.2.1 Wave-Particle Interactions

Wave-particle interactions play an essential role in space phenomena (Gary, 1992) and in shaping the plasma populations of the inner magnetosphere (Tsurutani and Lakhina, 1997). Resonant interactions allow for efficient energy transfer between a given particle and a wave, if both of them maintain the same phase relation for a sufficient period of time. In cyclotron resonance, the particle and the wave have the same angular frequency, i.e. $\omega = \Omega_\sigma$. The condition for cyclotron resonance between a given wave and a particle is (e.g. Tsurutani and Lakhina, 1997; Millan and Thorne, 2007):

$$\omega - k_{\parallel} v_{\parallel} = \frac{n\Omega_\sigma}{\gamma}, \quad n = 0, \pm 1, \pm 2, ... \tag{3.2}$$

where ω is the wave frequency, $k_{\parallel}$ and $v_{\parallel}$ are the components of the wave vector and particle velocity parallel to the ambient magnetic field, respectively, and Ω_σ is the gyrofrequency of the particle.

Whistler mode and EMIC waves propagate only at frequencies below the electron and the ion gyrofrequency, respectively. However, resonance is still possible if the wave frequency is Doppler-shifted up to a multiple of the gyrofrequency ($n \neq 0$) of the particle. As a result of the Doppler shift, resonance is met, and the particle observes the wave at its gyrofrequency or multiples of its gyrofrequency. Under these conditions, the particle will experience a constant component of the electric field that can accelerate or decelerate it.

Figure 3.3 shows an example of the normal cyclotron resonance, in which waves and particles move towards each other. In this case, for right-hand circularly polarised whistler mode waves propagating along the magnetic field, the wave frequency must be Doppler-shifted up for resonance with electrons, and thus the waves resonate travelling in the opposite direction. Conversely, under anomalous cyclotron resonance, particles must overtake an opposite polarised wave, in order for resonance to be met. An example of this interaction is the resonance between MeV electrons and left-handed polarised EMIC waves (Thorne and Kennel, 1971). Cyclotron resonance interactions can violate the first and second adiabatic invariants and lead to electron diffusion in energy and pitch angle. Both mechanisms are described in Sections 3.3.1.2 and 3.3.2.2, respectively.

In addition, bounce-drift resonance arises when ultra low frequency (ULF) waves interact with particles undergoing the drift motion with the same frequency. The resonance condition for the bounce-drift resonance is (e.g. Southwood, Dungey, and Etherington, 1969; Southwood and Kivelson, 1981):

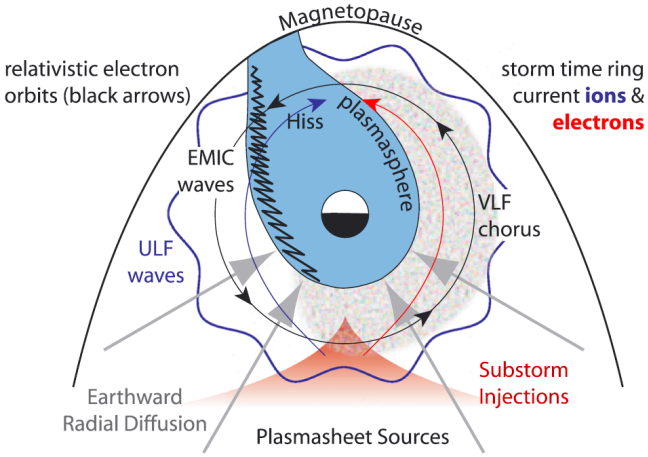

FIGURE 3.4: Schematic illustration of the spatial distribution of various magnetospheric waves and energetic particle populations in the equatorial inner magnetosphere (Li and Hudson, 2019).

$$\omega - m\omega_d = n\omega_b, \tag{3.3}$$

where m is the azimuthal wave number, ω_b is the bounce frequency, and ω_d is the azimuthal drift frequency. As plasmasheet electrons are transported inwards through the radial diffusion process (Fälthammar, 1965), energy is exchanged between electrons and ULF waves through the drift resonance. This mechanism of inward transport is further discussed in Section 3.3.1.1.

In the terrestrial magnetosphere, changes in the energetic electron population are controlled by interactions with various plasma waves. During magnetically active periods, intense waves are excited in the magnetosphere, which results in the violation of one or more of the adiabatic invariants (Schulz and Lanzerotti, 1974). The encounter between plasma waves and electrons in the outer radiation belt drifting around the Earth can lead to wave-particle interactions, resulting in electron acceleration or loss.

ULF waves can violate the third adiabatic invariant, leading to radial diffusion. Higher frequency kinetic waves, in the extremely low frequency (ELF) and very low frequency (VLF) range, which are excited by the injection of plasmasheet particles into the outer belt during increased convection, can violate the first two invariants, causing local acceleration and loss to the atmosphere due to pitch-angle scattering. Four of the most important plasma waves are illustrated in Figure 3.4 and are described in the next sections.

3.2.2 Ultra Low Frequency Waves (ULF)

ULF waves typically have frequencies in the order of a few mHz. Solar wind velocity shear (Claudepierre, Elkington, and Wiltberger, 2008) and pressure variations (Ukhorskiy et al., 2006; Claudepierre et al., 2009) at the magnetopause boundary excite ULF waves. The global distribution and variability of these waves can be monitored by space-borne and ground-based magnetometers.

Due to the frequency of ULF waves, resonant interactions with the drift period τ_d of electrons may occur, violating the third invariant while conserving the first and second invariants. Interaction with ULF waves along with violation of the third

invariant leads to radial diffusion, in which particles drift inwards or outwards. Inward radial diffusion (see Section 3.3.1.1) energises particles in the radiation belts during inward transport from sources at higher L in the plasmasheet. ULF wave radial diffusion can also redistribute new flux created by, for instance, local VLF chorus acceleration across L shells (e.g. Selesnick and Blake, 1997). Moreover, ULF waves can transport particles outwards through enhanced outward radial diffusion resulting in de-energisation and ultimately, loss to the magnetopause (e.g. Shprits et al., 2006c; Turner et al., 2012a).

3.2.3 Chorus Waves

Chorus emissions are discrete, coherent, intense whistler mode right-handed VLF waves that occur in the $\sim$ 100 Hz to tens of kHz frequency range below the local electron gyrofrequency (f_{ce}). Chorus is often observed in two frequency bands with a gap at $0.5f_{ce}$ (Tsurutani and Smith, 1974), separating the waves into lower-band ($0.1f_{ce} < f < 0.5f_{ce}$) and upper-band chorus ($0.5f_{ce} < f < f_{ce}$). These waves are characterised by bursts of short duration that rise or fall rapidly in frequency. Although they may last only a few milliseconds, they usually overlap and recur repeatedly for many hours (Santolík et al., 2003). Chorus waves are primarily observed in the low-density region outside of the plasmasphere (see Figure 3.4), and are strongest in the dawn sector (Meredith, Horne, and Anderson, 2001a).

Chorus waves are generated by cyclotron resonance with anisotropic electrons with energies from a few keV up to tens of keV, injected from the plasmasheet into the inner magnetosphere during storms and substorms (e.g. Hwang et al., 2007; Li et al., 2009). Nightside chorus is strongest inside $L = 8$ and is confined to latitudes below 15^{o}, as a result of Landau damping of oblique waves as they propagate from the equatorial source region towards higher latitudes (Bortnik, Thorne, and Meredith, 2007). In contrast, dayside chorus is observed over a broader range of latitudes, maximises in the outer magnetosphere ($L \sim 8$), and is less dependent on geomagnetic activity (Tsurutani and Smith, 1977).

Whistler mode chorus plays a significant role in radiation belt dynamics, by contributing both to acceleration and loss of electrons. Chorus waves provide an energy transfer mechanism from the substorm injected low-energy (few keV) electrons, to the trapped high energy radiation belt electrons by means of energy diffusion (Horne and Thorne, 2003). These emissions are thought to be responsible for the gradual flux build-up on a timescale of 1 to 2 days during the storm recovery phase (Horne et al., 2005b). In contrast, pitch-angle scattering during cyclotron resonance with chorus waves provides a mechanism for loss by collisions in the atmosphere (Hikishima et al., 2009; Lam et al., 2010). At lower electron energies, pitch-angle scattering by chorus is largely responsible for the diffuse aurora (Thorne et al., 2010) and the pulsating aurora (Nishimura et al., 2010).

3.2.4 Plasmaspheric Hiss

Hiss is a broadband, structureless, ELF whistler mode emission that occurs below f_{ce} in the frequency range from approximately 100 Hz to several kHz. These waves are primarily observed throughout the higher density regions associated with the Earth's plasmasphere and dayside plasmaspheric plumes (Thorne et al., 1973), with the strongest emissions between noon and dusk (Meredith et al., 2004). Hiss waves are nearly field-aligned close to the equator, but become more oblique as they propagate to higher latitudes (Ni et al., 2013a).

The ray tracing modelling (Bortnik, Thorne, and Meredith, 2008) showed that hiss may originate from bursts of short duration ($\sim$ 0.1 s) chorus emissions which are excited outside the plasmasphere and avoid Landau damping during propagation into the plasmasphere, and become trapped by the high density plasma. Within the plasmasphere, the discrete chorus emissions merge together to form hiss. Recent observational studies have found a correlation between the amplitude modulation of chorus and hiss on two Time History of Events and Macroscale Interactions during Substorms (THEMIS) spacecraft (Bortnik et al., 2009) and two Cluster spacecraft (Wang et al., 2011).

Inside the plasmasphere, hiss contributes to the loss of outer radiation belt electrons during the main and recovery phases of storms (Summers, Ni, and Meredith, 2007) and the quiet time decay of energetic electrons in the outer belt (Meredith et al., 2006). Moreover, pitch-angle scattering by plasmaspheric hiss is primarily responsible for the formation of the quiet time slot region (e.g. Lyons and Thorne, 1973; Meredith et al., 2007; Meredith et al., 2009).

Figure 3.5, taken from Bortnik, Thorne, and Meredith (2008), shows an observation of chorus and hiss waves performed by the Combined Release and Radiation Effects Satellite (CRRES). After 11 UT, during its inbound orbit, CRRES travelled from higher to lower L and entered the plasmasphere on the dayside. The frequency band of chorus followed the equatorial gyrofrequency and remained confined between 0.1 and 0.45 f_{ce}, with increasing frequency as the satellite moved to lower L. Chorus emissions were suddenly cut off at 14:40 UT, when CRRES entered the plasmasphere, and were replaced by plasmaspheric hiss, with a peak intensity near the outer boundary of the plasmasphere.

3.2.5 Electromagnetic Ion Cyclotron Waves (EMIC)

EMIC waves are left-handed polarised, lower-frequency waves (0.1 to 5 Hz) which propagate below the proton gyrofrequency. The EMIC source region is typically confined within $\sim 10^{o}$ of the geomagnetic equatorial plane. EMIC waves are excited by anisotropic 1 to 100 keV ring current ions injected into the inner magnetosphere during enhanced convection in the course of storms and substorms (e.g. Cornwall, Coroniti, and Thorne, 1970; Kozyra et al., 1984) or by increases in the solar wind dynamic pressure (e.g. Usanova et al., 2008). EMIC waves are most often enhanced in the high-density regions along the duskside plasmapause (Thorne and Horne, 1997; Jordanova et al., 1998) and within plasmaspheric plumes (Spasojević et al., 2003).

EMIC waves are observed in three bands below the proton, helium ion, and oxygen ion cyclotron frequency, the excited band being controlled by the ion composition, the anisotropy of the proton distribution (Kozyra et al., 1984), and the location with respect to the plasmapause (Fraser and Nguyen, 2001). Hydrogen band EMIC waves, which are observed between the proton and helium ion gyrofrequencies, are primarily found outside the plasmapause. Helium band EMIC waves, observed between the helium and oxygen ion gyrofrequencies, are found both inside and outside the plasmapause. Oxygen band EMIC waves, below the oxygen ion gyrofrequency, are seldom observed.

As mentioned in Section 3.2.1, in order to resonate with EMIC waves, electrons must overtake the wave and change the sense of polarisation in the electron reference frame, allowing for cyclotron resonance to occur (Tsurutani and Lakhina, 1997). As a consequence, EMIC waves mainly resonate with electrons above certain threshold energies. Thorne and Kennel (1971), Albert (2003), and Summers and Thorne

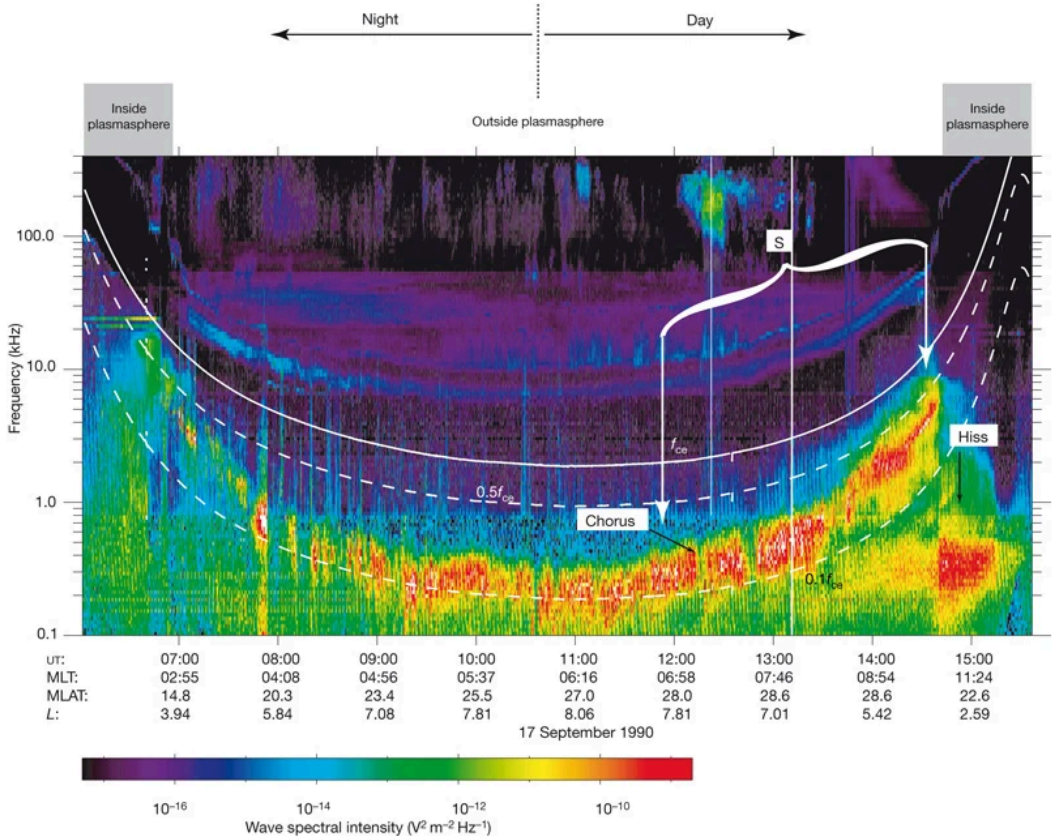

FIGURE 3.5: Wave spectral intensity for orbit 130 of the CRRES Plasma Wave Experiment. Plasmaspheric hiss is confined to the plasmasphere, and whistler mode chorus is observed outside the plasmapause (Bortnik, Thorne, and Meredith, 2008).

(2003) concluded that such threshold is $\sim$ 1 MeV. Furthermore, EMIC waves are only effective at scattering electrons with pitch angles below around 45° (e.g. Kersten et al., 2014; Usanova et al., 2014; Drozdov et al., 2020), ultimately resulting in loss to the atmosphere and the narrowing of pitch-angle distributions.

An example of an EMIC wave event observed by the Van Allen Probe B is shown in Figure 3.6. Helium band and hydrogen band EMIC wave power is plotted as a function of time and frequency, with the interval 19:20 UT to 19:40 UT exhibiting the most intense measured EMIC waves, as marked by the vertical dashed-dotted purple lines.

3.3 Variability of Radiation Belt Electrons

As mentioned in Section 2.3.3.6, the Earth's outer radiation belt is highly dynamic, and electron fluxes can vary on timescales of several hours to a few days, particularly during and after geomagnetic storms. Both acceleration and loss are capable of producing dramatic changes and compete to determine the final flux levels. This section outlines various source and loss processes that have been identified as instrumental in driving the outer belt variability.

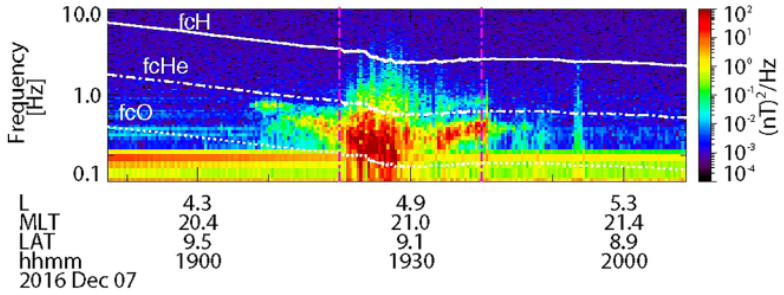

FIGURE 3.6: Helium band and hydrogen band EMIC wave power recorded by Van Allen Probe B on 07 December 2016. Proton, helium, and oxigen ion gyrofrequencies are indicated by solid, dashed-dotted, and dotted white curves, respectively (Pinto et al., 2020).

3.3.1 Source Mechanisms

Since the discovery of the Van Allen belts, electron flux enhancements have often been observed during geomagnetic storms, and researchers have sought to identify the mechanisms by which electrons are accelerated from energies of a few keV to several MeV. Two leading theories have emerged to explain this: transport and acceleration of electrons from a source population at and beyond GEO (inward radial transport), and in-situ acceleration by wave-particle interactions in the heart of the outer belt (local acceleration).

3.3.1.1 Inward Radial Transport

Radial transport moves a source population located at large radial distances inwards, and violates the third invariant, while conserving the first two. As electrons move inwards into regions of stronger magnetic field, they are energised via betatron acceleration (Schulz and Lanzerotti, 1974). Radial transport may act diffusively driven by ULF waves, or non-diffusively, for instance during strong interplanetary shock compressions.

Up until the mid-1990s, the proximate source of the radiation belts was considered to be the electrons in the Earth's plasmasheet, and inward radial diffusion was established as the leading mechanism for the outer belt electrons (Fälthammar, 1965; Schulz and Lanzerotti, 1974). According to the radial diffusion model, electrons are transported to within 2.5 R_E during storms from a reservoir of particles beyond GEO. Electrons are diffused across the magnetic field by large scale magnetic and electric field fluctuations in the outer belt at frequencies that are resonant with the electron drift frequencies of a few mHz around the Earth. This process is faster when ULF waves at a few mHz are enhanced (e.g. Elkington, Hudson, and Chan, 1999; Liu, Rostoker, and Baker, 1999; Elkington, 2006; Ozeke et al., 2012; Su et al., 2015).

Shprits et al. (2005) employed a 1D radial diffusion model with constant boundary conditions based on averaged fluxes at $L = 7$, and were able to simulate features of the variability of the outer belt and predict fluxes within one order of magnitude for most of the storms during their study. However, their model failed to reproduce the gradual buildup of fluxes observed during the recovery phases of storms, concluding that local acceleration was required to accurately reproduce the dynamics of the electron fluxes. Liu et al. (2018) and Ozeke et al. (2019) also reproduced individual storm events by means of a 1D radial diffusion model and a dynamic outer boundary, showing relativistic electron flux enhancements in agreement with observations in magnitude and timescale.

Injections of electrons in the outer radiation belt can also occur due to the magnetospheric impacts from interplanetary shocks. As a result of the dayside magnetopause compression due to the shock arrival, an azimuthal electric field is launched within the magnetosphere. The impulse propagates tailward along both flanks of the magnetosphere, accelerating those electrons in drift resonance with the electric field impulse. This electric field transports them radially inward and accelerates them while conserving their first adiabatic invariant (Li et al., 1993). Based on observations by the CRRES satellite, Blake et al. (1992) reported a prompt acceleration by a large CME-interplanetary shock on 24 March 1991, injecting multi-MeV electrons into $L < 3$ and producing a new radiation belt in the normally devoid slot region. Baker et al. (2004) also studied the sudden formation of a new belt within the slot region during the Halloween storm of 2003. After being injected to such low L values, the multi-MeV electrons remained for over a year. Thus, shock injections typically associated with severe geomagnetic storms are an acceleration mechanism that can produce rapid and sudden enhancements of the outer radiation belt.

3.3.1.2 Local Acceleration

Challenges to the inward radial diffusion model began to arise in the 1990s, when a growing fleet of satellites provided multipoint measurements with temporal and spatial resolution, revealing complex structures and rapid dynamics that were difficult to explain with radial diffusion theory. In January 1997, a strong geomagnetic storm triggered a dramatic intensification of electron fluxes at energies up to several MeV (e.g. Reeves et al., 1998a; Reeves et al., 1998b; Selesnick and Blake, 1998). Reeves et al. (1998a) compared the dynamics at GEO and in the heart of the outer belt, and found that the behaviour of the 2 MeV electrons was startlingly different. The intensification of relativistic electron fluxes over two orders of magnitude first occurred in the heart of the belts in less than 12 hours, whereas the buildup of fluxes at GEO was observed later and more gradually. These observations suggested an energisation process taking place locally in the heart of the outer belt.

In the local acceleration mechanism, electrons are energised at a particular L by violating their first two invariants via cyclotron resonant interactions with VLF waves. Summers, Thorne, and Xiao (1998) showed that this process is associated with waves at frequencies of a few kHz, primarily whistler mode chorus, which can provide a viable mechanism to account for the stochastic acceleration of the $\sim$ 100 keV population up to relativistic energies of a few MeV (Horne and Thorne, 1998). Further support for the local acceleration theory was presented by Horne et al. (2005a), who showed that the timescale to accelerate electrons by chorus and increase the flux at 1 MeV by an order of magnitude was approximately 1 day, in agreement with satellite observations during the recovery phase of storms. Horne et al. (2005b) studied the Halloween storm of 2003, a rare event when the outer radiation belt was depleted and later reformed closer to the Earth, and found that wave acceleration by chorus was more than sufficient to explain the new belt, whereas inward radial diffusion alone could not explain the increase in electron fluxes (Shprits et al., 2006a). Later studies performed 2D simulations of specific storm events, and demonstrated that electron acceleration driven by chorus waves deep within the outer belt was able to reconstruct the flux enhancements observed by the Van Allen Probes (e.g. Li, Shprits, and Thorne, 2007; Thorne et al., 2013; Li et al., 2014).

The current paradigm for understanding the local acceleration of relativistic electrons in the outer belt is presented in Figure 3.7, taken from Jaynes et al. (2015). This scenario involves both a source population of several to tens of keV electrons that

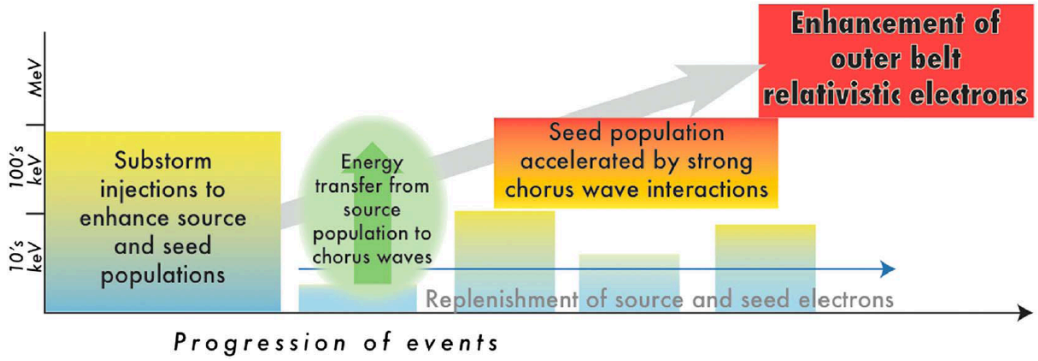

FIGURE 3.7: Schematic showing the conceptual scenario for strong enhancements of $E > 1$ MeV outer belt electrons (Jaynes et al., 2015).

generates chorus waves, and a seed population of tens to hundreds of keV electrons that can be accelerated to relativistic energies. Such an event normally starts with a strong solar wind forcing event and a southward turning of the IMF, followed by substantial energy loading into the magnetotail, which triggers the onset of a magnetospheric substorm after $\sim$ 1 h (see Section 2.3.3.8). The onset is accompanied by the injection of low to medium energy electrons from the plasmasheet into the inner magnetosphere (e.g. Baker et al., 1996; Friedel et al., 2001; Ganushkina et al., 2014; Kronberg et al., 2017). The lower-energy (1 to 30 keV) electrons constitute the source population, which have anisotropic angular distributions that transfer free energy to lower-band chorus waves (Li et al., 2010; Thorne et al., 2013). These waves then interact resonantly with the substorm injected medium energy electrons (30 to 300 keV), i.e. the seed population. Chorus waves can very efficiently accelerate such electrons to multi-MeV energies through resonant interactions. The seed electrons can be enhanced in energy on time scales of minutes to hours (e.g. Horne et al., 2005a; Thorne et al., 2013; Foster et al., 2014).

Meredith et al. (2003a) performed a survey of geomagnetically disturbed periods from the CRRES satellite, and found that the most significant relativistic flux enhancements occurred in connection with prolonged substorm activity. These events were associated with increased seed electron flux and enhanced lower-band chorus wave power.

3.3.2 Loss Mechanisms

Electron dropouts in the radiation belts can be produced by two categories of loss processes: adiabatic or reversible effects, and nonadiabatic or irreversible changes. The *Dst* effect is an example of the former, whereas local precipitation, magnetopause shadowing, and outward radial diffusion correspond to the latter category and represent true loss to the system.

3.3.2.1 Dst Effect

Adiabatic variations occur when the magnetic field changes slowly compared to the timescale associated with the three adiabatic invariants, thus resulting in a reversible loss of electrons (Dessler and Karplus, 1961). During the main phase of a geomagnetic storm, when the *Dst* is significantly negative, the intensity of the ring current is enhanced, and the strength of the geomagnetic field decreases. In order to conserve

their third adiabatic invariant, the electrons move outward, which results in an expansion of their drift shells. By moving further away from the Earth, the electrons are now in a lower magnetic field, and therefore lose some of their kinetic energy in order to conserve their first invariant. In general, the number of radiation belt particles decreases exponentially with increasing energy, thus for a stationary observer measuring a fixed energy range, there would appear to be a dropout of electrons at that energy. During the recovery phase of the storm, the ring current decreases back to its pre-storm level, the magnetic field increases, the electrons are accelerated, and the expanded drift shells contract. As a result, the system returns to its initial, pre-storm state. Since this phenomenon takes place during geomagnetic storms, it has been referred to as the *Dst* effect (Kim and Chan, 1997).

However, for many storms electron fluxes do not return to their original pre-storm values, indicating that true non-reversible loss occurs during storms (e.g. McAdams and Reeves, 2001; Onsager et al., 2002; Reeves et al., 2003; Green et al., 2004; Boynton, Mourenas, and Balikhin, 2016). In such cases, the dropout is a result of several different nonadiabatic processes that remove the electrons permanently. Two plausible theories to explain the non-reversible dropouts are atmospheric precipitation due to wave-induced pitch-angle scattering, and magnetopause shadowing combined with outward radial diffusion. These non-adiabatic mechanisms are presented in the next sections.

3.3.2.2 Local Precipitation

Pitch-angle diffusion and scattering of radiation belt electrons into the atmosphere is driven by wave-particle interactions with some of the plasma waves presented in Section 3.2. Three wave modes are primarily responsible for the majority of particle losses in the inner magnetosphere by means of pitch-angle scattering: hiss, chorus, and EMIC waves. The diffusion coefficients, and hence the effective loss rates, depend on electron pitch angle, energy, and location.

As mentioned in Section 2.1.2, as electrons drift around the Earth, they bounce back and forth between their mirror points in the northern and southern hemispheres. Using equation 2.14, for particles with equatorial pitch angles less than $\alpha_{LC} = \sin^{-1}\sqrt{B_{\mathrm{eq}}/B_a}$, where B_a is the field intensity at the top of the atmosphere ($\sim$ 100 km), the mirror point lies deep within the atmosphere. Electrons with $\alpha_{\mathrm{eq}} < \alpha_{LC}$ therefore strike the atmosphere during each bounce, where the density of neutral particles is large enough for loss due to collisions, and are rapidly removed from the trapping region. The quantity α_{LC} is known as the bounce loss cone angle.

The existence of the SAA (Section 2.3.2) introduces a longitudinal dependence on the mirror altitude of a drifting electron, such that the altitude is lowest over the anomaly region. Electrons that are outside of the bounce loss cone away from the SAA may find themselves inside the loss cone over the SAA. For a given drift shell, the drift loss cone is the smallest equatorial pitch angle that allows an electron to entirely drift around the Earth without being lost to the atmosphere. The interaction between waves and electrons alters the particle's pitch angle, by making it sufficiently aligned to be into the bounce or drift loss cone, driving diffusion and enhancing atmospheric losses.

Inside the plasmasphere, resonant interactions with plasmaspheric hiss dominate the pitch-angle scattering of radiation belt electrons. Li, Shprits, and Thorne (2007) showed that pitch-angle diffusion coefficients for hiss waves are higher for the lower-energy electrons. Hiss was found to be more effective in scattering few hundred keV electrons at $L = 4.5$, consistent with the results of Meredith et al. (2006)

for scattering in the plasmasphere. Shprits et al. (2008) found decay times of a few days at 500 keV, $\sim$ 10 days at 1 MeV, and $\sim$ 40 days at 2 MeV.

Near the duskside plasmapause, the presence of EMIC waves significantly decreases the electron lifetimes. Simulations of the combined scattering by hiss and EMIC waves performed by Shprits et al. (2008) showed that, while scattering by only hiss is weaker at high energy and the lifetime due to hiss alone gets longer, this trend is reversed by the presence of EMIC waves. However, hiss still plays an important role at MeV energies in the combined scattering by transporting electrons from higher pitch angles towards the loss cone.

One of the dominant loss mechanisms outside the plasmasphere is pitch-angle scattering by chorus waves. Shprits et al. (2006b) performed numerical experiments of the sensitivity of scattering rates to the latitudinal distribution of waves, and found that, when chorus emissions are confined to within 15^o of the magnetic equator, they produce no scattering near the edge of the loss cone, and therefore electron losses at MeV energies. In contrast, when chorus waves with the same spectral properties extend to higher latitudes, very fast losses of relativistic electrons, on the scale of 1 day, are observed. Dayside chorus, which extends to latitudes up to 30^o and possibly beyond (Meredith, Horne, and Anderson, 2001b; Meredith et al., 2003b), produce a significant loss of MeV electrons, providing lifetimes on the timescale of a few days at MeV energies (Shprits et al., 2008). However, on the nightside, MeV electrons are not able to diffuse into the loss cone.

EMIC waves are only effective at scattering particles with lower pitch angles, leaving those with higher pitch angles essentially unaffected. Previous studies have shown that additional contemporaneous scattering by hiss in plumes or by chorus (e.g. Li, Shprits, and Thorne, 2007; Albert and Shprits, 2009; Shprits, Chen, and Thorne, 2009; Shprits et al., 2013b; Mourenas et al., 2016; Shprits et al., 2016; Zhang et al., 2017; Pinto et al., 2020) is needed in order for EMIC waves to significantly deplete the entire pitch-angle distribution, and to reduce the lifetimes of ultrarelativistic $E > 2$ MeV electrons, while EMIC or chorus waves alone cannot produce such fast and strong dropouts. EMIC waves drive loss at small pitch angles but also create gradients in the pitch-angle distribution, assisting chorus waves in scattering relativistic electrons near 90^o pitch angle toward the loss cone.

3.3.2.3 Magnetopause Shadowing and Outward Radial Diffusion

Loss across the magnetopause, called magnetopause shadowing, is another non-adiabatic process. This term describes the scenario in which the magnetopause moves inward due to abrupt increases in solar wind dynamic pressure, resulting in the depletion of electrons on open drift paths that were previously closed (e.g. Kim et al., 2008; Ohtani et al., 2009; Morley et al., 2010; Turner et al., 2012a). Once the magnetopause subsides to its pre-compression, quiet time shape, there is a steep radial gradient at the edge of the outer belt which, in turn, drives outward radial diffusion by enhanced ULF waves. This mechanism transports electrons away from the Earth into the region of weaker magnetic field, decelerates particles, and propagates progressively further electron loss to lower-L values (Shprits et al., 2006c). In this way, magnetopause shadowing coupled with outward radial diffusion can contribute to the observed flux decrease deep in the heart of the radiation belts.

As described in Section 2.2.2, due to the pitch-angle dependence on the electron's drift path, particles with different initial pitch angles follow different drift trajectories, and therefore, different probabilities of encountering the dayside magnetopause on the drifts around the Earth. Consider two electrons initially located on a magnetic

field line around midnight, one with a more perpendicular pitch angle, and another with a more parallel initial pitch angle. The near perpendicular electron will drift to a larger radial distance at noon than the electron with more parallel propagation, and therefore, is more likely to encounter the dayside magnetopause and be lost from the trapping region. When a spacecraft measures the pitch-angle distributions near the edge of the outer belt, it is common to observe a minimum centred around 90^{o}.

An important concept for radiation belt particles is the last closed drift shell (LCDS), as it defines the outer boundary of stable trapping in the geomagnetic field. The LCDS represents the outermost drift path of a particle which entirely encircles the Earth without encountering the magnetopause. Since the drift path of a particle depends on its pitch angle, the location of the LCDS is also pitch-angle dependent. Rapid radial loss during dropouts is well correlated with the LCDS location under strong magnetopause compressions (Albert et al., 2018; Olifer et al., 2018).

Evidence in favour of either loss to the atmosphere due to wave-particle interactions or loss due to magnetopause shadowing and enhanced outward radial transport has been provided by numerous observational (e.g. Green et al., 2004; Matsumura et al., 2011; Turner et al., 2012a; Boynton, Mourenas, and Balikhin, 2016; Boynton, Mourenas, and Balikhin, 2017; Shprits et al., 2017) and modelling efforts (e.g. Shprits et al., 2006c; Su et al., 2011; Yu, Koller, and Morley, 2013; Mann et al., 2016). Other studies have argued that losses during dropouts could be explained by a combination of different loss mechanisms operating at distinct L ranges during dropouts. For instance, Bortnik et al. (2006) suggested that loss at $L > 5$ was dominated by magnetopause shadowing and outward radial diffusion, whereas at $L < 5$ it was dominated by pitch-angle scattering driven by EMIC waves. Turner et al. (2014b) studied another dropout event and concluded that both loss mechanisms operated, with a boundary at $L^* \sim 4$. Similarly, on the basis of three distinct radiation belt dropouts, Xiang et al. (2017) concluded that magnetopause shadowing can deplete electrons at $L^* > 4$, while EMIC waves can efficiently scatter electrons at $L^* < 4$. These two loss processes, pitch-angle scattering due to EMIC waves, and magnetopause shadowing coupled with outward radial diffusion, are the main topics of research of Chapters 7 and 8, where their relative contribution to radiation belt dropouts is assessed with a novel approach based on data assimilation (introduced in detail in Chapter 6).

3.4 Phase Space Density (PSD)

As mentioned in the introduction of this chapter, a vast number of electrons reside in the outer radiation belt, and particles are typically measured in terms of fluxes, a non-adiabatically conserved quantity, as a function of spatial location, energy, and pitch angle. Furthermore, as presented in Section 3.3, the dynamics of the outer belt is complicated by the fact that some of the variations are adiabatic, whereas others are non-adiabatic. However, by inferring phase space density (PSD) as a function of the three adiabatic invariants μ, K or J, and L^*, adiabatic and non-adiabatic changes can be separated. Therefore, the conversion of flux to PSD allows us to distinguish non-adiabatic electron acceleration and loss from purely adiabatic processes (e.g. the *Dst* effect), and to track the temporal evolution related to the non-reversible violation of the adiabatic invariants.

3.4.1 Definition of PSD

Phase space is a six-dimensional space composed of the three orthogonal spatial coordinates $\mathbf{r} = (x, y, z)$ and the three conjugate momenta, $\mathbf{p}$. The density of particles in phase space, i.e. PSD, is described by Liouville's theorem, which states that the PSD along particle trajectories through any point in phase space is constant. This theorem applies even when particles change momentum as well as position.

PSD is directly related to observable quantities such as particle flux via the following relationship (Walt, 1994):

$$f(\mathbf{r}, \mathbf{p}) = \frac{j(\alpha_{\text{eq}}, E)}{p^2}, \tag{3.4}$$

where $f(\mathbf{r}, \mathbf{p})$ is PSD, and $j(\alpha_{\text{eq}}, E)$ is the particle flux at equatorial pitch angle α_{eq} and energy E.

3.4.2 Evolution of PSD Profiles

Calculating the PSD vs L^* profile provides a diagnostic tool to unambiguously identify between various mechanisms responsible for radiation belt enhancements and depletions. For instance, Green and Kivelson (2004), Chen, Reeves, and Friedel (2007), and Reeves et al. (2013) analysed the time evolution of PSD radial profiles (i.e. PSD(L^*) at fixed μ and K) to distinguish radial diffusion from local acceleration, whereas Aseev et al. (2017), Shprits et al. (2017), and Xiang et al. (2017) applied the same general principle to differentiate between the mechanisms of radiation belt dropouts.

3.4.2.1 Source Mechanisms

Radial diffusion moves electrons in L^*, while conserving the invariants μ and K. Since it is a stochastic process, diffusion moves electrons from regions of higher PSD to lower PSD. Increased radial diffusion from a source population at high L^* can enhance the PSD at low L^*, and the radial gradients will exhibit a monotonic increase with increasing L^*. In contrast, local acceleration energises electrons and produces increases in PSD over a limited L^* range, which may lead to a growing, localised peak in the PSD radial profile with negative gradients at higher L^*.

Both acceleration mechanisms are summarised in Figure 3.8, which provide the telltale signatures of the source location of outer radiation belt electrons. Electrons with a source in the plasmasheet have a maximum in the PSD profile at high radial distances (i.e. the plasmasheet itself), while electrons that are locally energised within the heart of the outer belt have peaked radial profiles, and the peak is collocated with the waves driving the acceleration, such as chorus emissions. Turner et al. (2012b) studied both processes by employing THEMIS observations of electron PSD for fixed invariants (Figure 3.9), as the spacecraft moved into the near Earth plasmasheet. Positive radial gradients beyond GEO for electrons with energies between 80 and 300 keV in the heart of the outer belt were indicative of a source in the plasmasheet, whereas negative gradients beyond GEO and localised peaked profiles for relativistic electrons suggested a source within the heart of the outer belt, in the inner magnetosphere.

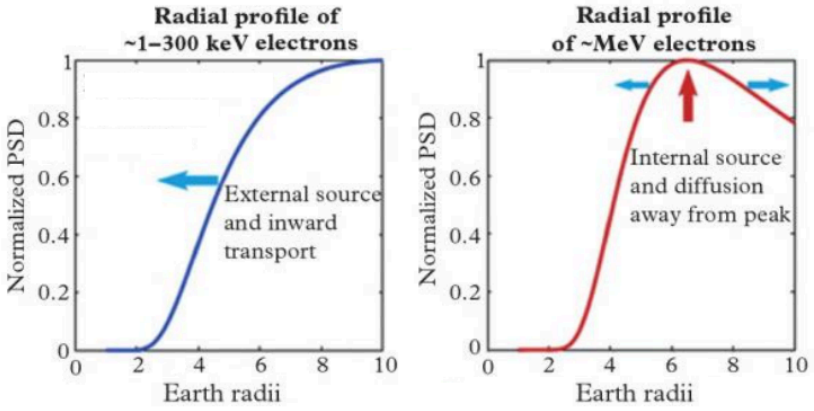

FIGURE 3.8: Schematics showing the PSD radial distributions for electron acceleration in the outer radiation belt. The lower-energy electrons have a source in the near-Earth plasmasheet, whereas the relativistic electrons have a local source in the heart of the outer belt. Adapted from Turner and Angelopoulos (2016).

3.4.2.2 Loss Mechanisms

The time evolution of PSD radial profiles can also be used to distinguish between loss processes. Figure 3.10, from Shprits et al. (2017), illustrates three potential scenarios of particle loss in the outer belt, in the absence of acceleration. The first case (Figure 3.10a) corresponds to particles that are resonantly scattered by whistler mode waves and are gradually lost to the atmosphere. As mentioned in Section 3.3.2.2, scattering rates by plasmaspheric hiss range from a few days at 500 keV up to several weeks for multi-MeV energies. Chorus wave-induced loss is on the scale of a few days at MeV energies. In this scenario, as the radial diffusion rates will likely dominate the loss rates, the ensuing radial profile of PSD is monotonic.

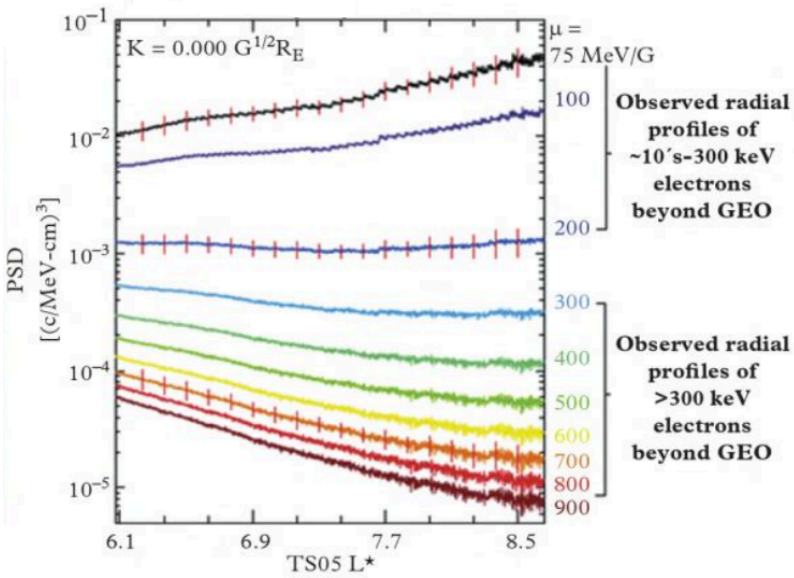

FIGURE 3.9: Profiles of THEMIS observations of PSD versus L^* for a broad range of the first invariant μ as the spacecraft moved beyond GEO into the plasmasheet. Adapted from Turner and Angelopoulos (2016).

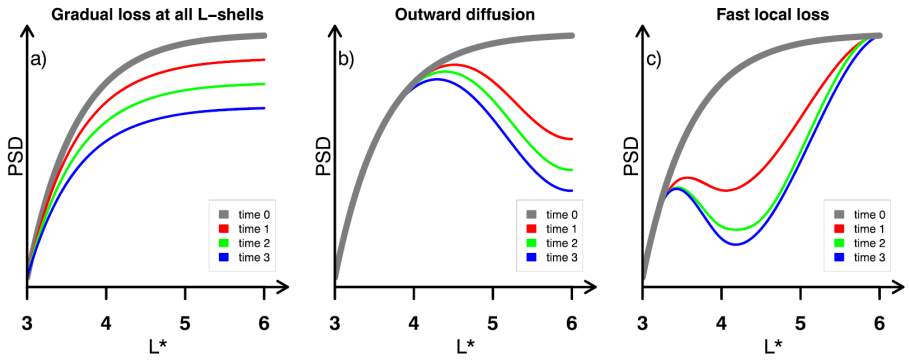

FIGURE 3.10: Schematics showing three scenarios for the PSD evolution when electrons are lost from the radiation belts (Shprits et al., 2017).

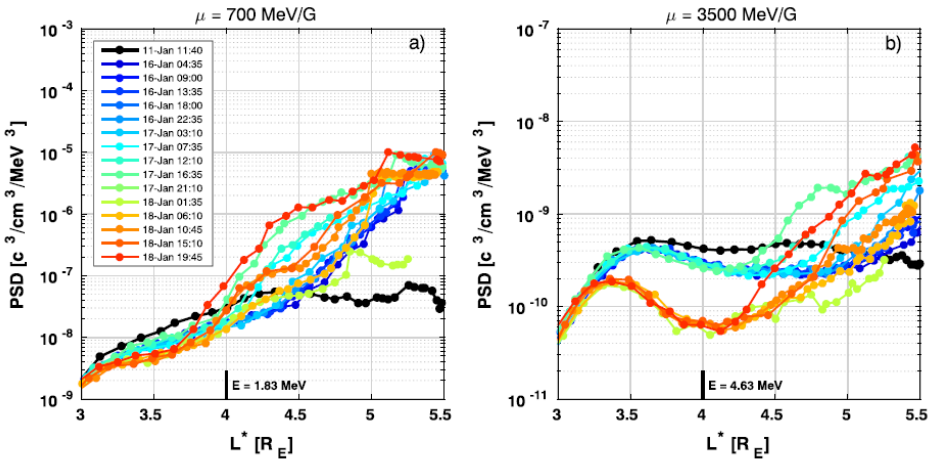

FIGURE 3.11: Profiles of PSD for (a) relativistic ($\mu = 700$ MeV/G) and (b) ultrarelativistic ($\mu = 3500$ MeV/G) electrons and $K = 0.1$ $G^{0.5}R_E$ measured by the Van Allen Probes. Adapted from Shprits et al. (2017).

Loss to the magnetopause and the subsequent outward radial diffusion is presented in Figure 3.10b. The arrival of high-pressure solar wind moves the magnetopause inward, creating sharp negative gradients in PSD at higher L^*. Such negative gradients from the initial loss and enhanced ULF wave activity drive further loss to the outer boundary via rapid outward radial diffusion. This process results in further irreversible losses throughout much of the outer belt, because electrons lose energy as they move outwards. The third scenario (Figure 3.10c) describes a localised, fast loss with deepening minima, e.g. driven by EMIC waves, which can induce loss rates on the scale of hours, as presented in Section 3.3.2.2.

An example of the evolution of PSD radial profiles during the 17 January 2013 storm, as observed by the Van Allen Probes, and corresponding to loss induced by EMIC wave scattering is presented in Figure 3.11. Panel (a) corresponds to $\mu = 700$ MeV/G (1.8 MeV at $L^* = 4$ using a dipole approximation). At such relativistic energies, the profile is mainly monotonic. In contrast, in panel (b), for $\mu = 3500$ MeV/G (4.6 MeV at $L^* = 4$), a local minimum is clearly formed and is subsequently deepened, indicating the presence of a local and very fast loss mechanism at ultrarelativistic energies. The inspection of the evolution of such profiles helps to pinpoint and visualise the location where the loss process is more efficient.

Chapter 4

Modelling the Earth's Electron Radiation Belts

The evolution of relativistic electrons in the radiation belts, previously introduced in Chapter 3, can be modelled by a diffusion equation. This chapter starts by introducing the modified Fokker-Planck equation often used in radiation belt modelling, in terms of radial distance, energy, and equatorial pitch angle, and with diffusion coefficients calculated from wave-particle resonant interactions. Then, a model known as the Versatile Electron Radiation Belt (VERB) code used to numerically solve the above-mentioned equation is presented, and the calculation procedure is described. Finally, the model setup, the diffusion rates, and the initial and boundary conditions used in the current study are enumerated.

4.1 Diffusion and the Fokker-Planck Equation

As mentioned in Chapter 2, electrons undergo three types of periodic motion in the radiation belts: gyration about field lines, bounce between their mirror points, and gradient-curvature drift around the Earth. For each particular type of motion, we can define an adiabatic invariant, which is constant as long as the parameters of the system vary on time scales longer than the corresponding motion period. The adiabatic invariants can be interpreted geometrically as the area covered by the trajectory of the particle in phase space. If the parameters of motion change slowly compared to the period of the motion, the area covered by the trajectory in phase space remains relatively constant (Landau and Lifshits, 1973).

The Fokker-Planck diffusion equation for the evolution of the phase-averaged PSD f of the relativistic electrons may be written in terms of the adiabatic invariants as follows (Schulz and Lanzerotti, 1974; Walt, 1994):

$$\frac{\partial f}{\partial t} = \sum_{i,j=1}^{3} \frac{\partial}{\partial J_i} D_{ij} \frac{\partial f}{\partial J_j}, \tag{4.1}$$

where J_1, J_2, and J_3 are the first, second, and third adiabatic invariants (μ, J, and Φ), respectively, and D_{ij} are diffusion coefficients, also known as scattering rates.

Diffusion is the result of violation of the adiabatic invariants. Only when one or more of the particle's invariants is altered, the particle can be said to diffuse. The first and second adiabatic invariants are violated by ELF/VLF waves, while the third invariant, by ULF waves. Due to the difference in time scales associated with these waves, the cyclotron frequency and the drift frequency interactions are considered to be uncoupled, and terms involving D_{13} and D_{23} are usually omitted (Albert, Meredith, and Horne, 2009):

$$\frac{\partial f}{\partial t} = \frac{\partial f}{\partial J_1}\left(D_{11}\frac{\partial f}{\partial J_1} + D_{12}\frac{\partial f}{\partial J_2}\right) + \frac{\partial f}{\partial J_2}\left(D_{12}\frac{\partial f}{\partial J_1} + D_{22}\frac{\partial f}{\partial J_2}\right) + \frac{\partial}{\partial J_3}D_{33}\frac{\partial f}{\partial J_3}. \quad (4.2)$$

The dominant approach for evaluating interactions between the radiation belt electrons and higher-frequency waves is quasilinear theory, where the effects of waves on particles are treated as diffusion (Schulz and Lanzerotti, 1974). In this framework, the waves are assumed to be of small amplitude and to have broadband structures, and the wave intensities are averaged over space and time. Diffusion coefficients account for the effects of waves on particles, and the evolution of electron PSD can be calculated by numerically solving the bounce and Magnetic Local Time (MLT)-averaged Fokker-Planck equation (Shprits et al., 2008; Subbotin and Shprits, 2009):

$$\begin{aligned}\frac{\partial f}{\partial t} &= L^{*2}\frac{\partial}{\partial L^*}\bigg|_{\mu,J}\left(\frac{1}{L^{*2}}D_{L^*L^*}\frac{\partial f}{\partial L^*}\bigg|_{\mu,J}\right) \\ &+ \frac{1}{p^2}\frac{\partial f}{\partial p}\bigg|_{\alpha_{\rm eq},L^*} p^2\left(D_{pp}\frac{\partial f}{\partial p}\bigg|_{\alpha_{\rm eq},L^*} + D_{p\alpha_{\rm eq}}\frac{\partial f}{\partial \alpha_{\rm eq}}\bigg|_{p,L^*}\right) \\ &+ \frac{1}{T(\alpha_{\rm eq})\sin(2\alpha_{\rm eq})}\frac{\partial}{\partial \alpha_{\rm eq}}\bigg|_{p,L^*} T(\alpha_{\rm eq})\sin(2\alpha_{\rm eq})\left(D_{\alpha_{\rm eq}\alpha_{\rm eq}}\frac{\partial f}{\partial \alpha_{\rm eq}}\bigg|_{p,L^*} + D_{\alpha_{\rm eq}p}\frac{\partial f}{\partial p}\bigg|_{\alpha_{\rm eq},L^*}\right) \\ &- \frac{f}{\tau}, \end{aligned} \quad (4.3)$$

which includes radial, energy, pitch-angle, and mixed pitch angle-energy diffusion. $D_{L^*L^*}$ is the drift and MLT-averaged radial diffusion coefficient, and D_{pp}, $D_{\alpha_{\rm eq}\alpha_{\rm eq}}$, and $D_{\alpha_{\rm eq}p}(\equiv D_{p\alpha_{\rm eq}})$ are the bounce and MLT-averaged energy, pitch-angle, and mixed pitch angle-energy diffusion coefficients, respectively, due to resonant wave-particle interactions. $T(\alpha_{\rm eq})$ is a function related to the particle's bounce motion, and in a dipolar field can be approximately given by (Lenchek, Singer, and Wentworth, 1961; Schulz and Lanzerotti, 1974):

$$T(\alpha_{\rm eq}) = 1.3802 - 0.3198(\sin\alpha_{\rm eq} + \sin^{0.5}\alpha_{\rm eq}). \quad (4.4)$$

The parameter τ represents losses due to the loss cone, where τ is the electron lifetime, which is assumed to be infinite outside the loss cone and equal to a quarter of the electron bounce time inside the loss cone.

4.2 The Versatile Electron Radiation Belt (VERB) Model

The first solution of the three-dimensional (3D) Fokker-Planck equation was performed using the Salammbô code (Beutier and Boscher, 1995; Bourdarie et al., 1996; Bourdarie et al., 1997). This model included radial diffusion by electric and magnetic field fluctuations, cosmic ray albedo decay, pitch-angle scattering by plasmaspheric hiss, and Coulomb collisions. Later, Varotsou et al. (2005) and Horne et al. (2005a) incorporated diffusion driven by chorus waves into the Salammbô code.

Shprits et al. (2008) and Subbotin and Shprits (2009) presented the 3D Versatile Electron Radiation Belt (VERB-3D) code, developed on the basis of the radial diffusion code (Shprits and Thorne, 2004) and the 2D code for pitch-angle and energy

diffusion (Shprits et al., 2006a). Shprits, Subbotin, and Ni (2009) performed simulations of idealised storms with the VERB-3D model using diffusion coefficients due to ULF waves, chorus, plasmaspheric hiss, and EMIC waves; and Subbotin, Shprits, and Ni (2010) later incorporated mixed pitch angle-energy diffusion into the model. In this thesis, the VERB-3D code is used to solve the modified Fokker-Planck equation and to model the radiation belt region. The next sections describe the calculation procedure, the diffusion coefficients used for the solution of equation 4.3, and the initial and boundary conditions employed in this study.

4.2.1 Numerical Solution

For the solution of equation 4.3 a finite differences approach with an implicit numerical scheme is employed (Subbotin and Shprits, 2009; Subbotin, Shprits, and Ni, 2010). The size of the computational grid used in this study is $29 \times 101 \times 91$ points along radial, energy, and pitch-angle dimension, respectively. Radial grid points are distributed uniformly, whereas energy and pitch-angle grid points are distributed logarithmically. The L^* grid is set from 1 R_E to 6.6 R_E. The energy grid is defined by a minimum of 0.01 MeV and a maximum of 10 MeV at the outer radial boundary. The pitch-angle grid extends from 0.3^o to 89.7^o. Furthermore, an operator-splitting method is used, in which equation 4.3 is divided between radial and local (energy, pitch-angle, and mixed pitch angle-energy) diffusion.

As equation 4.3 shows, radial diffusion should be solved on a (μ, J, L) grid, and local diffusion on a (p, α_{eq}, L) grid. The grid employed for calculating radial diffusion ensures particles can only change L shells along lines of constant invariants μ and J. Panels A to C of Figure 4.1 depict different views of such grid. Panel A presents a 3D view, and panel B the cross sections in L. In accordance with the conservation of μ, the energy range increases as L decreases. A specific 2D cross section of the radial diffusion grid at $L = 3$ is shown in panel C.

To calculate local diffusion, the PSD values are interpolated on a grid that is orthogonal in energy and pitch angle. A 3D view of the calculation grid, the L cross sections, and a specific cross section at $L = 3$ are depicted in panels D to F of Figure 4.1. This grid has perpendicular lines for pitch angle and energy at each L.

The inclusion of magnetopause shadowing warrants a more detailed description. The VERB-3D code includes the LCDS (see Section 3.3.2.3) as a function of time and invariant K. In this study, physics associated with magnetopause shadowing is introduced using the LCDS. An energy-dependent loss mechanism is employed, since the rate of loss following a reduction in the LCDS depends on the particle's drift period. The TS07 magnetic field model (Tsyganenko and Sitnov, 2007) incorporated into the International Radiation Belt Environment Modelling library (IRBEM; Boscher et al., 2010) is used to determine the LCDS, and loss due to magnetopause shadowing is simulated with an exponential decay of the electron PSD outside the LCDS, as:

$$f(t, L^* > \text{LCDS}(t)) = f(t)e^{(-1/\tau_d)}, \tag{4.5}$$

where τ_d is the electron drift period as in equation 2.65.

At each time step, loss due to magnetopause shadowing is first performed according to the exponential decay of electron PSD given by equation 4.5. Following this, radial diffusion is calculated for each pitch angle and energy on the radial diffusion grid. Then, the resulting PSD values are interpolated on the local diffusion grid to calculate the energy, pitch angle, and mixed pitch angle-energy diffusion for

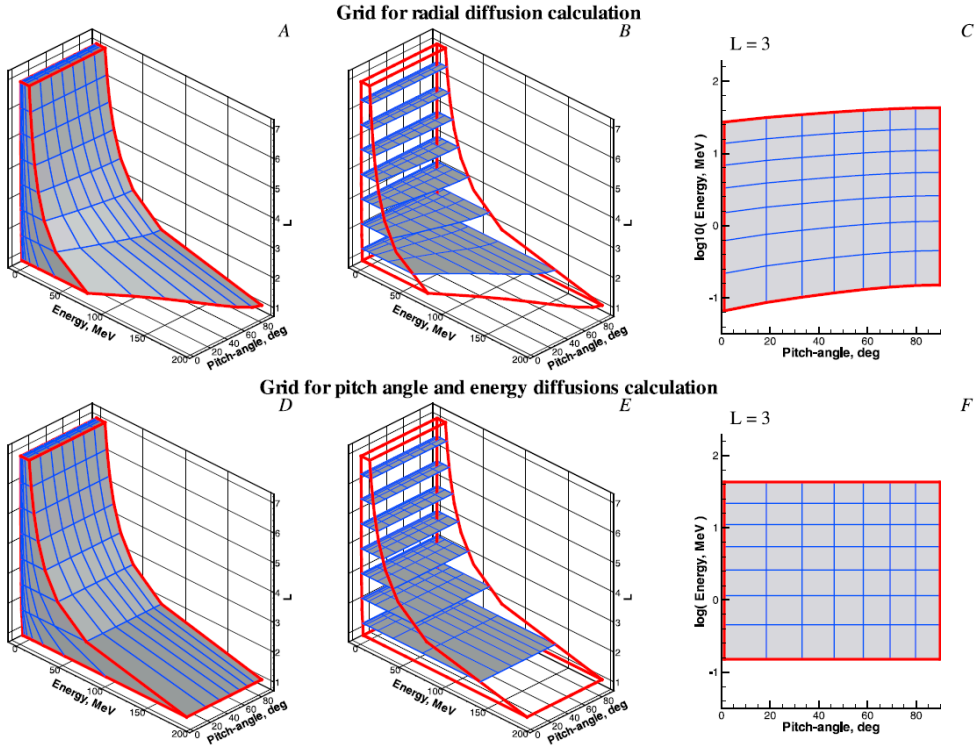

FIGURE 4.1: Computational grid in variables L, p, and α_{eq} for the radial diffusion operator, with μ and J constant along the L lines: (A) 3D view, (B) radial diffusion grid in several L cross sections, and (C) one cross section at $L = 3$. (D, E, and F) The same for the local diffusion grid. At each L plane, this grid is orthogonal in p and α_{eq} coordinates (Subbotin and Shprits, 2009).

each L. After performing local diffusion, the result is interpolated back to the radial diffusion grid and the next time step begins.

Owing to the exponential decrease of PSD with increasing energy, the logarithm of PSD is interpolated in order to minimise interpolation errors. Subbotin and Shprits (2009) tested different interpolation methods, and found that the spline interpolation produced the most accurate results without changing the shape of the interpolation function, in comparison to the the linear method.

4.2.2 Diffusion Coefficients

The parametrisation for the radial diffusion coefficients due to magnetic field fluctuations is computed following Brautigam and Albert (2000) as:

$$D_{L^*L^*} = 10^{0.056Kp-9.325}L^{*10}. \tag{4.6}$$

The radial diffusion coefficients $D_{L^*L^*}$ are shown in Figure 4.2, for the L^* range between 3 and 6.6. The radial diffusion coefficients increase with Kp, and thus, diffusion is faster during times of disturbed geomagnetic activity. Due to the L^{*10} dependence, $D_{L^*L^*}$ is most significant at the largest L^* values, and hence, radial diffusion is mainly important in the outer belt region.

Pitch-angle, energy, and mixed pitch angle-energy diffusion coefficients due to dayside and nightside chorus, plasmaspheric hiss, and EMIC waves, are calculated using the Full Diffusion Code (Ni et al., 2008; Shprits and Ni, 2009). The amplitude

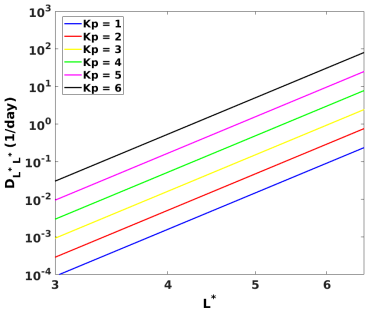

FIGURE 4.2: Electromagnetic radial diffusion coefficients $D_{L^*L^*}$ as given by Brautigam and Albert (2000).

of chorus and hiss waves is scaled with Kp. The parameters for dayside and nightside chorus are taken from Orlova and Shprits (2014), while for hiss the parametrisation of Orlova, Spasojevic, and Shprits (2014) is used. The spectral properties from Meredith et al. (2014) are used to calculate diffusion coefficients for helium band EMIC waves. The parameters of the waves employed in this thesis are summarised in Table 4.1.

Figure 4.3 shows the averaged pitch-angle, energy, and mixed pitch angle-energy diffusion coefficients in logarithmic color scale, computed at $L = 4.5$ due to dayside chorus, nightside chorus, and plasmaspheric hiss, following the wave parameters shown in Table 4.1. For dayside chorus, pitch- angle scattering rates (Figure 4.3a) are stronger for the lower-energy electrons than for the higher-energy ones, whereas energy diffusion rates (Figure 4.3d) are the highest for electrons with energies around 1 MeV. Dayside chorus minimises scattering at high pitch angles, and maximises losses near the edge of the loss cone. On the nightside, pitch-angle and energy diffusion rates due to chorus (Figure 4.3b and Figure 4.3e) are higher for lower-energy electrons, and peak at higher equatorial pitch angles, therefore providing significant pitch angle scattering for the electrons that mirror near the equator.

The pitch-angle diffusion coefficients for plasmaspheric hiss (Figure 4.3c) are between two and three orders of magnitude higher than the energy diffusion rates (Figure 4.3f), thus, hiss mostly causes pitch-angle scattering. Moreover, both pitch-angle and energy diffusion coefficients are higher for lower-energy electrons, about a few hundred keV. Diffusion coefficients also peak at higher pitch angles around 70º, indicating that plasmaspheric hiss is mainly effective in redistributing nearly equatorially mirroring electrons.

Figure 4.4 shows pitch-angle scattering rates for EMIC waves according to the parameters in Table 4.1 and two different ion composition rates. In the first case, the ion composition used is assumed to be 70% H^+, 20% He^+, and 10% O^+ as in Meredith et al. (2003c), while in the second case the rates are 94% H^+, 5% He^+, and 1% O^+ as in Kersten et al. (2014). Varying the ion composition affects the minimum resonant energy and the maximum equatorial pitch angle for effective electron scattering. With the ion composition in (a), electrons with pitch angle equal to 52º (corresponding to the invariant $K = 0.11\ G^{0.5}R_E$ using a dipole approximation) and energy > 2.5 MeV are affected by EMIC waves, whereas for the ion composition in (b) such minimum resonant energy increases up to 5 MeV. The ion composition in (a), namely 70% H^+, 20% He^+, and 10% O^+, is used in the current thesis.

TABLE 4.1: Wave parameters used for computing pitch- angle, energy, and mixed pitch angle-energy diffusion coefficients. The spatial and spectral wave properties presented in this table are wave amplitude B_w, maximum latitude at which waves are present $\lambda_{\max}$, density model used for computation, percentage of the MLT orbit with resonant wave-particle interactions, wave spectral properties ($\omega_m, \delta\omega, \omega_{uc}$, and ω_{lc}), and wave normal angle distribution.

Wave type	B_w(pT)	$\lambda_{\max}$(°)	Density model	MLT(%)	Wave spectral properties	Distribution in wave normal
Chorus day	$10^{0.75+0.04\lambda}(2\times10^{0.73+0.91Kp}/3319.2)^{0.5}, Kp \leq 2+$ $10^{0.75+0.04\lambda}(2\times10^{2.5+0.18Kp}/3319.2)^{0.5}, 2+ < Kp \leq 6$	35	Sheeley et al. (2001)	25	$\omega_m/\Omega_e = 0.2$, $\delta\omega/\Omega_e = 0.1$, $\omega_{uc}/\Omega_e = 0.3$, $\omega_{lc}/\Omega_e = 0.1$	$\theta_m = 0^o$, $\delta\theta = 30^o$, $\theta_{uc} = 45^o$, $\theta_{lc} = 0^o$
Chorus night	$50(2\times10^{0.73+0.91Kp}/3319.2)^{0.5}, Kp \leq 2+$ $50(2\times10^{2.5+0.18Kp}/3319.2)^{0.5}, 2+ < Kp \leq 6$	15	Sheeley et al. (2001)	25	$\omega_m/\Omega_e = 0.35$, $\delta\omega/\Omega_e = 0.15$, $\omega_{uc}/\Omega_e = 0.65$, $\omega_{lc}/\Omega_e = 0.05$	$\theta_m = 0^o$, $\delta\theta = 30^o$, $\theta_{uc} = 45^o$, $\theta_{lc} = 0^o$
Hiss	$30\times Kp/4$	40	Carpenter and Anderson (1992)	60	$\omega_m = 0.345\times10^4$rad/s, $\delta\omega = 0.189\times10^4$ rad/s, $\omega_{uc} = 1.25\times10^4$ rad/s, $\omega_{lc} = 0.0628\times10^4$ rad/s	$\theta_m = 0^o$, $\delta\theta = 20^o$, $\theta_{uc} = 30^o$, $\theta_{lc} = 0^o$
EMIC waves	1000	45	$\omega_p/\Omega_e = 10$	25	$\omega_m/\Omega_{O^+} = 3.6$, $\delta\omega/\Omega_{O^+} = 0.25$, $\omega_{uc}/\Omega_{O^+} = 3.85$, $\omega_{lc}/\Omega_{O^+} = 3.35$	field-aligned approximation

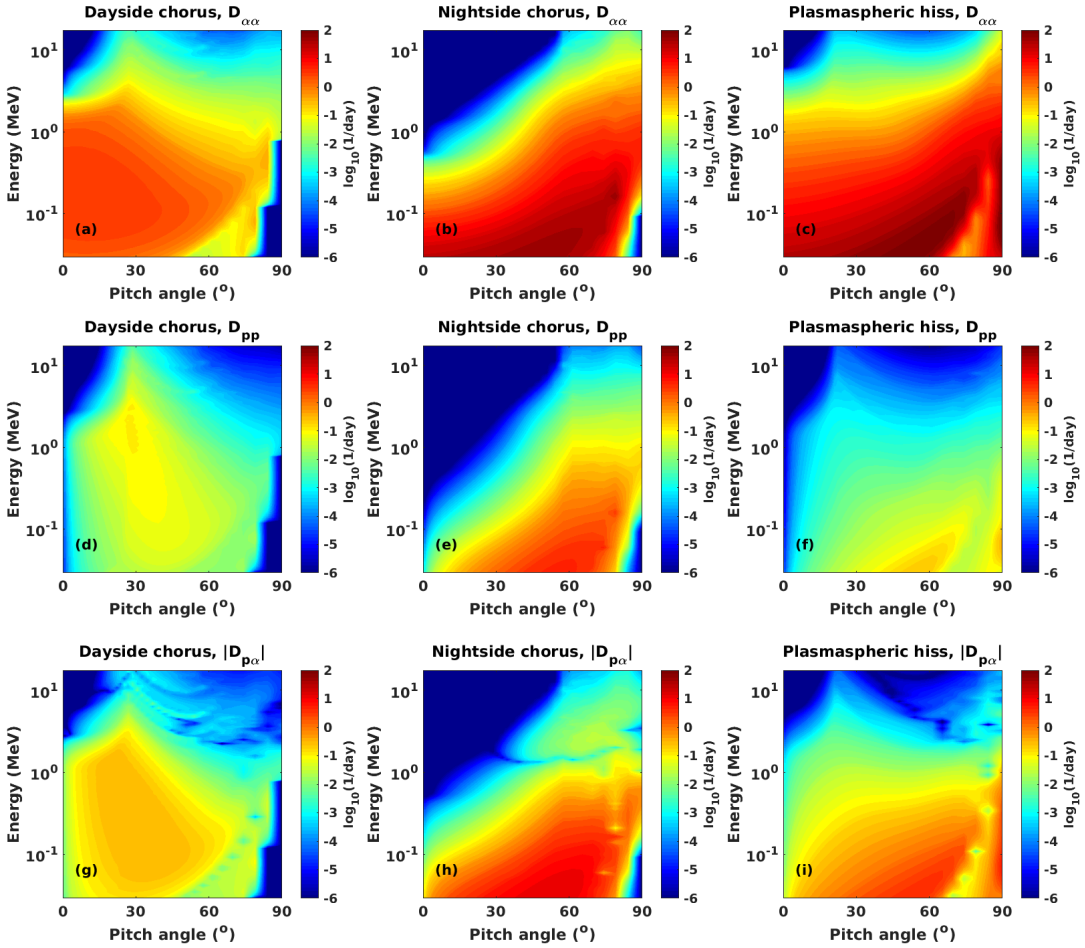

FIGURE 4.3: (top) Pitch- angle, (middle) energy, and (bottom) mixed pitch angle-energy quasi-linear scattering rates as a function of equatorial pitch angle and kinetic energy for (a, d, g) dayside chorus, (b, e, h) nightside chorus, and (c, f, i) plasmaspheric hiss at $L = 4.5$.

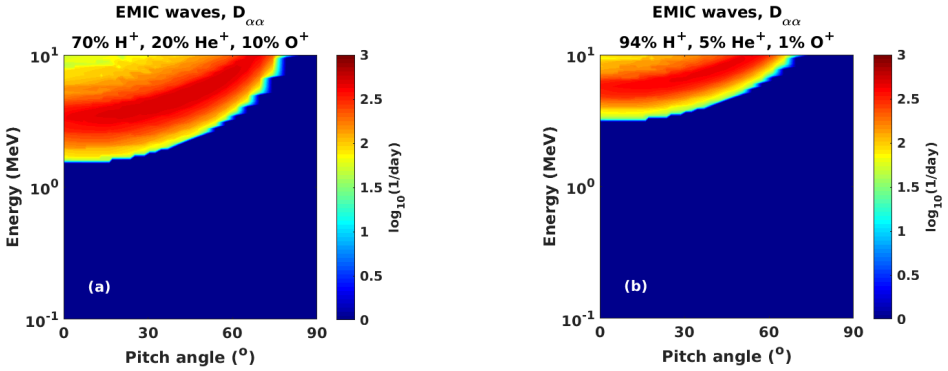

FIGURE 4.4: Two-dimensional bounce-averaged pitch-angle diffusion coefficients for helium band EMIC waves at $L = 4.5$ with (a) ion composition of 70% H^+, 20% He^+, and 10% O^+; and (b) 94% H^+, 5% He^+, and 1% O^+. All other spectral properties and MLT and latitudinal distribution are the same as in Table 4.1.

Following Meredith et al. (2014), the coefficients are scaled according to wave occurrence rate (2%). In accordance with Drozdov et al. (2017), EMIC waves are incorporated into the simulations when the solar wind dynamic pressure is greater

TABLE 4.2: Boundary conditions used in the VERB code simulations.

Boundary	Condition	Underlying physical process
$L^* = 1$	$f = 0$	Loss to atmosphere
$L^* = 6.6$	$f = f(\text{time})$	GOES measurements
$E = E_{\min}$	$f = f(\text{const})$	Balance of convective source and loss
$E = E_{\max}$	$f = 0$	Absence of multi-MeV energy electrons
$\alpha_{\text{eq}} = 0^{\text{o}}$	$f = 0$	Empty loss cone
$\alpha_{\text{eq}} = 90^{\text{o}}$	$\partial f / \partial \alpha_{\text{eq}} = 0$	Flat pitch-angle distribution

than or equal to 3 nPa. It is worth emphasising that only helium band EMIC waves are included in the current study.

The plasmapause location L_{pp} is estimated using the parametrisation of Carpenter and Anderson (1992):

$$L_{pp} = 5.6 - 0.46 Kp_{\text{max24}}, \tag{4.7}$$

where Kp_{max24} is the maximum Kp value in the preceding 24 hours. The plasmapause location is assumed to separate plasmaspheric hiss inside the plasmasphere, and chorus and EMIC waves outside the plasmasphere.

4.2.3 Boundary and Initial Conditions

To solve equation 4.3 and perform 3D simulations of the radiation belts, six boundary conditions need to be specified, two for each variable in the equation, and these are summarised in Table 4.2. A lower radial boundary condition ($L^* = 1$) of $f = 0$ is used in order to simulate the loss of electrons to the atmosphere. The PSD required for the upper radial boundary condition ($L^* = 6.6$) is obtained from Geostationary Operational Environmental Satellites (GOES) observations, introduced in the next chapter. For the lower energy boundary, PSD is set constant in time to represent a balance of convective source and loss. At the upper energy boundary (10 MeV at $L^* = 6.6$), an absence of electrons is assumed, and therefore PSD is set equal to zero. The lower pitch-angle boundary condition is set to zero to simulate precipitation loss of electrons into the loss cone in a weak diffusion regime. A zero gradient is chosen to account for the flat pitch-angle distribution observed at 90° (Horne et al., 2003) for the upper pitch-angle boundary condition.

For the solution of equation 4.3, the initial PSD is taken from the steady state solution of the radial diffusion equation:

$$0 = L^{*2} \frac{\partial}{\partial L^*}\bigg|_{\mu,J} \left(\frac{1}{L^{*2}} D_{L^*L^*} \frac{\partial f}{\partial L^*}\bigg|_{\mu,J} \right) - \frac{f}{\tau}. \tag{4.8}$$

Following Shprits, Subbotin, and Ni (2009) and Subbotin and Shprits (2009), the diffusion rate $D_{L^*L^*}$ is computed using an initial Kp of 2, and the lifetime is assumed to be $\tau = 10$ days.

Chapter 5

Instrumentation

The research presented in this thesis utilises data from two satellite missions: the twin Van Allen Probes (Mauk et al., 2012; Stratton, Harvey, and Heyler, 2012), of which two examples of electron flux measurements were presented in Chapter 2, and the multi-satellite Geostationary Operational Environmental Satellites (GOES) fleet (GOES-N Data Book, 2005). Data from the OMNIWeb interface (King and Papitashvili, 2005) are also employed in this study. In particular, solar wind dynamic pressure and geomagnetic indices *Kp* and *Dst* (introduced in Section 2.3.4) are used to interpret the results and to drive the VERB model. This chapter consists of an overview of the different instruments on board the spacecraft that provide the data used in the current work.

5.1 Van Allen Probes

The Van Allen Probes, formerly known as Radiation Belt Storm Probes (RBSP) Mission, are part of NASA's Living With a Star program. The underlying purpose of this mission is to provide a better understanding of the fundamental physical processes that drive changes within the Earth's radiation belts, some of which were introduced in Chapter 3. The Van Allen Probes were launched on August 30 2012, and the instruments on board both spacecraft provided data on the radiation belt region until the end of operations on 18 October 2019. Each probe is equipped with a set of eight instruments that measure particle intensities over a wide range of energy and species, as well as the magnetic and electric fields over a large spread of frequencies.

5.1.1 Mission Overview

The Van Allen Probes mission comprises two spacecraft (RBSP-A and RBSP-B) making in-situ measurements in nearly the same highly elliptical, low inclination (10^{o}), $\sim$ 9 hour period orbits close to the magnetic equatorial plane. The spin period of the Van Allen Probes is $\sim$ 11 s, with the spin axis roughly Sun pointing. Perigee is located at an altitude of $\sim$ 500 km while apogee is at $\sim$ 5.8 R_E. The orbits of both spacecraft are slightly different so that one probe overtakes the other about every 2.5 months. The eccentricity of their orbits allows for measurements of the radiation belt particles and environment, while traversing the inner belt, the slot region, and most of the outer belt. The orbit of the Van Allen Probes precesses around the Earth at a rate of $\sim 210^{o}$ per year. An example of the orbital trajectories for Probes A and B is shown in Figure 5.1 in Geocentric Solar Ecliptic coordinates.

The fundamental objective of the Van Allen Probes mission was to provide an understanding of how relativistic electrons and penetrating ions in space form or

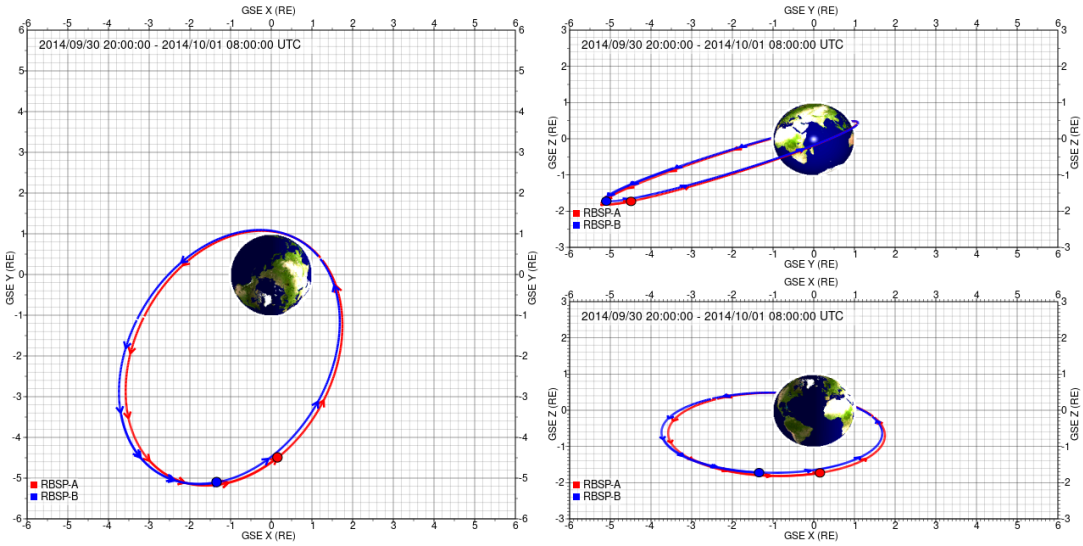

FIGURE 5.1: Orbit of the Van Allen Probes A and B on 01 October 2014, between 08:00 UT and 20:00 UT in GSE coordinates in the XY plane (left), the YZ plane (top right), and the XZ plane (bottom right). The trajectory of Probe A is shown in red and Probe B in blue.

change in response to variable energy inputs from the Sun. Three overarching science questions have been formulated in order to accomplish this broad objective (Mauk et al., 2012):

1. Which physical mechanisms produce radiation belt enhancements?
2. What are the dominant processes for relativistic electron loss?
3. How do geomagnetic processes affect radiation belt behaviour?

The science learned with this mission has enhanced the community's understanding of the physics at work in the Earth's radiation belts, and it has also allowed for the development of new models of the radiation environment and its effects on spacecraft hardware.

The observations performed by the RBSP mission are supported by a variety of experiments in each spacecraft. Of particular relevance to this thesis is the Energetic Particle, Composition, and Thermal Plasma suite (ECT, Spence et al., 2013), which consists of three highly-coordinated instruments (Figure 5.2): the Helium Oxygen Proton Electron (HOPE) sensor, the Magnetic Electron Ion Spectrometer (MagEIS), and the Relativistic Electron Proton Telescope (REPT). The latter two instruments are utilised in the following research chapters.

5.1.2 MagEIS

The Magnetic Electron Ion Spectrometer (Blake et al., 2013) is part of the ECT suite, onboard each of the two RBSP spacecraft. MagEIS is composed by four magnetic spectrometers, one low-energy unit (20 to 240 keV), two medium-energy units (80- to 1200 keV), and a high-energy unit (800 to 4800 keV). The spectrometers are mounted in the anti-solar deck of the probes. The low-energy, one medium-energy, and the high-energy units point 75° with respect to the satellite spin axis, and the second medium-energy unit points 35° with respect to the spin axis, the data from which is not typically included in the publicly available MagEIS files. The high-energy spectrometer also contains a proton telescope (55 keV to 20 MeV). MagEIS electron measurements are employed in this thesis, thus MagEIS proton measurements are not discussed further.

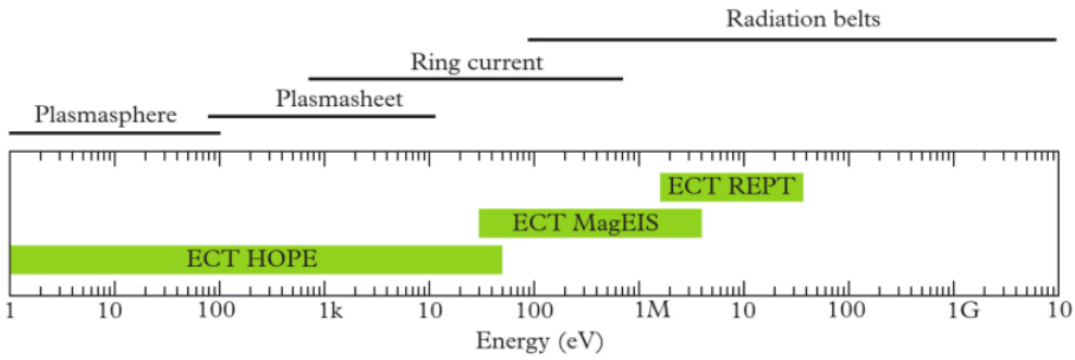

FIGURE 5.2: Particle experiments on board the ECT suite. Typical energy ranges of electrons in different regions of the magnetosphere are shown at the top. Adapted from Takahashi and Miyoshi (2016).

The magnetic focusing measurement technique used by the MagEIS electron spectrometers is illustrated in Figure 5.3. Electrons enter through a collimator with a field of view of $10^o \times 20^o$. Inside the chamber the magnetic field is uniform, and it focuses the electrons on a linear strip of silicon detectors, after the velocity of the incoming electrons has rotated through 180^o. Protons that enter through the collimator (indicated by the red arrows in Figure 5.3), are deflected away from the focal plane. The internal magnetic field strength inside the instrument chamber is $\sim 550, 1600,$ and 4800 G (1 G = 10^{-5} nT) for the low-, medium-, and high-energy units, respectively.

The low and medium-energy instruments ("LOW" and "MED" in Figure 5.3) are designed identically and only differ in the thickness of the detectors and the internal magnetic field strength. In these units, the focal plane consists of nine silicon solid-state detectors (or "energy pixels"), labelled as P0 to P8 in Figure 5.3, arranged along the entrance wall of the unit. Higher-energy electrons strike the higher-numbered pixels of increased size, located further along the focal plane.

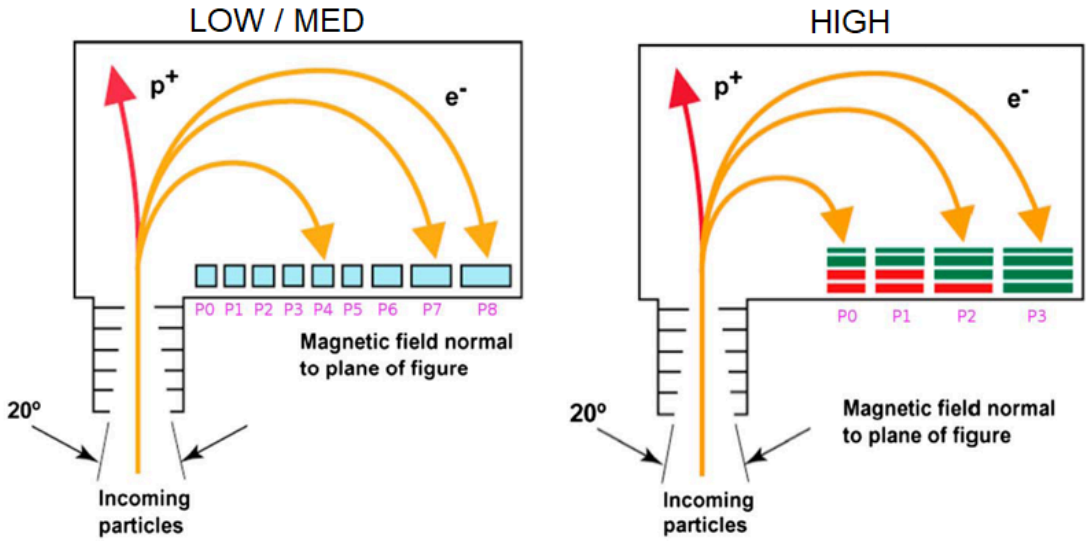

FIGURE 5.3: Schematic diagram of the MagEIS instruments. The low and medium-energy units are shown in the left and have nine pixels indicated by P0-P8. The high-energy unit is shown in the right and has four pixels, labelled as P0-P3 (Claudepierre et al., 2015).

In contrast, there are four pixels in the high-energy spectrometer ("HIGH" in Figure 5.3). Each pixel stack consists of four individual silicon solid-state detectors, thus there are 16 detectors in total in the high-energy unit. An individual pixel contains a thin front detector arranged with thicker rear detectors. The increasing thickness of the rear detector stacks is designed to stop electrons of increasing energy within the detectors. Since the gyroradius increases with electron energy, pixels 0 and 1 use only one of the three rear detectors, pixel 2 uses two, and pixel 3 uses all three. The active rear detectors are coloured green and the unused are shown in red.

In total, across the three energy units of the detector, MagEIS measurements are provided in 21 energy channels. Figure 5.3 shows that as the pixel number increases, the surface area of the pixel also increases, and the energy passband (the electron energy range steered towards the pixel) widens within a given unit. This maintains a roughly uniform count rate across all pixels in an individual unit, and compensates for the effect of a falling spectrum. On a given pixel, pulse-height analysis is used for each individual detection event (i.e. one electron strike). Multiple detection events (electron counts) are accumulated over some time interval. Then, the count rate (counts/second) is obtained as a function of energy deposit for a given pixel. The electron counts within a given energy passband are summed on board to produce the main channel data.

As the Van Allen Probes are a spinning spacecraft, the pitch-angle distribution can be calculated by sectoring the measurements from each spin into an integer number of angular partitions. The data provided to the user is binned in 11 pitch angles and is available at the spin time cadence. For the current work, the pitch-angle distribution is interpolated in a uniform grid with a step of 5^{o}.

5.1.3 REPT

The Relativistic Electron-Proton Telescope (Baker et al., 2013) is another instrument of the ECT suite on board each of the Van Allen Probes. The instrument points perpendicular to the spin axis of the spacecraft, and measures electrons in the energy range $\sim$ 1 to 20 MeV in 12 energy channels. Protons in the energy range $\sim$ 17 to 200 MeV are also measured. Pulse-height analysis is used to separate electrons from protons. As REPT proton measurements are not the focus of this work, they will not be discussed further.

Very high-energy particles are ideally measured with a compact solid-state telescope, as other systems (e.g. magnetic spectrometers) would require strong magnetic fields, resulting in massive instruments. REPT consists of a stack of high-performance solid-state detectors in a telescope configuration, a collimator, and a thick aluminium case that surrounds the detector in order to shield the sensors from penetrating radiation and brehmsstrahlung X-rays.

Figure 5.4 shows a cross-section of the REPT detector system. The REPT collimator has an aperture of 32^{o}. A beryllium window (white outline) located at the back of the collimator excludes lower-energy electrons ($\lesssim$ 1 MeV). Nine silicon detectors (in blue), labelled R1 to R9, are stacked behind the beryllium window, with larger-area detectors R3 to R9 twice as thick as the front detectors. The REPT telescope samples particles from all local pitch angles, and data is provided in 17 pitch-angle bins with a time resolution of the spin period. For this study, similar to MagEIS data, REPT pitch-angle distributions are also interpolated in a 5^{o} step uniform grid. Finally, as pointed by Boyd et al. (2019), the first five REPT channels each have a nearby (within 0.2 MeV) MagEIS-HIGH channel. Measurements from MagEIS for channels $>$ 2 MeV were neglected in the current work.

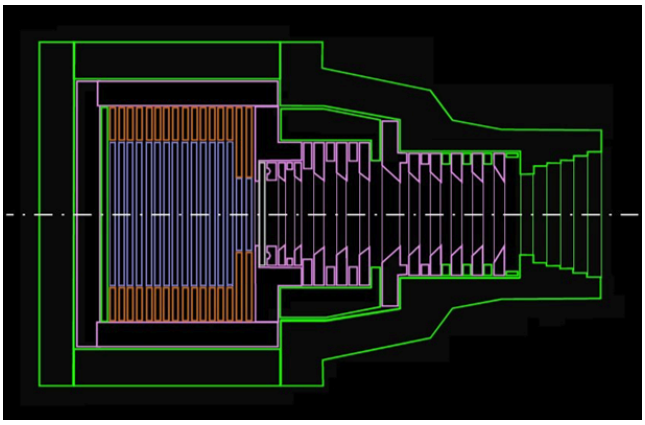

FIGURE 5.4: REPT instrument in cross section. Material marked in green is aluminium, and in white is beryllium. The silicon detectors are shown in blue (Baker et al., 2013).

5.2 Geostationary Operational Environmental Satellites (GOES)

The multimission GOES program (Onsager et al., 1996; Singer et al., 1996) is aimed at monitoring the near-Earth space, including operational meteorology and space weather. The GOES constellation provides the data and imagery used for daily weather forecasting and also measures energetic particle variations in the inner magnetosphere. Data from GOES 13 and 15, part of the GOES-N series, and launched on 24 May 2006 and 04 March 2010, respectively, are used in the current study.

5.2.1 Mission Overview

GOES spacecraft operate in GEO orbit, 35790 km above the equator, and with orbital period of one day. As stated in the GOES-N Data Book (2005), the mission goals of the GOES program are to:

1. Maintain continuous, reliable operational and environmental warning systems to protect life and property.

2. Monitor the Earth's surface and space environmental conditions.

3. Develop and provide new and improved applications and products for a wide range of federal agencies, governments, and private users.

These objectives are supported by a variety of components of the GOES-N payloads. In particular, the Space Environment Monitor subsystem contains multiple instruments including, among others, the Energetic Particle Sensor (EPS)/High Energy Proton and Alpha Detector (HEPAD) instrument that measures the flux of protons, alpha particles, and electrons over an extensive range of energies. Specifically, data from the MAGnetospheric Electron Detector (MAGED) and Energetic Proton, Electron, and Alpha Detector (EPEAD) instruments are relevant for the work conducted in this thesis. EPS/HEPAD instrument locations on the GOES spacecraft are shown in Figure 5.5.

5.2.2 MAGED

The MAGnetospheric Electron Detector instrument (Hanser, 2011) consists of nine solid-state detectors in a cruciform configuration with five telescopes in the east-west (equatorial) plane and four telescopes in the north-south (meridional) plane (Rodriguez, 2014a). Each telescope makes pitch-angle-resolved electron flux measurements in five energy bands: 30 to 50, 50 to 100, 100 to 200, 200 to 350, and 350 to

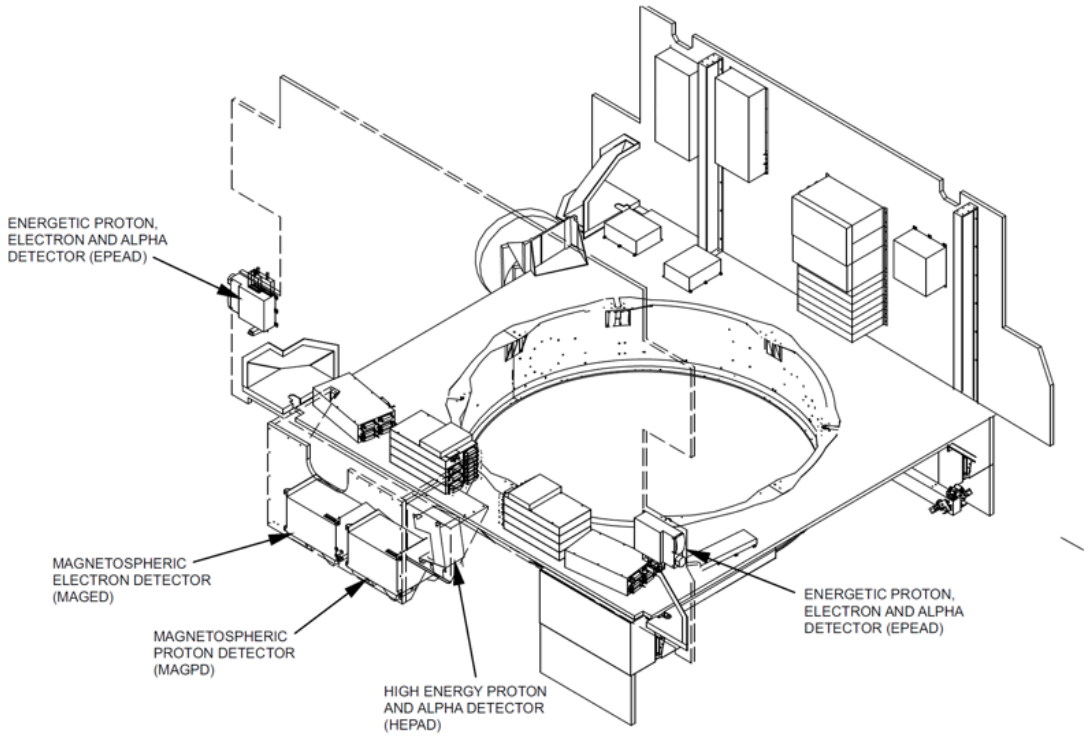

FIGURE 5.5: EPS/HEPAD instrument locations (GOES-N Data Book, 2005).

600 keV. MAGED measures electrons at nine pitch-angle directions. The detector sets are mounted on the anti-Earth side of the satellite and measure protons or electrons at 0^o, $\pm 35^o$, and $\pm 70^o$ from the anti-Earth direction in both the equatorial and the azimuthal plane. The pitch-angle distribution below 600 keV is directly measured by MAGED. Data is provided to the user at a 1-min resolution.

5.2.3 EPEAD

There are two Energetic Proton, Electron, and Alpha Detector instruments (Onsager et al., 1996; Hanser, 2011) on each satellite, one oriented westward and the other eastward (Rodriguez, 2014b), mounted on opposite sides of the spacecraft in order to measure the required equatorial angular coverage. The detectors provide integral electron flux measurements in two energy ranges: > 0.8 MeV and > 2 MeV. EPEAD integral fluxes are obtained by averaging the measurements over the westward and eastward telescopes, so that the resulting pitch angles are averages between both directions of the two telescopes as well. Integral fluxes as a function of energy are fitted to a power law, which is used to interpolate between values up to 1 MeV. In order to convert to differential flux, the 90^o pitch-angle differential flux data from MAGED is employed and the two integral channels of EPEAD are fitted to an exponential function $j = A \times \exp(B \times E)$, where j is the differential flux, E is the energy, and A and B are positive time-dependent coefficients obtained by solving the flux integral for averaged MAGED data.

Chapter 6

Data Assimilation and the Kalman Filter

Stated in general terms, data assimilation is a procedure in which observations are combined with models. The result is a more accurate and more complete description of the state of the system than that obtained by either model simulations or observations alone. There is a wide range of data assimilation techniques used throughout a variety of disciplines, from engineering and assisted navigation to meteorology and space physics.

In the first section of this chapter, the concept of data assimilation is presented, and two different approaches, the sequential and the variational, are discussed. Then, the Kalman filter and its diverse versions are introduced, and its classical formulation is outlined. Finally, specific details concerning the implementation of the filter to the present research work are presented, and a suboptimal method, known as the split-operator Kalman filter, is described.

6.1 Data Assimilation

Analysis of radiation belt observations, such as those shown in Chapter 3, poses a number of challenges. Satellite measurements are often limited to a restricted range of L shells, pitch angles, and energies, and also may have different observational errors. Therefore, the analysis of data from individual spacecraft does not allow for inferring and reproducing the global state of the radiation belts. The manual analysis of observations is a challenging task, while an automated analysis is complicated by the fact that measurements at different L shells are taken at different points along the spacecraft orbit and therefore at different times. Moreover, fluxes of energetic electrons in the outer belt change on timescales shorter than a typical satellite orbital period; thus, it is impossible to observe the instantaneous radial profiles of fluxes.

Similar challenges to those mentioned above were faced by the atmospheric sciences in the 1970s (Kalnay, 2003). A powerful method, inherited from the engineering of navigation systems and referred to as "data assimilation", was successfully applied to accomplish better numerical weather predictions. Talagrand (1997) defined data assimilation, in the context of oceanography and meteorology, as "the process through which all the available information is used in order to estimate as accurately as possible the state of the atmospheric or oceanic flow". In a more general sense, data assimilation is an algorithm in which model results and sparse data from various sources, contaminated by noise and errors, are optimally combined, and the result is typically referred to as "reanalysis". Data assimilation is therefore a two-way communication, as theoretical models fill the gaps where observations

are lacking and correct inaccurate measurements, while the observations correct the model and bring it closer to reality.

Either of two strategies can be applied for this task, referred to as sequential or variational data assimilation. The sequential approach follows a two-stage principle: starting from a previous state, we first forecast the evolution of that state, and then correct it (i.e. perform an analysis), as soon as an observation becomes available. The assimilation process is rooted in the theory of statistical estimation: a variance minimising estimate is calculated from the error statistics whenever measurements are available (Daley, 1991). An example of this approach is performed by the Kalman filter (Kalman, 1960).

Variational data assimilation emanates from optimal control theory. In contrast to sequential methods, which update the model estimate as soon as new observations are available, the variational methods calculate an estimate in space and time where the estimate at a given time depends on both past and future measurements (Evensen, 2009). Observations and model predictions are incorporated into an objective function, which is minimised in order to find the best fit state. The most popular formulation of the variational approach is the 4D-VAR method (Le Dimet and Talagrand, 1986).

The research presented in Chapters 7 and 8 is based on sequential data assimilation by means of the classical Kalman filter (Kalman, 1960); therefore, a more detailed description of this approach is presented in the next section.

6.2 The Kalman Filter

The filter algorithm of Kalman (1960) addresses the problem of estimating the state of a dynamical system, relying on a numerical model, an estimate of the initial state of the system, and a series of measurements. Kalman (1960) solved the problem for linear systems, and the algorithm became known as the classical Kalman filter (KF). Years later, Jazwinski (1970) presented the approximate formulation for nonlinear systems, called the extended Kalman filter (EKF). Afterwards, Evensen (1994) introduced the ensemble Kalman filter (EnKF), based on the utilisation of an ensemble of model simulations.

Kalman filtering is now widely accepted and has found many applications including the navigational system onboard the Apollo mission, GPS stand-alone devices, operational weather forecasting, and ocean modelling (e.g. Sorenson, 1985; Talagrand, 1997; Kalnay, 2003; Lahoz, Khattatov, and Ménard, 2010). Recently, it has successfully been applied to specify and forecast several near-Earth space particle and plasma populations, such as the ionosphere (e.g. Scherliess et al., 2004; Scherliess et al., 2006), the Van Allen radiation belts (e.g. Naehr and Toffoletto, 2005; Shprits et al., 2007; Kondrashov, Ghil, and Shprits, 2011; Cervantes et al., 2020a), and the ring current (e.g. Nakano et al., 2008; Godinez et al., 2016; Aseev and Shprits, 2019).

The KF is an optimal sequential data assimilation algorithm that minimises mean-squared errors between the state vector and the observational vector. The underlying assumption of the filter is that the errors of the model and the observations are unbiased and obey a Gaussian distribution. The KF utilises a feedback control: first it estimates the state of the system at a given time, and then it obtains feedback in the form of measurements. Hence, the equations for the KF fall in two categories: prediction equations and update (or corrector) equations. First, the prediction equations project forward in time the current state and error covariance estimates to obtain the

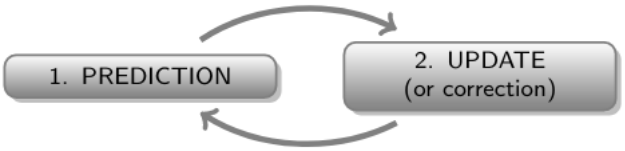

FIGURE 6.1: The ongoing discrete Kalman filter cycle.

forecast for the next time step. Then, the update equations incorporate a new measurement into the prediction to obtain an improved estimate. The ongoing discrete KF cycle is schematically represented in Figure 6.1.

The following section presents a description of the KF in discrete time, following Ghil and Malanotte-Rizzoli (1991). The set of notations that will be employed in the formulation of the KF is provided in Table 6.1.

6.2.1 Kalman Filter Methodology

For a given dynamic system described by a set of partial differential equations, the numerical algorithm can be presented in the following form:

$$\mathbf{x}_k^f = \mathbf{M}_{k-1}\mathbf{x}_{k-1}^a, \tag{6.1}$$

where $\mathbf{x}$ represents a model state vector (for our model, it is the PSD on the numerical grid locations), and the model matrix $\mathbf{M}$ advances the state vector $\mathbf{x}$ in discrete time increments Δt. The subscript k shows the time step, and superscripts f and a refer to forecast and analysis, respectively. $\mathbf{x}_k^a$ is the best estimate of the state vector at time k, relying on the model and the available observations. The evolution of $\mathbf{x}_k^t$ (superscript t refers to true), is assumed to differ from the model by a random error ϵ_k^m:

$$\mathbf{x}_k^t = \mathbf{M}_{k-1}\mathbf{x}_{k-1}^t + \epsilon_k^m, \tag{6.2}$$

TABLE 6.1: Notation of vectors and operators used in the Kalman filter. N represents the number of grid points, and m is the number of observations at time k. With the exception of the matrix I, the quantities listed in this table are time-dependent, and appear in the text with subscript k.

Variable	Dimension	Description
$\mathbf{x}^f$	$(N \times 1)$	forecast state vector
$\mathbf{x}^a$	$(N \times 1)$	assimilated (analysis) state vector
$\mathbf{x}^i$	$(N \times 1)$	innovation vector
$\mathbf{y}^o$	$(m \times 1)$	observation vector
$\mathbf{P}^f$	$(N \times N)$	forecast error covariance matrix
$\mathbf{P}^a$	$(N \times N)$	analysis error covariance matrix
$\mathbf{M}$	$(N \times N)$	model matrix
$\mathbf{H}$	$(m \times N)$	observation matrix
$\mathbf{K}$	$(N \times m)$	Kalman gain matrix
$\mathbf{Q}$	$(N \times N)$	model error covariance matrix
$\mathbf{R}$	$(m \times m)$	observational error matrix
$\mathbf{I}$	$(N \times N)$	identity matrix

where ϵ_k^m is assumed to be a Gaussian white-noise sequence ($\mathbb{E}(\epsilon^m) = 0$), with mean zero and model-error covariance matrix $\mathbf{Q}$. The symbol $\mathbb{E}$ represents the expectation operator over time. The model error accounts for inaccurate model physics, e.g. errors in boundary conditions or numerical discretisation.

The statistical properties of the forecast error are described by a covariance matrix $\mathbf{P}_k^f$ given by:

$$\mathbf{P}_k^f = \mathbf{M}_{k-1}\mathbf{P}_{k-1}^a\mathbf{M}_{k-1}^T + \mathbf{Q}_{k-1}. \tag{6.3}$$

The observations $\mathbf{y}_k^o$ (superscript o refers to observed), are assumed to be contaminated by observational errors ϵ_k^o:

$$\mathbf{y}_k^o = \mathbf{H}_k\mathbf{x}_k^t + \epsilon_k^o, \tag{6.4}$$

where ϵ_k^o is also assumed to be Gaussian, white in time, with mean zero ($\mathbb{E}(\epsilon^o) = 0$) and given observational-error covariance matrix $\mathbf{R}$. The observational error includes instrumental and sampling errors. In radiation belt reanalysis, errors may also arise from inaccuracies associated with the external magnetic field models, which are essential in the determination of the adiabatic invariants and electron PSD. The observation matrix $\mathbf{H}_k$ accounts for the fact that usually the dimension of $\mathbf{y}_k^o$ is less than the dimension of $\mathbf{x}_k^t$ (i.e. only certain variables are observed).

During the so-called update (or analysis) step, when observations are available, forecast and observations are blended to yield the analysis state vector:

$$\mathbf{x}_k^a = \mathbf{x}_k^f + \mathbf{K}_k(\mathbf{y}_k^o - \mathbf{H}_k\mathbf{x}_k^f), \tag{6.5}$$

where the term $\mathbf{K}_k\left(\mathbf{y}_k^o - \mathbf{H}_k\mathbf{x}_k^f\right)$ is usually referred to as the innovation vector $\mathbf{x}_k^i$. $\mathbf{K}_k$ is the Kalman gain matrix computed at each time step. On the analysis step the error covariance matrix is also updated:

$$\mathbf{P}_k^a = \left(\mathbf{I} - \mathbf{K}_k\mathbf{H}_k\right)\mathbf{P}_k^f. \tag{6.6}$$

When no observations are available at time $k\Delta t$, $\mathbf{H}_k = 0$, only the forecast step is performed, $\mathbf{x}_k^a = \mathbf{x}_k^f$ and $\mathbf{P}_k^a = \mathbf{P}_k^f$. The Kalman gain matrix $\mathbf{K}_k$ is computed by minimising the analysis error covariance $\mathrm{tr}\mathbf{P}_k^a$, and it represents the optimal weights given to the observations when updating the model state vector:

$$\mathbf{K}_k = \mathbf{P}_k^f\mathbf{H}_k^T\left(\mathbf{H}_k\mathbf{P}_k^f\mathbf{H}_k^T + \mathbf{R}_k\right)^{-1}. \tag{6.7}$$

The innovation vector $\mathbf{x}_k^i$ measures how much new and additional information, provided by the data (hence its name), will modify the model forecast $\mathbf{x}^f$ in order to produce an optimal estimate of the state of the system $\mathbf{x}^a$. The value and the sign of the innovation vector depend on how much the modelled and observed values differ from each other, and on the estimated forecast and observational errors. A perfect model would predict exactly the incoming observations (i.e. complete agreement between the predicted estimate and the actual observation), and the innovation would be zero. As the forecast error covariance matrix $\mathbf{P}_k^f$ tends to zero, the innovation is weighted less heavily by the gain $\mathbf{K}_k$:

$$\lim_{\mathbf{P}_k^f \to 0} \mathbf{K}_k = 0. \tag{6.8}$$

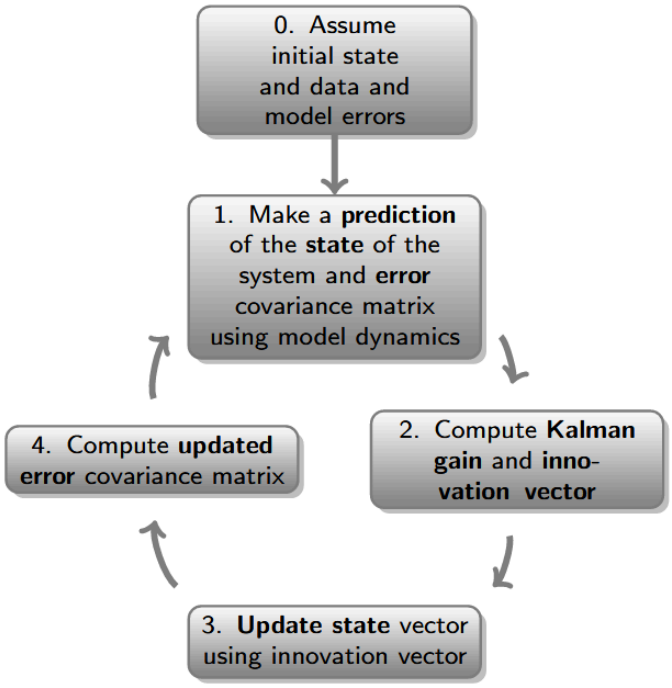

FIGURE 6.2: Flow diagram of the recursive Kalman filter algorithm.

In contrast, as the observational error covariance matrix $\mathbf{R}_k$ approaches zero, the Kalman gain $\mathbf{K}_k$ weights the innovation more heavily:

$$\lim_{\mathbf{R}_k \to 0} \mathbf{K}_k = \mathbf{H}_k^{-1}. \tag{6.9}$$

The weighting by the Kalman gain matrix can also be interpreted in the following way: as the forecast error covariance matrix $\mathbf{P}_k^f$ approaches zero, the measurement $\mathbf{y}_k^o$ is trusted less, while the prediction $\mathbf{H}_k \mathbf{x}_k^f$ is trusted more. On the other hand, as the observational error covariance matrix $\mathbf{R}_k$ tends to zero, the observation is trusted more, whereas the predicted value is trusted less.

A flow diagram summarising all steps of the KF is provided in Figure 6.2, where step 1 corresponds to the prediction stage, and steps 2 to 4, to the update stage. Table 6.2 offers a complete picture of the operation of the filter, combining the flowchart of Figure 6.2 and equations 6.1 to 6.7, categorising them either as prediction or update equations.

6.2.2 Split-Operator Kalman Filter

Data assimilation with the VERB-3D code allows us to assimilate a vast amount of data, with pitch-angle distributions and energy spectra at various radial distances and from multiple spacecraft. Nevertheless, the computational requirements for a 3D KF become very large in 3D state space. In particular, it requires operating on and storing a very large error covariance matrix. Hence, in the case of multidimensional systems, computational requirements of the optimal KF become very demanding.

In this regard, several suboptimal but computationally feasible versions of the KF for large numerical models have been proposed. One of them is a so-called split-operator approach, introduced and successfully applied in the 3D formulation of the

TABLE 6.2: Kalman filter prediction and update equations.

Prediction equations	Update equations
(1) Project the state ahead: $\mathbf{x}_k^f = \mathbf{M}_{k-1}\mathbf{x}_{k-1}^a$	(1) Compute the Kalman gain: $\mathbf{K}_k = \mathbf{P}_k^f \mathbf{H}_k^T \left(\mathbf{H}_k \mathbf{P}_k^f \mathbf{H}_k^T + \mathbf{R}_k\right)^{-1}$
(2) Project the error covariance ahead: $\mathbf{P}_k^f = \mathbf{M}_{k-1}\mathbf{P}_{k-1}^a \mathbf{M}_{k-1}^T + \mathbf{Q}_{k-1}$	(2) Update the estimate with the measurement: $\mathbf{x}_k^a = \mathbf{x}_k^f + \mathbf{K}_k(\mathbf{y}_k^o - \mathbf{H}_k \mathbf{x}_k^f)$
	(3) Update the error covariance: $\mathbf{P}_k^a = (\mathbf{I} - \mathbf{K}_k \mathbf{H}_k)\, \mathbf{P}_k^f$

VERB code by Shprits et al. (2013a) and Kellerman et al. (2014), and employed in the subsequent chapters. Using this approach, the standard formulation of a KF is still applied but only for the 1D diffusion operators in radial distance, energy, and pitch angle in a sequential manner. In this case, the KF operates on much smaller matrices sequentially, for each grid line along radial, energy, and pitch-angle directions. The omission of the mixed pitch angle-energy diffusion terms by the split-operator approach is accounted for by the innovation vector, introduced in Section 6.2.1. An example of the applicability of the innovation to estimate the missing physics due to the lack of mixed diffusion is presented in Chapter 7.

6.2.3 Filter Parameters

The standard formulation of the KF assumes that the model and observational error covariance matrices ($\mathbf{Q}$ and $\mathbf{R}$, respectively) are known. This rarely happens in practice and simple approximations are usually made. In the current study, the initial error covariance matrices are set equal to zero. The model error covariance matrix $\mathbf{Q}_k$ is a diagonal matrix with elements calculated as $Q = Xf^2$, where $X = 0.5$ is the error and f is the PSD at the time of the assimilation. A similar form is assigned to the observational error covariance matrix $\mathbf{R}_k$.

In this thesis, the VERB-3D model is used with a one-hour time step, and the assimilation is performed at the same cadence using Van Allen Probes A and B and GOES 13 and 15 observations. In order to assimilate the data, they are converted from flux to PSD in phase space coordinates (L^*, μ, K). To do so, magnetic field information is required. The in-situ magnetic field measurements are used to calculate μ, while to calculate K and L^* the Tsyganenko and Sitnov (2007) model is employed.

The assumed form and values of the model and observational error covariance matrices are based on studies performed previously in the working group, e.g. Podladchikova et al. (2014a) and Podladchikova et al. (2014b). The model error mainly stems from the uncertainty in the one-hour timestep prediction, which is considerably lower than when running the VERB-3D code for longer time intervals, e.g. one-year simulations. On the other hand, the observational error accounts for uncertainties in the instrument geometric factors, data contamination, and the measurements themselves. Since each timestep starts with an already corrected previous state, and the interval of assimilation is one hour only, both model and observational errors are comparable (A. Kellerman, personal communication, 2017). Future work geared

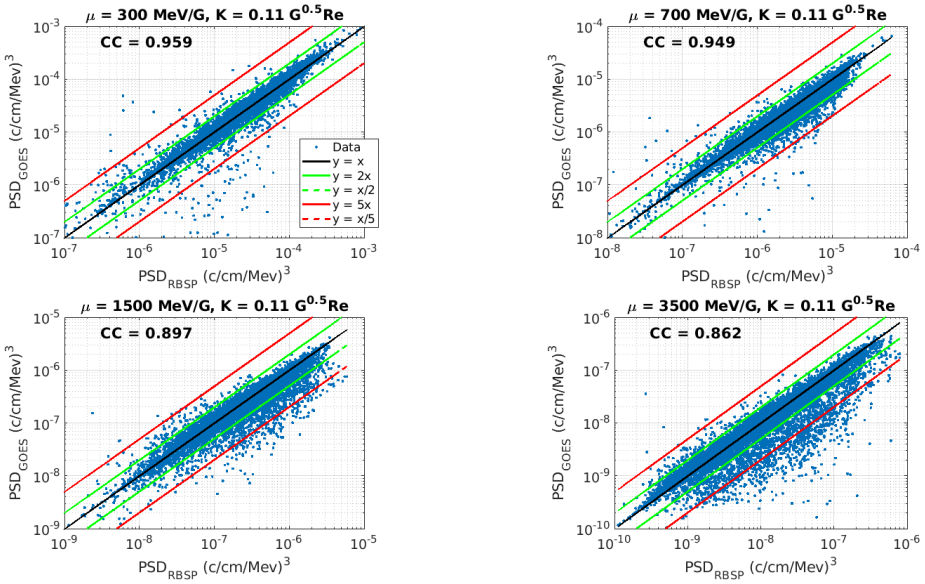

FIGURE 6.3: Comparison of PSD derived from Van Allen Probes and GOES measurements between 01 October 2012 and 01 October 2016 and within 0.2 R_E of each other, for the specified pairs of adiabatic invariants. Green lines indicate data within a factor of 2, and red, within a factor of 5.

towards a more accurate assessment of the errors of different missions and instruments, as a function of energy and pitch angle, will be performed and incorporated into the data assimilative framework.

In contrast to previous studies (e.g. Ni et al., 2009; Kellerman et al., 2014), who intercalibrated spacecraft data prior to their assimilation into the VERB code, such a procedure between the Van Allen Probes A and B and GOES 13 and 15 was not necessary in this work. Figure 6.3 shows, for four values of the first two adiabatic invariants (which are later investigated in Chapter 8), PSD calculated hourly from Van Allen Probes and GOES measurements taken between 01 October 2012 and 01 October 2016, and located within 0.2 R_E of each other. The correlation coefficient is also shown for each case, as well as green and red lines bounding data within a factor of 2 and 5, respectively. Table 6.3 quantifies the results from Figure 6.3 and presents the total number of PSD hourly values within 0.2 R_E, and the percentage of them falling between a factor of 2 and 5. The scatter plots from Figure 6.3, as well as the large correlation coefficients (> 0.85) and the percentage of PSD derived values located within a factor of 2 ($> 89\%$), show the good agreement between PSD calculated from Van Allen Probes and GOES measured fluxes. Therefore, there was no need to perform satellite intercalibration in this study.

6.3 Data Assimilation in Radiation Belt Modelling

Naehr and Toffoletto (2005) were among the first to demonstrate the applicability of data assimilation to radiation belt research, by performing identical twin experiments with a radial diffusion model and synthetic observational data. Kondrashov et al. (2007) used the EKF to estimate the electron PSD and to infer unknown parameters in a model, such as the relativistic electron lifetimes in the Earth's radiation belts. Shprits et al. (2007) and Koller et al. (2007) performed data assimilation with a radial diffusion model and demonstrated how it can be used to identify and adjust

TABLE 6.3: Statistics of PSD hourly values derived from Van Allen Probes and GOES measurements between 01 October 2012 and 01 October 2016 and within 0.2 R_E of each other, for the specified pairs of adiabatic invariants.

	$\mu = 300$ MeV/G	$\mu = 700$ MeV/G	$\mu = 1500$ MeV/G	$\mu = 3500$ MeV/G
number of PSD hourly values within 0.2 R_E	16534	13781	13579	13942
% within a factor of 2	97.54	95.59	90.8	89.88
% within a factor of 5	99.3	99.3	97.84	95.96

for missing physics in the model. They also showed that the KF added PSD between $L^* = 5$ and $L^* = 6$, which is consistent with local acceleration driven by chorus waves (see Section 3.3.1.2).

Furthermore, Ni et al. (2009) used four empirical external magnetic field models, along with simultaneous sparse but calibrated observations of four satellites, and found that combined reanalysis are relatively insensitive to the choice of magnetic field model. The results also showed that the errors of PSD obtained by assimilating multiple satellite measurements at different locations can be smaller than the errors of individual satellite reconstructions. Daae et al. (2011) tested the sensitivity of the reanalysis of radiation belt PSD to the assumed outer boundary conditions and loss model, and demonstrated that the KF performs remarkably well when sufficient data is available at all considered L shells for the assimilation. They also found out that the effect of the initial condition is negligible after one day of simulations as long as data are available. Kondrashov, Ghil, and Shprits (2011) proposed a modified filter in log-normal space that significantly improved the PSD reanalysis and prediction skill compared to the KF formulation.

Shprits, Daae, and Ni (2012) performed a long-term multispacecraft reanalysis and found a good correlation between the location of the peak of the PSD and the plasmapause location, and investigated the link between PSD dropouts and solar wind dynamic pressure increases (see Section 3.3.2). Schiller et al. (2012) also used a Kalman filter in combination with a five satellite data set and a radial diffusion model, and augmented the filter to include local acceleration in the state vector. Their study concluded that the local source is a major contributor to the outer radiation belt in the recovery phase. Ni et al. (2013b) further studied the occurrence of PSD dropouts in terms of solar wind dynamic pressure pulses and increases by reconstructing the entire year 2002 radial profiles of PSD, and found results consistent with those of Shprits, Daae, and Ni (2012). The results also showed that the errors of PSD obtained by assimilating multiple satellite measurements at different locations can be smaller than the errors of individual satellite reconstructions.

Several recent studies have employed 3D diffusion models accounting for radial, pitch-angle, and energy diffusion (e.g., Bourdarie and Maget, 2012; Kellerman et al., 2014; Cervantes et al., 2020a; Cervantes et al., 2020b). Such 3D models potentially account for more physical processes and use the knowledge of the dynamics of pitch-angle distributions and energy spectra. Moreover, as mentioned in the previous section, Shprits et al. (2013a) suggested an operator splitting method that allowed to use the KF for 3D diffusion codes.

Chapter 7

Identifying Sources and Losses in the Outer Radiation Belt

The results of this chapter have been published in the *Journal of Geophysical Research: Space Physics* as:

Cervantes, S., Shprits, Y. Y., Aseev, N. A., Drozdov, A. Y., Castillo, A., and Stolle, C. (2020) *Identifying radiation belt electron source and loss processes by assimilating spacecraft data in a three-dimensional diffusion model. Journal of Geophysical Research: Space Physics,* 125, e2019JA027514. https://doi.org/10.1029/2019JA027514

The presented analysis is the outcome of the author's own work. Y. Y. Shprits, N. A. Aseev, A .Y. Drozdov, A. Castillo, and C. Stolle provided supervision and/or advice. The results from this chapter were presented at the 2018 GEM Summer Workshop in Santa Fe, the 2018 AGU Fall Meeting in Washington, and the 2019 EGU General Assembly in Vienna.

7.1 Overview

As mentioned in Chapter 3, the dynamics of the outer radiation belt is governed by a complex competition between a number of physical processes, including transport, acceleration, and loss (e.g. Friedel, Reeves, and Obara, 2002; Shprits et al., 2008; Millan and Baker, 2012; Turner et al., 2014a). High resolution profiles of PSD in both time and space are essential to differentiate between these mechanisms and to quantify their relative roles. Moreover, knowledge of the outer belt dynamics is of particular importance since it spatially overlaps with many communication and scientific spacecraft orbits, as depicted in Figure 2.14. Understanding the mechanisms responsible for the dynamics of radiation belt electrons is essential for predicting the response of the radiation belts to geomagnetic disturbances.

However, as pointed out in Section 6.1, restrictions of spacecraft observations to a single or a few measurements in time and space, and at specific values of electron energy and pitch angle, hinder the calculation of such PSD profiles. This limitation is compounded by the inaccuracy of the instruments. Data assimilation provides algorithms to fill the gaps in data using physics-based models in an optimal way, and hence to reconstruct the radial profiles of PSD, while keeping consistency between model dynamics and observations. This novel approach has become an increasingly useful and popular tool for improving our understanding of radiation belt dynamics.

Data assimilation has proven to be an effective method in radiation belt modelling as it can also provide the best possible estimate of the current state of the

system. This estimate, in turn, can be employed as an accurate initial condition for forecasting models, and therefore, can improve their prediction skill. Spacecraft operators, who are interested in knowing the radiation levels for particular orbits where there is no monitoring of radiation, can benefit from data assimilation as well. The assimilated state can be used, for instance, to determine whether a specific satellite failure has been due to an increase of radiation or not.

The purpose of this chapter is to incorporate the following processes into the VERB-3D data assimilation scheme, absent in previous studies: mixed pitch angle-energy diffusion, scattering by EMIC waves, and magnetopause shadowing. Their relevance to the radiation belt dynamics has been evaluated in earlier works, based either on observations or model simulations (e.g., Albert and Young, 2005; Shprits et al., 2006c; Shprits et al., 2008; Albert, Meredith, and Horne, 2009; Subbotin, Shprits, and Ni, 2010; Xiao et al., 2010; Turner et al., 2012a; Shprits et al., 2013b; Yu, Koller, and Morley, 2013; Turner et al., 2014a; Turner et al., 2014b; Usanova et al., 2014; Drozdov et al., 2015; Shprits et al., 2016; Drozdov et al., 2017; Shprits et al., 2017; Xiang et al., 2017). However, their effect on the reanalysis has not yet been investigated and objectively quantified.

7.2 Methodology

The data assimilative framework employed in this work combines the VERB-3D code with data from the Van Allen Probes A and B (Section 5.1) and GOES 13 and 15 (Section 5.2) on the basis of a split-operator KF as outlined in Section 6.2. The date range spans from 01 October 2012 to 01 April 2013. The VERB-3D model setup, namely boundary and initial conditions, computational grid, and radial, pitch angle, energy, and mixed pitch angle-energy diffusion coefficients, are as described in Section 4.2.

Multiple reanalysis are performed by systematically adding, one by one, the above-mentioned processes. The innovation vector is inspected for each reanalysis and for various values of the adiabatic invariants μ and K. This measure is interpreted as an evidence of the effect of these mechanisms in the dynamics of the radiation belt electrons. Furthermore, the radial distance from the Earth and the geomagnetic conditions under which each physical process operates are also identified by means of the innovation vector.

In total, four data assimilation runs are performed, as summarised in Table 7.1. The first one only accounts for radial diffusion due to ULF waves, and for pitch-angle and energy diffusion due to chorus and hiss waves (hereinafter, 3D diffusion), neglecting mixed pitch angle-energy diffusion, EMIC wave scattering, and losses due to magnetopause shadowing. In the other three runs, one process is systematically added at a time with respect to the previous run. In the second reanalysis, mixed pitch angle-energy diffusion is incorporated; in the third one, scattering by EMIC waves; and in the last one, magnetopause shadowing.

7.3 Reanalysis of Electron PSD from 01 October 2012 to 01 April 2013

The results of this chapter focus on the evolution of PSD for two sets of three pairs of the adiabatic invariants μ and K, yielding six pairs in total. For the first set, the invariant K is equal to 0.8 $G^{0.5}R_E$, with the following three different values of μ:

TABLE 7.1: Summary of six-month data assimilation runs.

Run	Processes included
1	Radial diffusion due to ULF waves + pitch-angle and energy diffusion due to chorus and hiss waves (3D diffusion)
2	3D diffusion + mixed pitch angle-energy diffusion due to chorus and hiss waves
3	3D diffusion + mixed pitch angle-energy diffusion due to chorus and hiss waves + EMIC wave scattering
4	3D diffusion + mixed pitch angle-energy diffusion due to chorus and hiss waves + EMIC wave scattering + magnetopause shadowing

50 MeV/G, 300 MeV/G, and 600 MeV/G. For the second set, the invariant K equals 0.1 $G^{0.5}R_E$, with the following three different values of μ: 200 MeV/G, 1300 MeV/G, and 2650 MeV/G. Their related equatorial pitch- angle and electron kinetic energy dependencies on the L shell for a dipole magnetic field are plotted in Figure 7.1, using the equations provided in Section 2.2. The pitch angle of the electrons changes only by a few degrees, whereas electrons can lose (gain) a large amount of kinetic energy by radially diffusing outward (inward) by a few L shells.

At the heart of the outer radiation belt, namely $L = 4.5$, for the chosen values of $K = 0.8\ G^{0.5}R_E$ and $K = 0.1\ G^{0.5}R_E$, the equatorial pitch angles are approximately 22^o and 52^o, respectively. At $L = 4.5$ for the pairs ($\mu = 50$ MeV/G, $K = 0.8\ G^{0.5}R_E$) and ($\mu = 200$ MeV/G, $K = 0.1\ G^{0.5}R_E$), electron energies are ~ 0.7 MeV. For the pairs ($\mu = 300$ MeV/G, $K = 0.8\ G^{0.5}R_E$) and ($\mu = 1300$ MeV/G, $K = 0.1\ G^{0.5}R_E$), E is ~ 2.2 MeV, while for the pairs ($\mu = 600$ MeV/G, $K = 0.8\ G^{0.5}R_E$) and ($\mu = 2650$ MeV/G, $K = 0.1\ G^{0.5}R_E$), electron energies are ~ 3.3 MeV, at $L = 4.5$. Such a selection of pairs of adiabatic invariants allows the comparison of three different populations of electrons at low and high equatorial pitch angles, with approximately the same energy variation across the outer radiation belt.

The combined reanalysis based on the VERB-3D code and four satellite measurements, and accounting for 3D diffusion, mixed pitch angle-energy diffusion, EMIC wave scattering, and magnetopause shadowing, are shown in Figures 7.2 and 7.3. From top to bottom, the one-hour averaged electron PSD versus L^* distribution for the four satellites and the assimilated radial profiles of PSD at the above-mentioned pairs of (μ, K) are presented. The last two panels show the solar wind dynamic pressure and the geomagnetic index Kp, respectively. The Van Allen Probes measurements provide the electron PSD below $L^* = 5.8$, and the GOES measurements above $L^* \sim 6$, establishing a good radial coverage of observed PSD. Although the data clearly show a number of electron dropouts and enhancements, the distribution is still sparse in space and time. After blending the observations with the VERB-3D code, the gaps are filled, as illustrated in panels (b), (d), and (f).

The temporal evolution of the assimilated PSD is strongly correlated with the geomagnetic activity as shown in Figures 7.2 and 7.3. In accordance with previous reanalysis studies (e.g. Ni et al., 2009; Shprits, Daae, and Ni, 2012; Ni et al., 2013b), sudden and substantial dropouts in PSD are observed during the main phase of geomagnetic storms, depleting electron PSD even down to $L^* = 4.6$, as on 17 March 2013, and lasting a few hours. These decreases occur right after sudden pulses of solar wind dynamic pressure, which are in turn associated with clear and pronounced

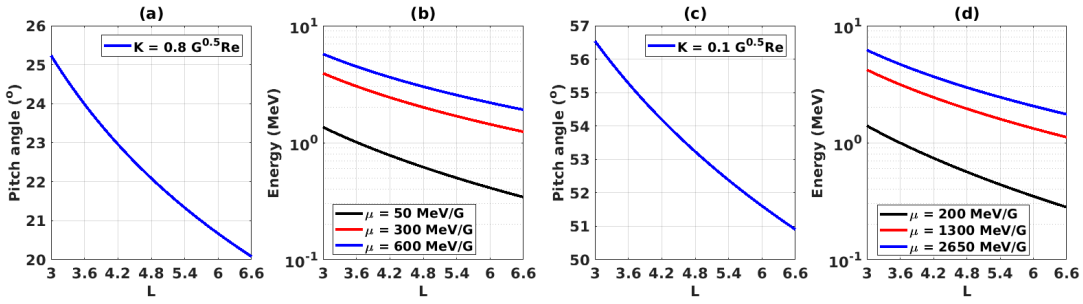

FIGURE 7.1: Dependence of ((a) and (c)) equatorial pitch angle, and ((b) and (d)) electron kinetic energy on L shell in a dipolar magnetic field, for the six pairs of (μ, K) investigated in the present chapter.

compressions of the magnetopause. For example, on 17 January 2013 the solar wind dynamic pressure increased up to 14.8 nPa, and the LCDS moved inward down to $L^* = 5.2$, well below GEO.

In addition, the dependence on energy of the magnetopause shadowing loss mechanism employed in the model is evident when comparing panels (b), (d) and (f) of Figures 7.2 and 7.3. The loss effect is more pronounced at higher values of the invariant μ (lowermost reanalysis, panel (f)), where electron PSD is depleted faster than for lower values of μ (uppermost reanalysis, panel (b)).

7.4 Analysis of the Innovation Vector

As mentioned in Section 6.2.1, the innovation vector adds or subtracts PSD from the predicted values, and it can be regarded as an indicator of the missing electron loss and source processes in the model. Shprits et al. (2007), Koller et al. (2007), and Daae et al. (2011) used it as a tool to understand the physical mechanisms responsible for the acceleration of electrons and interpreted its peaks as evidence of local acceleration, absent in the 1D model employed in their studies.

To objectively investigate the effect of introducing several processes in the VERB-3D model, the hourly innovation vector is calculated for each L^* and binned according to the Kp index. Then, the average innovation vector is computed as a function of L^* and Kp for each of the four six-month runs and each of the six pairs of adiabatic invariants. The distribution of the number of measurements that are used for the reanalysis in terms of Kp is shown in Figure 7.4. Owing to the highly skewed distribution of samples towards low values of Kp, and the lack of measurements at high Kp and L^*, the analysis of the innovation vector is restricted in this chapter to the intervals with $Kp < 4$.

7.4.1 Average Innovation for PSD at K = 0.8 $G^{0.5}R_E$ and Different Values of the Invariant μ

For the electrons with $\mu = 50$ MeV/G (Figure 7.5, first row), the average innovation using the model with 3D diffusion shows enhanced overestimation of PSD extending from $L^* = 4.4$ to $L^* = 6.6$ for $Kp > 2$, and for $Kp < 2$ between $L^* = 5$ and $L^* = 5.6$. The addition of mixed pitch angle-energy diffusion significantly reduces this overestimation, and furthermore, it emphasises a region of underestimation of PSD at large radial distances, extending from $L^* = 5.6$ to the outer boundary. The inclusion of EMIC waves does not change the average innovation vector, as the

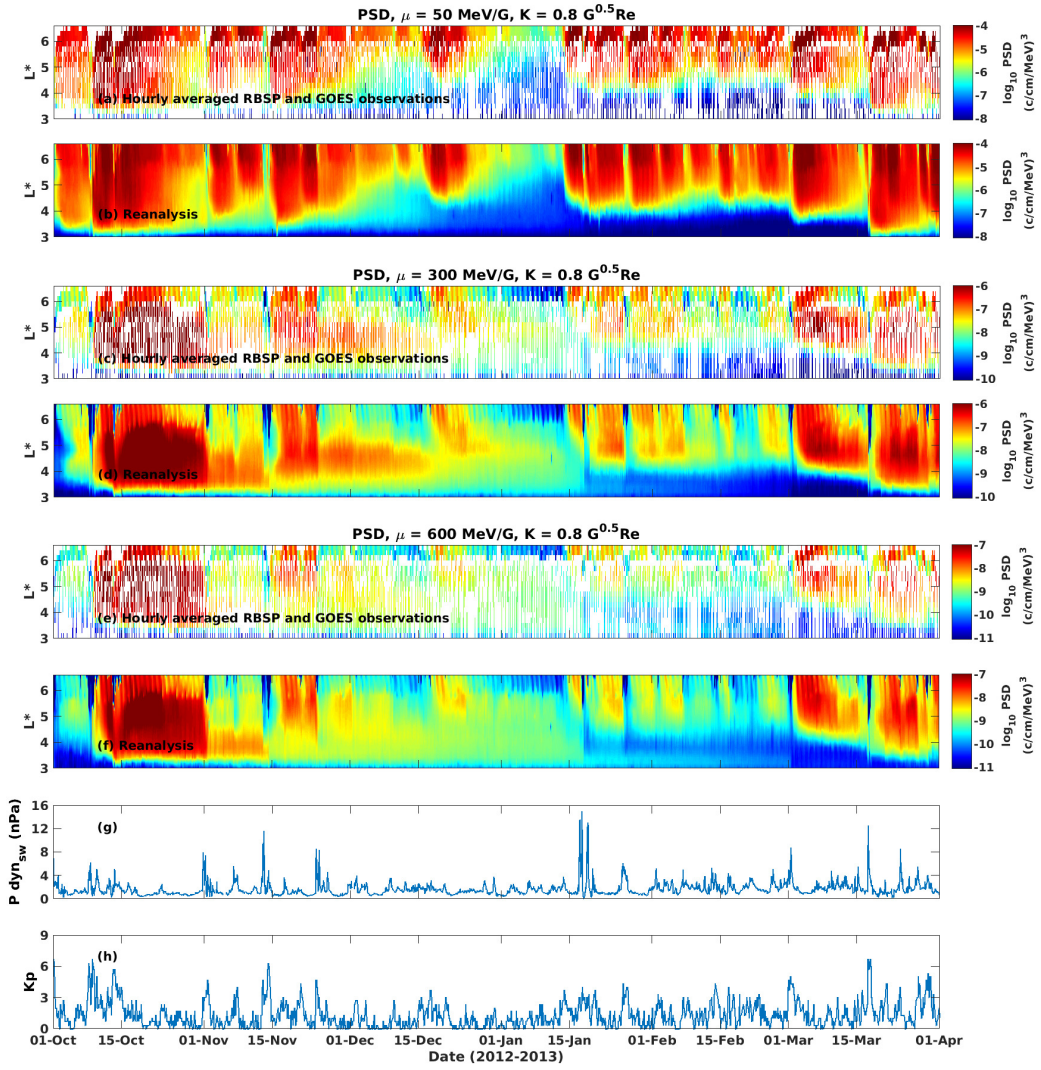

FIGURE 7.2: Evolution of electron PSD as a function of L^* and time from 01 October 2012 to 01 April 2013: (a) Van Allen Probes and GOES data, and (b) assimilated radial profile of PSD for $\mu = 50$ MeV/G and $K = 0.8$ $G^{0.5}R_E$; (c) and (d) same as (a) and (b) but for $\mu = 300$ MeV/G and $K = 0.8$ $G^{0.5}R_E$; (e) and (f) same as (a) and (b) but for $\mu = 600$ MeV/G and $K = 0.8$ $G^{0.5}R_E$; (g) evolution of solar wind dynamic pressure, and (h) geomagnetic activity Kp index. The assimilative results of the combined reanalysis of electron PSD in this figure account for 3D diffusion, mixed pitch angle-energy diffusion, scattering by EMIC waves, and magnetopause shadowing.

lower-energy electrons (≤ 1 MeV) are in general unaffected by them (e.g. Horne and Thorne, 1998; Meredith et al., 2003c). Lastly, incorporating magnetopause shadowing driven by the LCDS accentuates a region of large innovation at $L^* > 5.8$ for $Kp > 2$. This is indicative of a missing source in the radiation belt model, namely, earthward magnetospheric convection of electrons with keV energies from the tail region to the plasmasheet.

The average innovation vector of the 3D reanalysis of the electrons with $\mu = 300$ MeV/G (Figure 7.5, second row) exhibits a region of large overestimation of PSD at all L^* for $Kp > 2+$. Such missing loss is then added when mixed pitch angle-energy diffusion is incorporated into the scheme, in particular at $L^* < 5.8$.

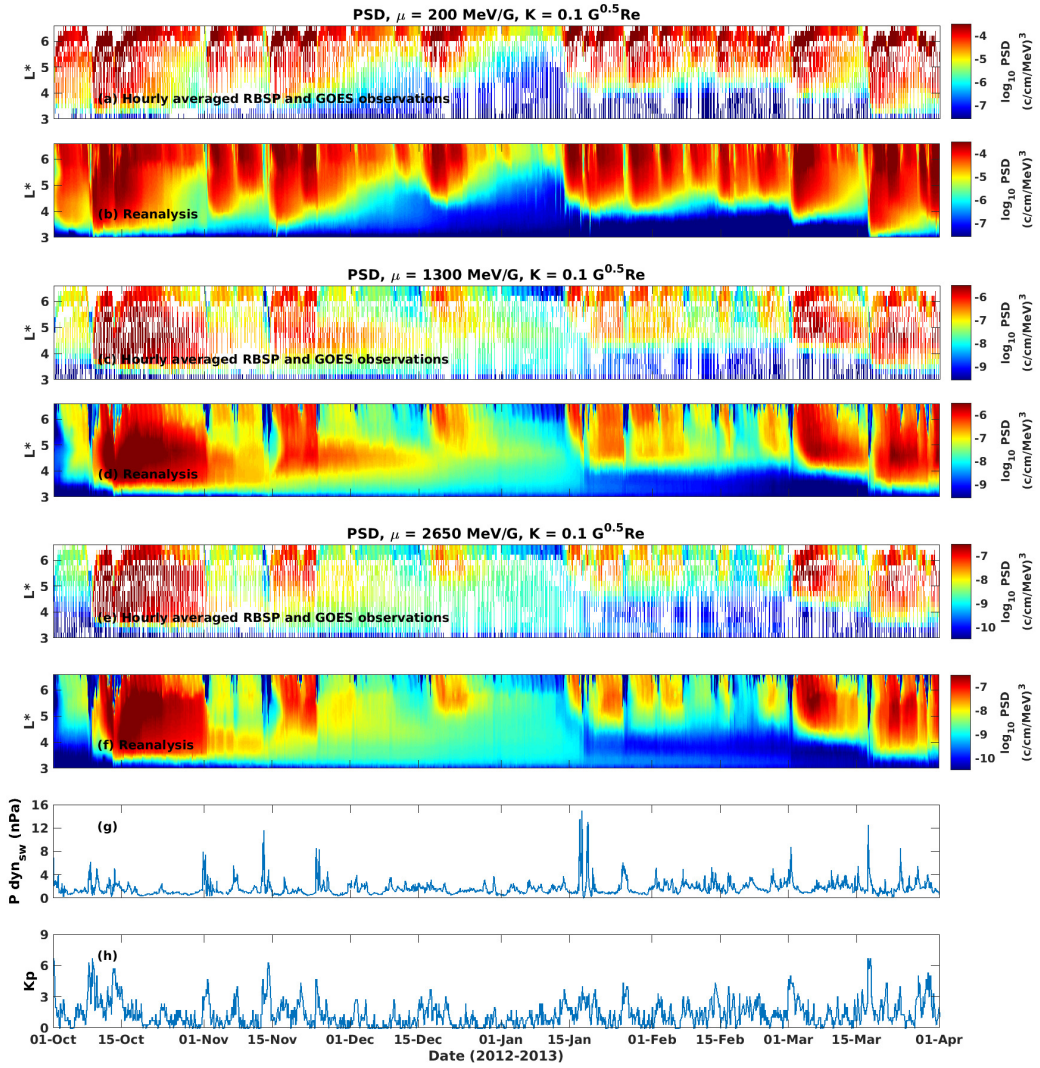

FIGURE 7.3: Same as Figure 7.2, but for the pairs of invariants ((a) and (b)) $\mu = 200$ MeV/G and $K = 0.1$ $G^{0.5}R_E$; ((c) and (d)) $\mu = 1300$ MeV/G and $K = 0.1$ $G^{0.5}R_E$; and ((e) and (f)) $\mu = 2650$ MeV/G and $K = 0.1$ $G^{0.5}R_E$.

Furthermore, scattering by EMIC waves effectively brings loss into the model, as the average innovation vector decreases for $L^* < 5.6$ and $Kp > 3$, which for this population of electrons corresponds to energies greater than 1.9 MeV. The effect of EMIC waves is only observed close to the plasmapause and is negligible below 1.9 MeV. The innovation, when magnetopause shadowing and outward diffusion induced by it are included, acts as a loss process, especially for $Kp > 3$ and $L^* > 5.6$.

Finally, for the electrons with first invariant $\mu = 600$ MeV/G (Figure 7.5, third row), the PSD is largely overestimated when relying only on the 3D model, hence the KF substracts PSD, particularly in the region extending from $Kp = 2$ to $Kp = 4$ at all L^*. The addition of both mixed pitch angle-energy diffusion and EMIC wave scattering acts as a loss process, mostly for $Kp > 2$ and $L^* < 5.8$, where the energy of electrons is larger than 2.2 MeV. Moreover, taking into account magnetopause shadowing reduces to some extent the overestimation of electron PSD at $L^* > 5.6$ and $Kp > 3$.

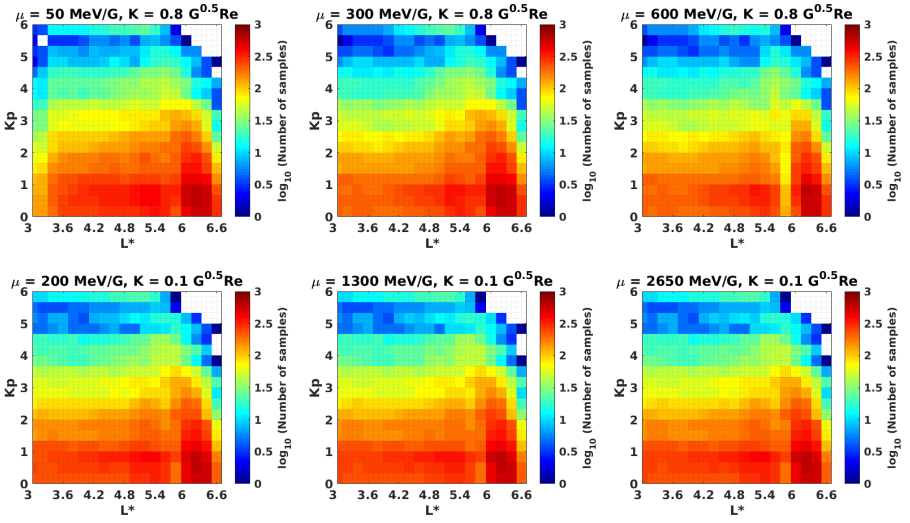

FIGURE 7.4: Distribution of the number of samples employed in the reanalysis of PSD binned in L^* and Kp for the indicated pairs of adiabatic invariants μ and K.

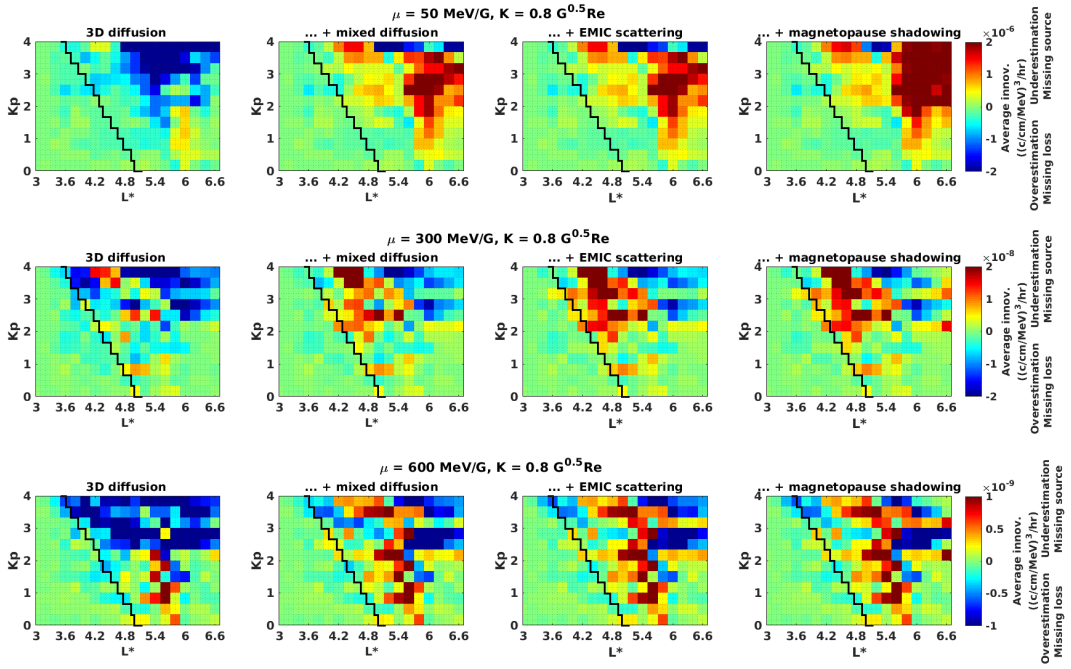

FIGURE 7.5: Innovation vector averaged over the interval 01 October 2012 to 01 April 2013 as function of L^* and Kp for electron PSD for the following pairs of invariants: $\mu = 50$ MeV/G and $K = 0.8$ $G^{0.5}R_E$ (first row), $\mu = 300$ MeV/G and $K = 0.8$ $G^{0.5}R_E$ (second row), and $\mu = 600$ MeV/G and $K = 0.8$ $G^{0.5}R_E$ (third row). The first column corresponds to radial, pitch-angle and energy diffusion (3D) reanalysis, the second to reanalysis with the addition of mixed pitch angle - energy diffusion, the third to reanalysis including scattering by EMIC waves, and the last to reanalysis adding magnetopause shadowing. The solid black line indicates the estimated average location of the plasmapause, computed following Carpenter and Anderson (1992).

7.4.2 Average Innovation for PSD at K = 0.1 $G^{0.5}R_E$ and Different Values of the Invariant μ

For the 3D reanalysis of the electrons with $\mu = 200$ MeV/G (Figure 7.6, first row), the average innovation vector shows how the model accounting only for 3D diffusion significantly overestimates PSD. As a result, the KF subtracts PSD between $L^* = 4.6$ and $L^* = 6.6$ for $Kp > 2+$, and from $L^* = 4.8$ to $L^* = 6.2$ for quieter geomagnetic conditions. Such a missing loss process is added when mixed pitch angle-energy diffusion is incorporated into the framework, particularly for $L^* < 6$. Due to the low energy of this population of electrons, the inclusion of EMIC wave scattering does not modify the average innovation vector. Moreover, considering magnetopause shadowing shows that a missing source process (magnetospheric convection) is operating between $L^* = 5.6$ and $L^* = 6.6$, similarly to the case with $\mu = 50$ MeV/G and $K = 0.8$ $G^{0.5}R_E$.

The average innovation of the electrons with $\mu = 1300$ MeV/G (Figure 7.6, second row) shows that for $L^* > 5$ and all geomagnetic conditions, PSD is overestimated by the 3D model. However, introducing mixed pitch angle-energy diffusion does not significantly affect this population. The addition of scattering by EMIC waves corrects for the PSD overestimation in the region between $Kp = 3$ and $Kp = 4$ for $L^* < 4.4$, where the energy of the electrons is greater than 2.3 MeV. Considering magnetopause shadowing brings further losses into the model, in particular for $Kp > 2$ and $L^* > 5.4$.

Lastly, the innovation of the 3D reanalysis of the electrons with $\mu = 2650$ MeV/G (Figure 7.6, third row) shows, on average, a region of overestimation at $L^* > 5.8$ for $Kp > 2$, and for $Kp > 3-$ at $L^* < 5.2$. For this population, mixed pitch angle-energy diffusion does not introduce losses as was the case for the electrons with $K = 0.8$ $G^{0.5}R_E$. In contrast, EMIC wave scattering effectively decreases PSD for $Kp > 2+$ and $L^* < 5.6$, where electrons have energies larger than 2.3 MeV, and magnetopause shadowing partially removes PSD at $L^* > 5.4$ and $Kp > 2+$.

7.5 Discussion and Conclusions

Data assimilation by means of a standard KF fills in the spatial and temporal gaps left by sparse in-situ measurements, combines them with the VERB-3D model, and as result, reconstructs electron PSD. In comparison to previous works, these results potentially account for more physical loss processes, and in the future, will improve our understanding of the dynamic evolution of radial profiles of PSD. Data assimilation can also be applied to identify time intervals where the model predictions are significantly lower or higher than the observations. In this regard, the innovation vector is used to pinpoint which mechanisms are absent in the model, where they operate, and which population of electrons they affect the most.

Mixed pitch angle-energy diffusion subtracts PSD from the model, and its effect is stronger at higher K (Section 7.4.1), than at lower K (Section 7.4.2). Similar results have been reported by others (e.g., Albert and Young, 2005; Albert, Meredith, and Horne, 2009; Subbotin, Shprits, and Ni, 2010; Xiao et al., 2010) relying on 2D (pitch-angle and energy diffusion) and 3D simulations. The contribution of mixed pitch angle-energy diffusion at low K and high μ (last two cases in Section 7.4.2) warrants a more detailed study in the future.

The scattering effect induced by EMIC waves on electrons with energies above ~ 2 MeV and equatorial pitch angles less than $\sim 40^o$ to 60^o (both second and third

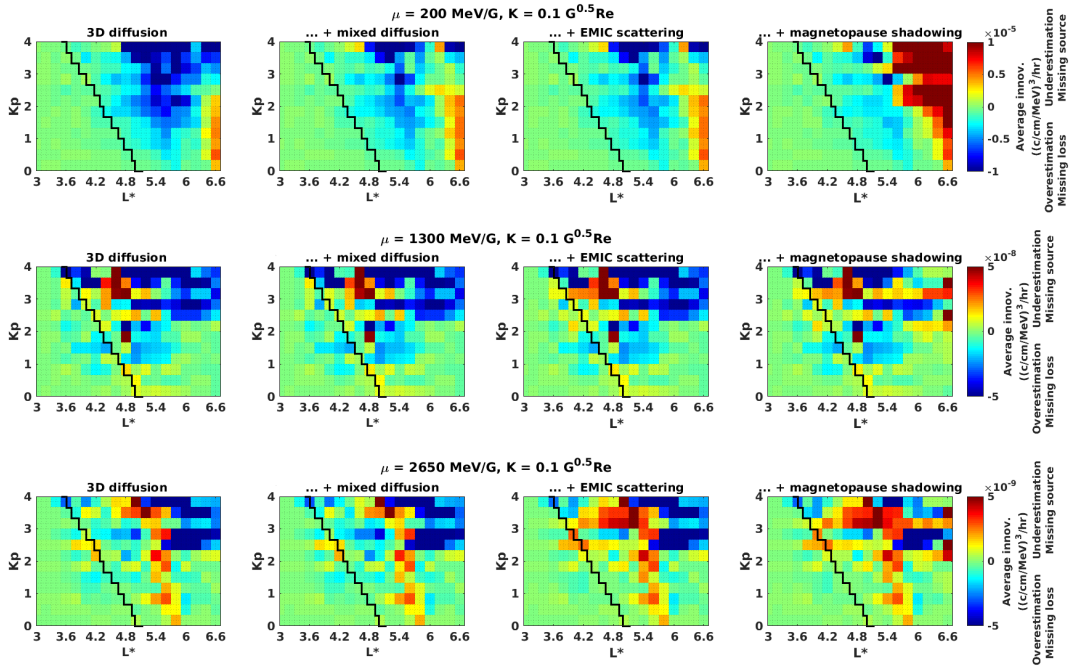

FIGURE 7.6: Same as Figure 7.5, for the pairs of invariants $\mu = 200$ MeV/G and $K = 0.1$ $G^{0.5}R_E$ (first row), $\mu = 1300$ MeV/G and $K = 0.1$ $G^{0.5}R_E$ (second row), and $\mu = 2650$ MeV/G and $K = 0.1$ $G^{0.5}R_E$ (third row).

cases in Sections 7.4.1 and 7.4.2) is consistent with previous modelling and observational studies (e.g., Shprits et al., 2013b; Shprits et al., 2016; Drozdov et al., 2017; Xiang et al., 2017). Visual analysis of the corresponding average innovation plots, before and after including EMIC waves for 300 MeV/G and $K = 0.8\,G^{0.5}$ R_E, and for 600 MeV/G and $K = 0.8\,G^{0.5}$ R_E, show that, for a fixed K, the loss brought by introducing EMIC waves, is larger for higher μ than for lower μ. Similar effects are observed for $K = 0.1\,G^{0.5}$ R_E. Specifically, such loss is mostly evident in the region with $2 < Kp < 4$ and $L^* < 5$, on average. These findings provide supporting evidence that EMIC waves provide an additional loss mechanism and play an essential role in the dynamics of the ultrarelativistic electron population.

Magnetopause shadowing driven by the LCDS effectively brings losses into the model, as concluded by earlier studies which relied either on observations or simulations (e.g., Shprits et al., 2006c; Turner et al., 2012a; Yu, Koller, and Morley, 2013; Turner et al., 2014b; Xiang et al., 2017). The average innovation plots show that this mechanism is more efficient in the intervals with $2 < Kp < 4$ and in the region with $L^* > 5$. For the two populations of electrons with the lowest μ values (both first cases in Sections 7.4.1 and 7.4.2), the incorporation of this process into the data assimilative scheme clearly illustrates a region of large underestimation extending from $L^* = 5.4$ up to the boundary at $L^* = 6.6$, corresponding to the absence of magnetospheric convection in the reanalysis. Such a process is accounted for by other models, e.g. the VERB-4D code (Shprits et al., 2015; Aseev et al., 2016), which solves the modified Fokker-Planck equation with additional convection terms.

Chapter 8

Understanding the Loss Mechanisms of Radiation Belt Dropouts

The results of this chapter have been published in the *Journal of Geophysical Research: Space Physics* as:

Cervantes, S., Shprits, Y. Y., Aseev, N. A., and Allison, H. J. (2020) *Quantifying the effects of EMIC wave scattering and magnetopause shadowing in the outer electron radiation belt by means of data assimilation. Journal of Geophysical Research: Space Physics,* 125, e2020JA028208. https://doi.org/10.1029/2020JA028208

The presented analysis is the outcome of the author's own work. Y. Y. Shprits, N. A. Aseev, and H. J. Allison provided supervision and/or advice. The results from this chapter were presented at the 2019 AGU Fall Meeting in San Francisco and the 2020 Virtual GEM Summer Workshop.

The four-year reanalysis of electron PSD has been published as a database in the following form:

Cervantes, S., Shprits Y. Y., Aseev N. A., Drozdov A. Y., Castillo A., and Allison H. J. (2020) *Three-dimensional reconstruction of the dynamic evolution of the Van Allen belts using multiple satellite measurements and a diffusion model. GFZ Data Services,* https://doi.org/10.5880/GFZ.2.8.2020.003

8.1 Overview

The response of the Earth's outer radiation belt to solar activity is highly dynamic (see Chapter 3). Several studies have associated the variability in the responses of the radiation belts to storms to the complex competing nature between acceleration and loss (e.g. Friedel, Reeves, and Obara, 2002; Millan and Thorne, 2007; Shprits et al., 2008; Millan and Baker, 2012). This chapter essentially focuses on the rapid loss of radiation belt electrons.

It is now widely accepted that reductions of the outer radiation belt electron flux can be attributed both to adiabatic and nonadiabatic processes, introduced in Section 3.3.2. One mechanism that falls into this nonadiabatic category is the loss due to pitch-angle scattering via resonant interaction with various types of magnetospheric waves, including whistler mode chorus, plasmaspheric hiss, and EMIC

waves, which leads to electron precipitation to the atmosphere. Another nonadiabatic process is the loss across the magnetopause, called magnetopause shadowing due to increases in solar wind dynamic pressure. Nevertheless, the relative contribution of each physical process to electron flux dropouts still remains a fundamental puzzle.

Multisatellite observations provide a useful means of understanding the dominant loss mechanisms of radiation belt dropouts. For instance, Green et al. (2004) used 52 dropout events and tested several processes that may contribute to electron flux decreases, including adiabatic motion, magnetopause shadowing, and precipitation to the atmosphere. Their study concluded that the most likely cause of the dropout was precipitation to the atmosphere, although the cause of the precipitation remained uncertain. Turner et al. (2012a) analysed data collected by several spacecraft and concluded that the sudden electron depletion on 06 January 2011 was mainly a result of outward radial diffusion rather than loss to the atmosphere.

Boynton, Mourenas, and Balikhin (2016) studied electron flux dropouts on the basis of 20-year measurements from geosynchronous satellites and determined the major solar wind and geomagnetic conditions controlling such dropouts. At energies above 1 MeV, radial diffusion coupled with magnetopause shadowing and precipitation induced by EMIC and chorus (or hiss) waves were found to be effective factors for the observed losses at GEO. In addition, their analysis suggested that at such energies dynamic pressure and southward IMF are the main factors governing the dropouts. In a later study, Boynton, Mourenas, and Balikhin (2017) employed a similar methodology to investigate electron flux dropouts within the heart of the radiation belts at $L \sim 4.2$. In stark contrast with their findings at GEO, the main driving factor for the 1 to 10 MeV electron dropouts at $L \sim 4.2$ turned out to be the southward IMF with no significant influence from solar wind dynamic pressure. This suggests an important role of precipitation loss due to combined EMIC and whistler mode waves in a significant fraction of these events, as well as the existence of different loss mechanisms operating at different L ranges during dropouts. More recently, Xiang et al. (2017) investigated three distinct radiation belt dropouts observed by the Van Allen Probes, subtracting the electron PSD versus L^* profiles before and after the dropout. Their findings suggest that these events can be classified in three different classes in terms of dominant loss processes: magnetopause shadowing dominant, EMIC wave scattering dominant, and a combination of both mechanisms. However, one limitation of in-situ data is the sparse coverage, as incomplete profiles may hinder the calculation of PSD drops.

On the other hand, radiation belt modelling studies have also focused on the importance of loss processes in flux dropouts. For example, Shprits et al. (2006c) explored the viability of outward radial diffusion loss by comparing radial diffusion model simulations with CRRES measurements. The comparison showed that nonadiabatic flux dropouts near GEO can be effectively propagated by the outward radial diffusion down to $L^* = 4$ and that magnetopause loss coupled with the radial transport can account for the main-phase flux dropout. Su et al. (2011) examined the contribution of different loss processes by comparing CRRES observations with a 3D radiation belt model by gradually incorporating magnetopause shadowing, adiabatic transport, radial diffusion, and plume and chorus wave-particle interactions into the code. Yu, Koller, and Morley (2013) quantified the relative contribution of magnetopause shadowing coupled with outward radial diffusion by comparing radial diffusion simulations with GPS-observed total flux dropout. Their results indicated that such process accounted for 60 to 90%/hr of the main-phase radiation belt electron dropout near GEO.

TABLE 8.1: Summary of four-year data assimilation runs.

Run	Processes included
1	Radial diffusion due to ULF waves + pitch-angle, energy, and mixed pitch angle-energy diffusion due to chorus and hiss waves + EMIC wave scattering + magnetopause shadowing ("full" run)
2	Radial diffusion due to ULF waves + pitch-angle, energy, and mixed pitch angle-energy diffusion due to chorus and hiss waves + magnetopause shadowing
3	Radial diffusion due to ULF waves + pitch-angle, energy, and mixed pitch angle-energy diffusion due to chorus and hiss waves + EMIC wave scattering

The aim of this chapter is to answer the question: how much loss is caused by (1) pitch-angle scattering driven by EMIC waves, and (2) magnetopause shadowing? This study tackles this issue by quantifying the contribution of each mechanism via the innovation vector, as derived from the split-operator KF, for several values of the adiabatic invariants μ and K, and for a variety of geomagnetic conditions as described by the indices Kp and Dst and the solar wind dynamic pressure P_{dyn}.

8.2 Methodology

This chapter builds upon the data assimilative algorithm described in Chapter 6 and implemented in Chapter 7. Multiple four-year long-term runs, for the period 01 October 2012 to 01 October 2016 and spanning different levels of geomagnetic activity, are performed by switching on and off in the model the above-mentioned mechanisms.

The results present a four-year statistical analysis of the innovation vector, which is used as a tool to quantify the loss effect of EMIC wave scattering and magnetopause shadowing on radiation belt electrons. For that purpose, three data assimilation runs are performed (Table 8.1). The first run includes all processes in the VERB-3D model (hereinafter, "full" run), and in the second and third runs, one process is neglected in each. The "full" simulation (number 1) accounts for: radial diffusion due to ULF waves, pitch-angle, energy, and mixed pitch angle-energy diffusion due to chorus and hiss waves, EMIC wave scattering, and magnetopause shadowing. The second run (number 2) accounts for all processes except for scattering by EMIC waves. Finally, the third run (number 3) includes all processes in the "full run" with the exception of magnetopause shadowing.

For each of the three runs, the hourly innovation vector $\mathbf{x}_k^i$ is calculated at each L^* and normalised by the corresponding hourly maximum value of assimilated PSD $\mathbf{x}_k^a$ (from the "full" run) over all L^*. Afterwards, the difference between the absolute values of the normalised innovation of the "full" simulation and the one excluding either loss process is calculated according to the following equation:

$$\Delta \mathbf{x}_k^i = \frac{|\mathbf{x}_{1,k}^i| - |\mathbf{x}_{2,k}^i|}{\max(\mathbf{x}_{1,k}^a)} \times 100\%, \tag{8.1}$$

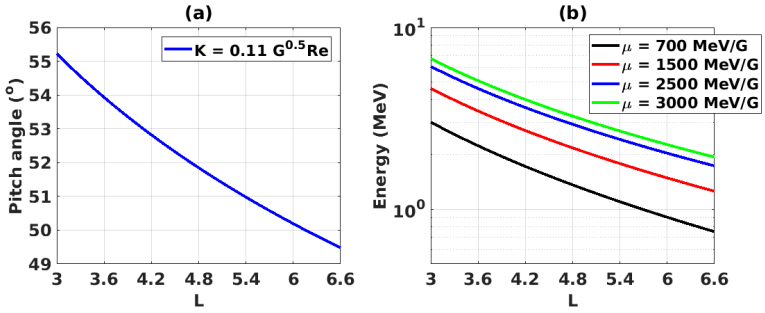

FIGURE 8.1: Dependence of (a) equatorial pitch angle, and (b) electron kinetic energy on L shell in a dipolar magnetic field, for the four pairs of (μ, K) investigated in the present chapter.

where subscript 1 refers to the "full" run and subscript 2 to the run lacking either EMIC wave scattering or magnetopause shadowing. Negative values of $\Delta \mathbf{x}_k^i$ indicate that the inclusion of such mechanisms provides a better agreement with the observed PSD, bringing the model prediction closer to reality. On the other hand, positive $\Delta \mathbf{x}_k^i$ suggests that the modelled effect of either process is stronger than observed, hence the ensuing loss is overestimated. The quantity $\Delta \mathbf{x}_k^i$ is interpreted as an indicator of the loss brought by both scattering by EMIC waves and magnetopause shadowing into the dynamics of the outer radiation belt.

8.3 Long-Term Reanalysis of Electron PSD from 01 October 2012 to 01 October 2016

The reanalysis of PSD and the corresponding innovation vector $\mathbf{x}_k^i$ are inspected in detail for four pairs of adiabatic invariants μ and K. The invariant K is fixed at 0.11 $G^{0.5}R_E$, while μ takes either of the following values: 700 MeV/G, 1500 MeV/G, 2500 MeV/G, and 3000 MeV/G.

The corresponding equatorial pitch angle and electron kinetic energy in a dipolar magnetic field are presented in Figure 8.1. At the heart of the outer radiation belt, for the chosen values of $K = 0.11$ $G^{0.5}R_E$, the equatorial pitch angle is approximately 52^o. Electron energies at $L = 4.5$ are 1.53 MeV for $\mu = 700$ MeV/G, 2.42 MeV for $\mu = 1500$ MeV/G, 3.25 MeV for $\mu = 2500$ MeV/G, and 3.6 MeV for $\mu = 3000$ MeV/G.

Panels (a) and (c) of Figure 8.2 show measured Van Allen Probes and GOES hourly averaged electron PSD at $\mu = 700$ MeV/G and $K = 0.11$ $G^{0.5}R_E$ and $\mu = 3000$ MeV/G and $K = 0.11$ $G^{0.5}R_E$, respectively. The results of the "full" data assimilation run are illustrated in panels (b) and (d). The assimilated PSD is consistent with the original spacecraft data and it indicates the improvement in coverage that reanalysis provides. Panels (e) and (f) depict the solar wind dynamic pressure P_{dyn} and the geomagnetic indices Kp and Dst, respectively.

The reanalysis on panels (b) and (d) exhibits sudden dropouts and buildups of PSD. Figure 8.2 shows that dropouts in PSD often occur in association with sharp increases of solar wind dynamic pressure (e.g. Shprits, Daae, and Ni, 2012; Turner et al., 2012a; Ni et al., 2013b). It is also worth noting that during the first half of the period under study, particularly between October 2013 and October 2014, geomagnetic activity was much weaker and less PSD enhancements were apparent than during 2015 and 2016.

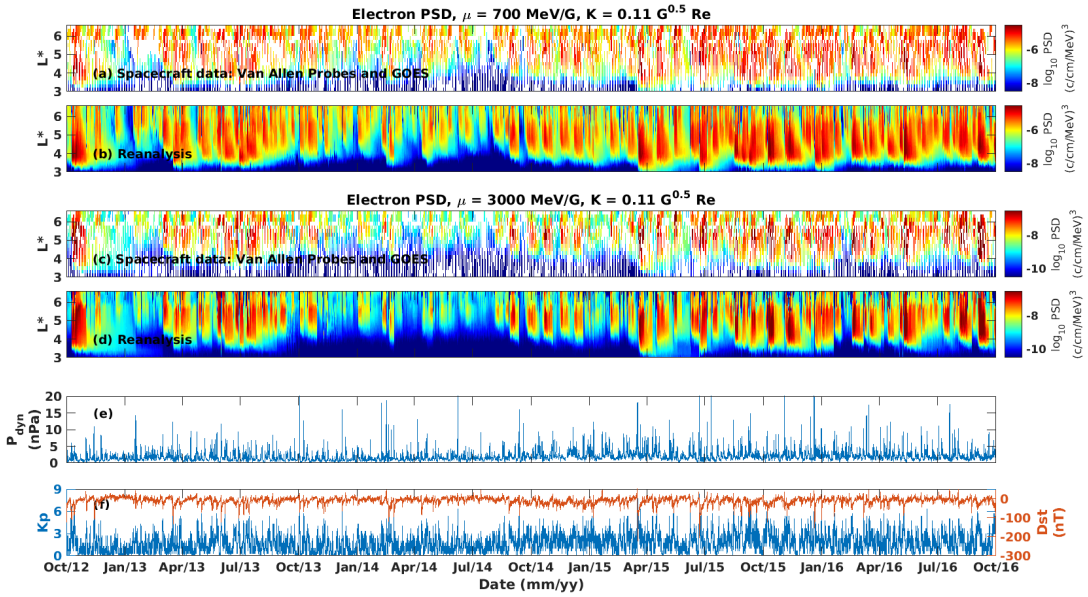

FIGURE 8.2: Evolution of electron PSD as a function of L^* and time from 01 October 2012 to 01 October 2016: (a) Van Allen Probes and GOES data, and (b) assimilated radial profile of PSD for $\mu = 700$ MeV/G and $K = 0.11$ $G^{0.5}R_E$; (c) and (d) same as (a) and (b) but for $\mu = 3000$ MeV/G and $K = 0.11$ $G^{0.5}R_E$; (e) evolution of solar wind dynamic pressure, and (f) geomagnetic activity Kp and Dst indices. The assimilative results of the combined reanalysis of electron PSD in this figure account for 3D diffusion, mixed pitch angle-energy diffusion, scattering by EMIC waves, and magnetopause shadowing (i.e. "full" run).

8.4 Statistical Analysis of Loss Processes by Means of the Innovation Vector

In order to understand the loss due to scattering by EMIC waves and magnetopause shadowing in the outer radiation belt, plots of the normalised innovation $\mathbf{x}^i$ and the difference of normalised innovations $\Delta\mathbf{x}^i$ (equation 8.1) are presented in this section for each four-year run and each of the four chosen pairs of adiabatic invariants. First, the hourly normalised innovation vector is binned according to the Kp index, and the average is computed as a function of L^* and Kp. The same procedure is then followed binning the normalised innovation by solar wind dynamic pressure. Figure 8.3 shows the occurrence of Kp, P_{dyn}, and Dst from 01 October 2012 to 01 October 2016, and the coloured lines indicate different thresholds of geomagnetic activity. The distribution of the number of measurements binned by both Kp and P_{dyn} is plotted in Figures 8.4 and 8.5, respectively. As expected, the distribution of samples is highly skewed towards low values of Kp index and solar wind dynamic pressure.

8.4.1 Scattering by EMIC Waves

The normalised innovation vector $\mathbf{x}^i$ as a function of L^* and Kp, before (run number 2) and after incorporating EMIC waves (run number 1, i.e. "full") into the model, is shown in the first two rows of Figure 8.6. Negative values (blue) denote additional loss missing from the radiation belt model, and thus the KF subtracts PSD in order to compensate and match the observations, i.e. the model overestimates the electron PSD. The last row presents the difference $\Delta\mathbf{x}^i$ as defined by equation 8.1 (namely the second row minus the first row) in which the blue color denotes the area in L^*

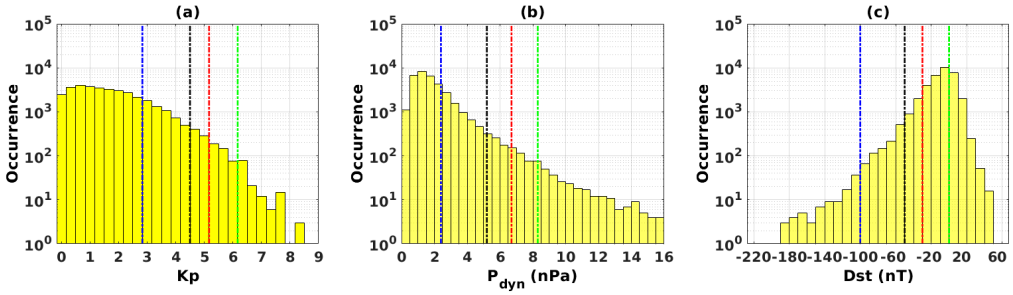

FIGURE 8.3: Occurrence of (a) Kp index, (b) solar wind dynamic pressure P_{dyn}, and (c) Dst index. Note that the y-axes are logarithmic. In plots (a) and (b) the blue, black, red, and green dashed lines denote the 75th, 96th, 98th, and 99th percentiles, respectively. In plot (c) the dashed lines indicate Dst values of -100 nT, -50 nT, -30 nT, and 0 nT. In plot (b) P_{dyn} is binned each 0.5 nPa, and in plot (c) Dst is binned each 10 nT.

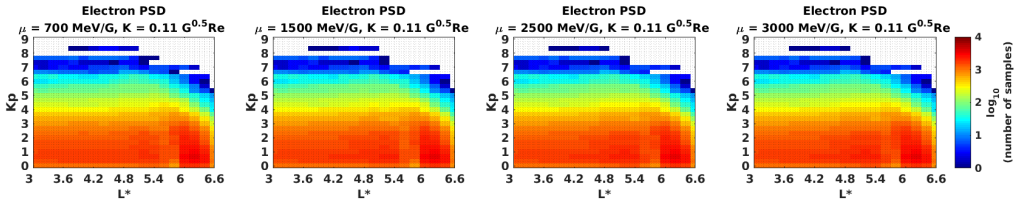

FIGURE 8.4: Distribution of the number of satellite observations employed in the reanalysis of PSD binned by L^* and Kp for the indicated pair of adiabatic invariants μ and K.

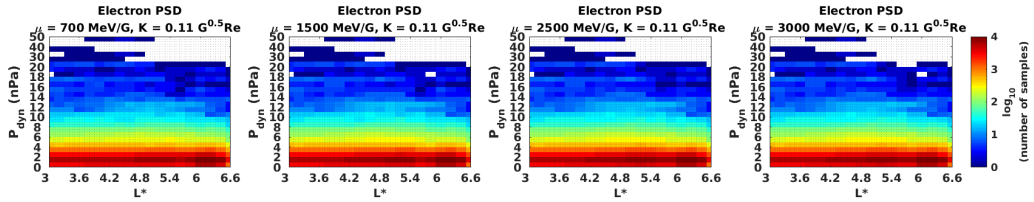

FIGURE 8.5: Distribution of the number of satellite observations employed in the reanalysis of PSD binned by L^* and P_{dyn} for the indicated pair of adiabatic invariants μ and K.

and Kp where EMIC waves operate and effectively scatter electrons. The positive yellow bins correspond to the intervals, mostly during disturbed times, when the inclusion of EMIC waves in the model brings more loss than is observed. This may indicate that the parametrisation based on solar wind dynamic pressure does not always perform well during periods of high geomagnetic activity. The vertical dashed lines delineating the region of EMIC induced scattering loss are drawn considering a threshold of $\Delta \mathbf{x}^i = 10\%/\text{hr}$.

As expected, EMIC waves do not affect the $\mu = 700$ MeV/G population, whereas they have a much more pronounced effect for higher energy electrons (e.g. Shprits et al., 2013b; Kersten et al., 2014; Usanova et al., 2014; Shprits et al., 2016). The upper extent of the region of loss due to EMIC waves moves from $L^* = 4.6$ (for $\mu = 1500$ MeV/G), to $L^* = 5.2$ (for $\mu = 2500$ MeV/G), and further beyond to $L^* = 5.6$ as μ increases to 3000 MeV/G. In terms of Kp, the scattering effect is evident for $Kp \geq 3$. On average, the loss brought by EMIC waves is between 15%/hr and 30%/hr of the maximum PSD, peaking at $Kp \geq 5$ and between $L^* = 4$ and $L^* = 4.8$.

The innovation $\mathbf{x}^i$ and difference of innovations $\Delta \mathbf{x}^i$ are also binned by L^* and P_{dyn} as presented in Figure 8.7. Similar to the results from Figure 8.6, including EMIC

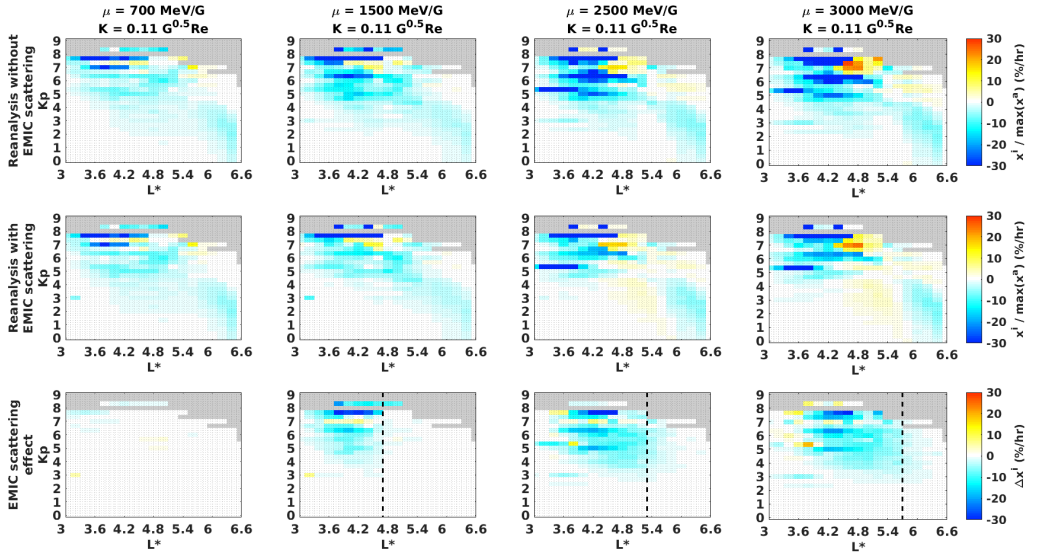

FIGURE 8.6: First row: normalised innovation vector $\mathbf{x}^i$ of the reanalysis without EMIC scattering (run number 2); second row: normalised innovation vector $\mathbf{x}^i$ of the "full" run (number 1); third row: difference of innovations $\Delta\mathbf{x}^i$, where the shaded region limited by the dashed line indicates the area where EMIC scattering is effective. The results are binned by L^* and Kp. Each column indicates a different pair of adiabatic invariants μ and K.

waves in the model decreases the overestimation of PSD, particularly for higher values of μ between $L^* = 4.2$ and $L^* = 5.6$. The scattering effect of these waves is evident for intervals with $P_{\text{dyn}} \geq 2$ nPa, and it exceeds 20% of the maximum PSD for $P_{\text{dyn}} \geq 10$ nPa and $4.2 \leq L^* \leq 4.8$. The choice of binning the innovation by solar wind dynamic pressure follows the previous works from Usanova et al. (2008) and Usanova et al. (2012) (and references therein), which demonstrated that strong magnetospheric compressions associated with high P_{dyn} may drive EMIC waves, and that the occurrence rate of EMIC activity in the dayside outer magnetosphere is controlled to a large extent by solar wind dynamic pressure.

The top row of Figure 8.8 shows the difference, $\Delta\mathbf{x}^i$, across a wide range of the first adiabatic invariant extending from $\mu = 300$ MeV/G ($E = 0.87$ MeV at the heart of the outer belt) to $\mu = 3000$ MeV/G, for both quiet and disturbed geomagnetic conditions as defined by the Kp index. For $Kp \leq 2.7$ (corresponding to the 75th percentile, see the histogram in Figure 8.3) EMIC waves do not contribute to loss. The next three intervals, defined by the 96th, 98th, and 99th percentiles, and characterising active times, show that the effect of these waves is confined to a triangular-shaped region defined by $\mu \geq 900$ MeV/G ($E = 1.78$ MeV at the heart of the outer belt) and extending from $L^* = 3.6$ to $L^* = 6$, on average. The loss brought in by EMIC waves increases from $\sim 10\%$/hr of the maximum PSD for Kp between 4.3 and 5 to $\sim 20\%$/hr for $Kp > 5.7$ (equivalent to the 99th percentile), between $L^* = 4.2$ and $L^* = 4.8$. A similar pattern is observed in the second row of Figure 8.8, where the results are plotted for different intervals of solar wind dynamic pressure. With increasing P_{dyn} and μ, the loss effect due to EMIC waves is enhanced and extends in radial distance from the Earth, maximising between $L^* = 4$ and $L^* = 4.8$.

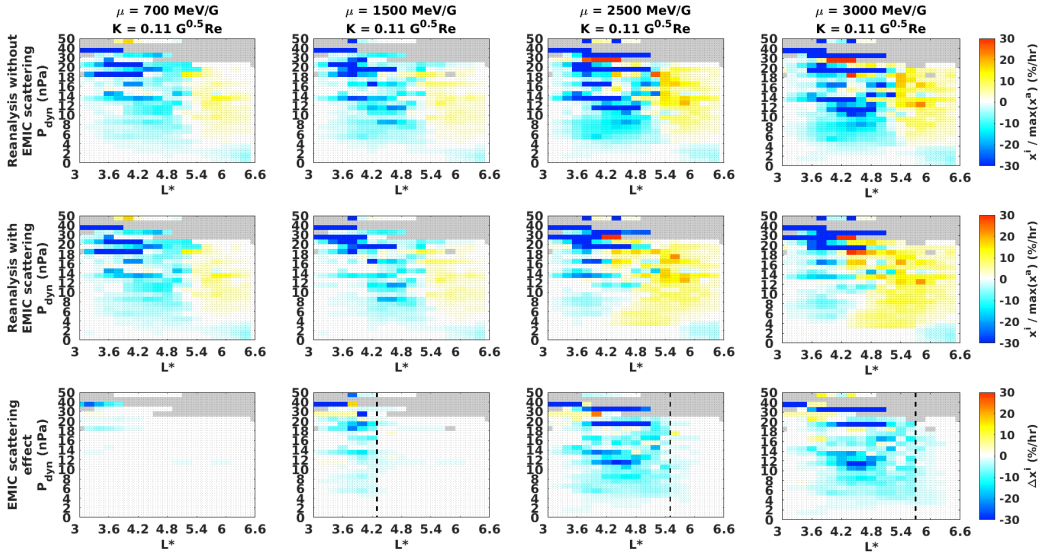

FIGURE 8.7: Same format as Figure 8.6, binning the results by L^* and P_{dyn}. Results are presented in bins of 1 nPa between $P_{\text{dyn}} = 0$ and $P_{\text{dyn}} = 20$ nPa and 5 nPa between $P_{\text{dyn}} = 20$ nPa and $P_{\text{dyn}} = 50$ nPa.

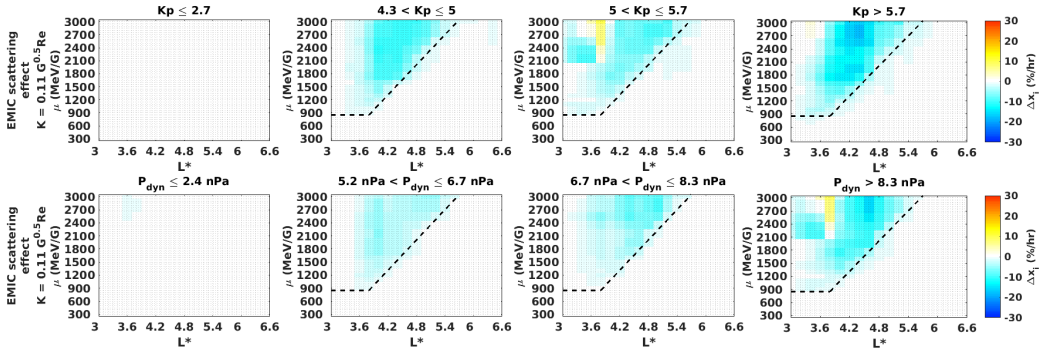

FIGURE 8.8: Difference of innovations $\Delta \mathbf{x}^i$ before and after including EMIC waves in the model for different intervals of geomagnetic activity defined by Kp index (first row) and P_{dyn} (second row) as a function of L^* and μ. The shaded region limited by the dashed line indicates the area where EMIC scattering is effective.

8.4.2 Magnetopause Shadowing

The effect of magnetopause shadowing coupled with outward radial diffusion is inspected in the four-year reanalysis via the difference of innovations $\Delta \mathbf{x}^i$ when including and not including this process (runs number 1 and 3, respectively), binned according to Kp and P_{dyn}. Figure 8.9 shows that loss resulting from magnetopause shadowing extends from the outer boundary for $Kp = 3$ down to $L^* = 3.6$ for $Kp > 7$. Therefore, a statistical picture where the loss region extends to lower L^* at a rate of $\sim 0.75 R_E$ per increase of 1 Kp unit is noticeable. Not surprisingly, the largest values of $\Delta \mathbf{x}^i$, and accordingly, the biggest loss due to magnetopause shadowing ($> 60\%$/hr of the maximum PSD), take place with $Kp \geq 5$ and at $L^* \geq 4.6$. A similar pattern is observed when binning $\Delta \mathbf{x}^i$ by solar wind dynamic pressure (Figure 8.10). Magnetopause loss starts at $P_{\text{dyn}} = 2$ nPa, and it peaks (between 50 and 70%/hr of the maximum PSD) when P_{dyn} exceeds 10 nPa at $L^* \geq 4.8$, on average. In

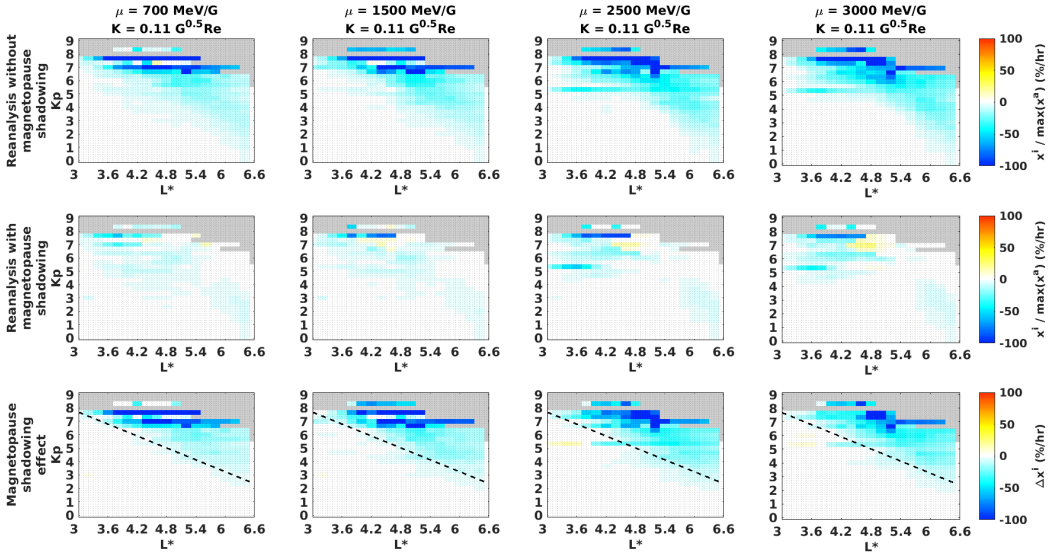

FIGURE 8.9: First row: normalised innovation vector $\mathbf{x}^i$ of the reanalysis without magnetopause shadowing (run number 3); second row: normalised innovation vector $\mathbf{x}^i$ of the "full" run (number 1); third row: difference of innovations $\Delta\mathbf{x}^i$, where the shaded region indicates the region where magnetopause shadowing operates. The results are binned by L^* and Kp. Each column indicates a different pair of adiabatic invariants μ and K.

both figures, the diagonal dashed lines that define the region of loss correspond to a threshold of $\Delta\mathbf{x}^i = 30\%/\text{hr}$.

Figure 8.11 shows that as geomagnetic activity increases from quiet to disturbed times, loss moves inward affecting all values of μ from 300 to 3000 MeV/G. The effect is more pronounced for electrons with values of the invariant $\mu \geq 1500$ MeV/G ($\Delta\mathbf{x}^i$ between 30%/hr and 50%/hr at $L^* \geq 5$) than for those with lower μ ($\Delta\mathbf{x}^i \sim$ 15%/hr, on average), as the former drift faster, and thus, are depleted more quickly than less energetic ones. Likewise, increases in solar wind dynamic pressure also

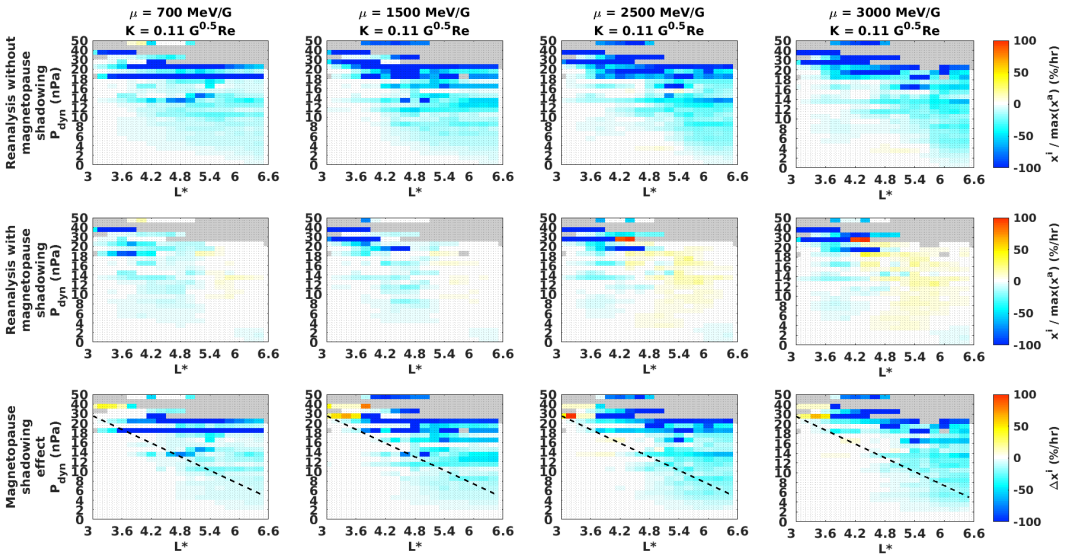

FIGURE 8.10: Same format as Figure 8.9, binning the results by L^* and P_{dyn}.

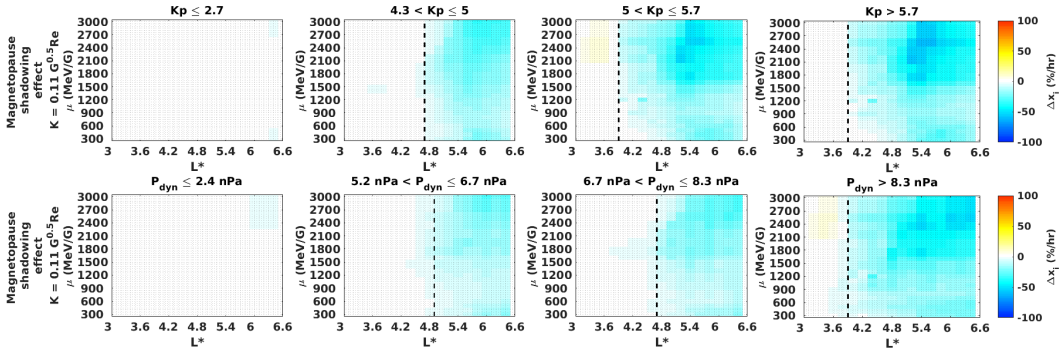

FIGURE 8.11: Difference of innovations $\Delta \mathbf{x}^i$ before and after magnetopause shadowing in the model for different intervals of geomagnetic activity defined by Kp index (first row) and P_{dyn} (second row) as a function of L^* and μ.

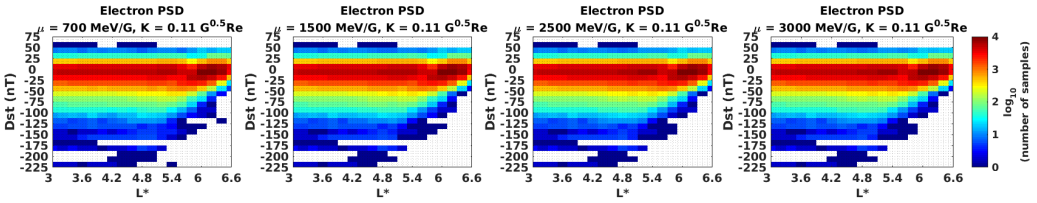

FIGURE 8.12: Distribution of the number of satellite observations employed in the reanalysis of PSD binned in L^* and Dst for the indicated pair of adiabatic invariants μ and K.

move the loss region due to magnetopause shadowing towards low L^*.

Lastly, the results are also analysed by binning $\Delta \mathbf{x}^i$ according to the geomagnetic activity Dst index. The corresponding histogram is shown in the right panel of Figure 8.3, and the distribution of measurements binned by Dst is presented in Figure 8.12. As Figure 8.13 shows, for electrons with $\mu = 700$ MeV/G loss due to magnetopause shadowing exceeds 50%/hr of the maximum PSD for $Dst < -100$ nT, whereas for those with $\mu = 3000$ MeV/G such level of loss is already evident at $Dst = -75$ nT. In other words, as μ increases, less geomagnetic activity, as described by Dst, is required to observe the same percentage loss to the magnetopause. It is also worth noting that, irrespective of the particle's energy, loss due to magnetopause shadowing extends down to $L^* = 4.4$ during times with -100 nT $< Dst \leq -50$ nT and even below to $L^* = 3.6$ when $Dst < -100$ nT.

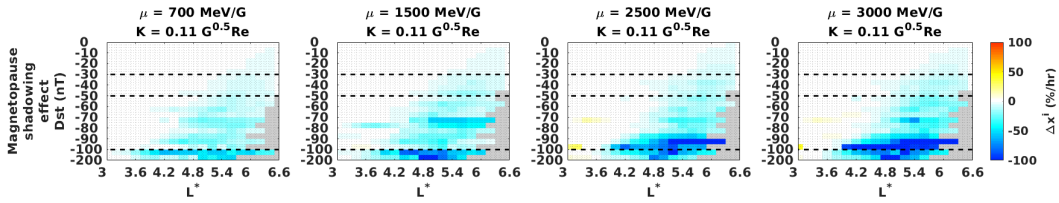

FIGURE 8.13: Difference of innovations $\Delta \mathbf{x}^i$ binned by L^* and Dst. The dashed lines indicate thresholds of -100 nT, -50 nT, and -30 nT. Results are presented in bins of 5 nT between $Dst = 0$ and $Dst = -100$ nT and 50 nT between $Dst = -100$ nT and $Dst = -200$ nT.

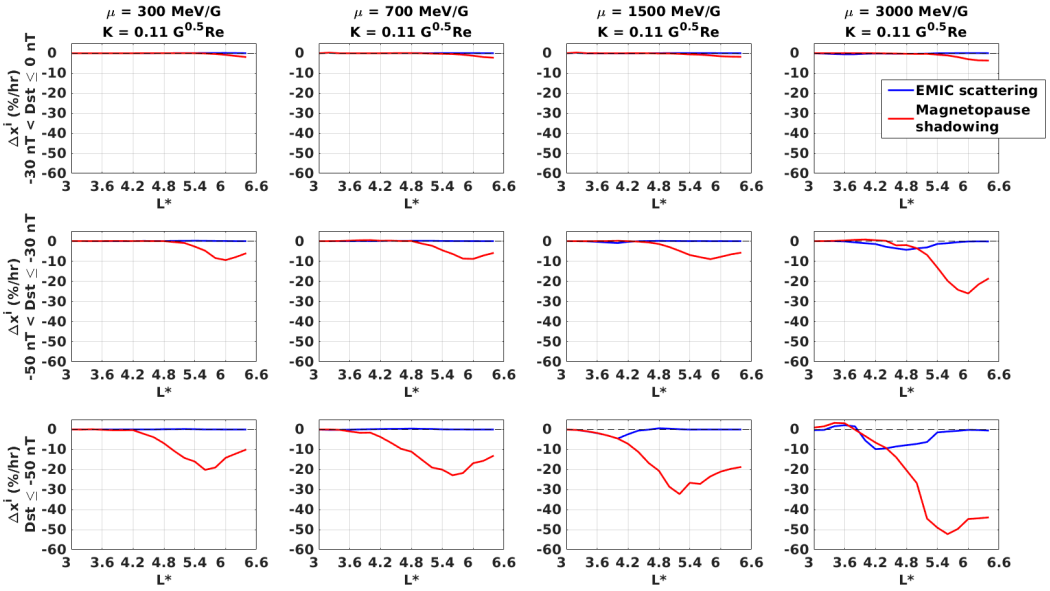

FIGURE 8.14: Difference of innovations $\Delta\mathbf{x}^i$ binned by L^* for different intervals of geomagnetic activity defined by Dst index for the indicated pairs of adiabatic invariants μ and K. Blue (red) lines denote loss due to EMIC scattering (magnetopause shadowing).

8.4.3 Comparison of Loss Mechanisms

The previous sections have quantitatively determined via data assimilation the effect of EMIC scattering and magnetopause shadowing in the outer radiation belt. Here, both processes are analysed simultaneously and the magnitude and the spatial extent (in L^*) of the loss induced by them is compared. Figure 8.14 presents the difference $\Delta\mathbf{x}^i$ as a function of radial distance averaged over the following levels of geomagnetic activity during the four-year period under study: -30 nT $< Dst \leq 0$ nT, -50 nT $< Dst \leq -30$ nT, and $Dst \leq -50$ nT. The minima of these curves are interpreted as the maximum loss achieved by either of the mechanisms. In accordance with the above-mentioned results, EMIC waves bring fewer loss than magnetopause shadowing. Loss due to EMIC waves is mostly seen at L^* between 3.6 and 4.6, whereas loss due to magnetopause shadowing is mainly evident at higher radial distances ($L^* \geq 4.8$).

The mimimum values of each curve of Figure 8.14, as well as their corresponding L^* locations, are plotted in panels (a) and (b) of Figure 8.15. For the lowermost geomagnetic activity level, with Dst between -30 nT and 0 nT, only loss due to magnetopause shadowing is apparent, fluctuating between 2%/hr and 4%/hr of the maximum PSD at $L^* = 6.4$. As Dst decreases between -50 nT and -30 nT, EMIC waves scatter electrons with $\mu > 1000$ MeV/G. Such loss reaches, at most, 5%/hr for the highest μ values, and is observed from $L^* = 3.6$ to $L^* = 4.8$. At the same geomagnetic activity level, magnetopause shadowing depletes electrons amounting from 10%/hr to 25%/hr of the maximum PSD between $L^* = 5.8$ and $L^* = 6$. For the intervals with $Dst \leq -50$ nT, the maximum EMIC induced scattering ($\Delta\mathbf{x}^i \leq 10\%$/hr) occurs at $3.4 \leq L^* \leq 4.2$, and it clearly intensifies with increasing μ. More dramatic loss is introduced by magnetopause shadowing, ranging on average between 20%/hr and 50%/hr, at L^* between 5.2 and 5.6.

Besides investigating the value and L^* of the maximum PSD loss, the location at which loss due to magnetopause shadowing starts dominating over that due to EMIC wave scattering is inspected, by finding the crossing between the red and

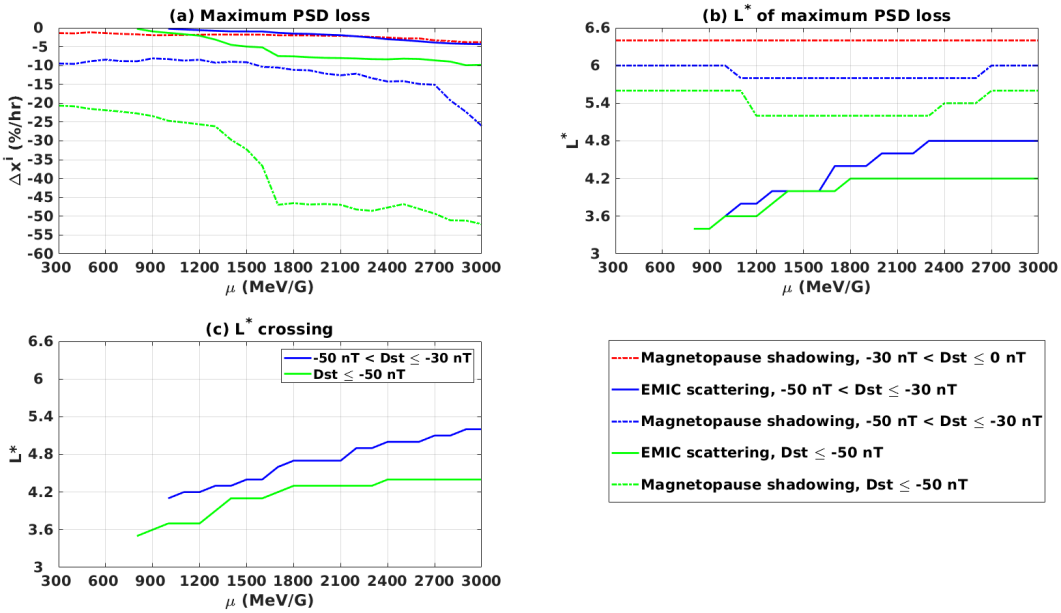

FIGURE 8.15: (a) Maximum loss (as defined by Δx^i) due to EMIC scattering and magnetopause shadowing for the indicated levels of geomagnetic activity; (b) L^* location corresponding to the maximum loss; (c) L^* boundary separating two distinct mechanisms of electron PSD loss.

blue curves in Figure 8.14. The corresponding L^* values are plotted in panel (c) of Figure 8.15. This intersection is clearly energy-dependent, and for Dst between -50 nT and -30 nT, it extends from $L^* = 4.1$ ($\mu = 1000$ MeV/G) to $L^* = 5.2$ ($\mu = 3000$ MeV/G), i.e. out of the two loss processes inspected, EMIC waves are the main scattering agent below such location, whereas magnetopause shadowing plays a dominant role above it. For more disturbed times, with $Dst \leq -50$ nT, this boundary moves inwards and fluctuates between $L^* = 3.5$ and $L^* = 4.4$. Nevertheless, it is worth noting that EMIC waves (magnetopause shadowing) may deplete electrons above (below) such location. As an example, for $Dst \leq -50$ nT and $\mu = 3000$ MeV/G, EMIC waves produce loss beyond the intersection at $L^* = 4.4$, extending out to $L^* = 5$. Conversely, loss due to magnetopause shadowing is already seen at $L^* = 4$.

8.5 Discussion and Conclusions

This chapter has employed four years of spacecraft data to statistically quantify the effect of two distinct loss processes over different levels of geomagnetic activity. Scattering by EMIC waves is shown to induce loss from $L^* = 3.6$ to $L^* = 5.6$, particularly between $L^* = 4$ and $L^* = 4.8$ during the most disturbed times. The resulting depletion amounts to between 10%/hr to 30%/hr of the maximum PSD. The effect of EMIC waves is seen starting from $\mu = 900$ MeV/G, and is energy-dependent, with higher energy electrons being affected the most over a broader range of L^*. These findings are consistent with previous observational and modelling studies (e.g. Usanova et al., 2014; Shprits et al., 2016; Drozdov et al., 2017; Xiang et al., 2017), and validate the employed wave model, since the behaviour of EMIC waves and the dynamics of the ultrarelativistic electron population are well reproduced.

In the current work only helium band EMIC waves are considered, thus only lower- equatorial pitch-angle electrons with energies between 2 and 4 MeV are significantly depleted, not affecting those with higher pitch angles. As mentioned in Section 3.3.2.2, additional contemporaneous scattering by hiss in plumes or by chorus is needed in order for EMIC waves to significantly deplete the entire pitch-angle distribution. It must be emphasised that the efficiency of EMIC wave scattering in the model, and the ensuing quantification of PSD loss, is subject to the assumed spectral characteristics, the ion composition, and the plasma density. Moreover, EMIC waves in the hydrogen band, which are neglected in this work, are generally most efficient, in combination with simultaneous chorus waves, in driving pitch-angle scattering and quickly precipitating the entire population of 2 MeV to 5 MeV electrons, up to large equatorial pitch angles (e.g. Mourenas et al., 2016; Zhang et al., 2017; Qin et al., 2019; Pinto et al., 2020). Inclusion of such waves, beyond the scope of this study, may impact the PSD reanalysis and, in consequence, the innovation vector and the estimation of PSD loss.

Loss due to magnetopause shadowing is the strongest between $L^* = 5$ and $L^* = 6.6$. Nevertheless, the depletion of electron PSD may extend further below $L^* = 4$ and reach between 50%/hr and 70%/hr of the maximum PSD, either for large values of geomagnetic indices or for enhanced solar wind dynamic pressure. This is in accordance with Shprits, Daae, and Ni (2012), who reconstructed a depletion of the radiation belt PSD down to $L^* = 3$, based on data assimilation, for a very high value of P_{dyn} around 50 nPa. Similar conclusions on the correlation between electron PSD dropout events and solar wind dynamic pressure pulses were reached by Ni et al. (2013b), based on a one-year reanalysis survey of multisatellite data. Such sharp increases of P_{dyn} clearly result in the compression of the magnetopause and the removal of electrons originally on closed drift orbits, with the most energetic populations affected to a larger extent. Statistically, for the range of μ values considered in this study, magnetopause shadowing tends to deplete more electrons than EMIC wave interactions during disturbed times.

The inclusion of the LCDS in the VERB-3D model, and the consequent estimation of the effect of magnetopause shadowing, is subject to several caveats. A number of different approaches can be employed to calculate the LCDS, including the widely used IRBEM library which is followed in this study. This code ignores drift orbit bifurcations (DOB) and the effects of electric fields. Albert et al. (2018) studied several codes to calculate the LCDS in different magnetic field models for four different disturbed periods, and concluded that, nevertheless, they produce seemingly reasonable and similar results. Moreover, it must be underlined that magnetic field models, such as TS07, are empirical approximations of the real field during geomagnetic disturbances. All these factors must be considered when studying the effects of magnetopause shadowing and quantifying the PSD loss brought in the model by this mechanism.

Furthermore, in order to test whether the location of the LCDS was correct, a series of simulations was conducted by shifting the location of the LCDS calculated from TS07D with the IRBEM library farther (i.e. adding 0.5 and 1 R_E to the LCDS) and closer (i.e. subtracting 0.5 and 1 R_E to the LCDS) to Earth, for the period 01 October 2012 to 01 October 2013. The results are depicted in Figure 8.16, where the normalised innovation $\mathbf{x}^i$ is plotted after including magnetopause shadowing ("full" run) for the different locations of the LCDS. The normalised innovations $\mathbf{x}^i$ with magnetopause shadowing where the LCDS is moved away from the Earth by 1 and 0.5 R_E exhibit more negative blue values of innovation $\mathbf{x}^i$ in comparison with the third row, which shows the location of the LCDS as estimated by using the IRBEM

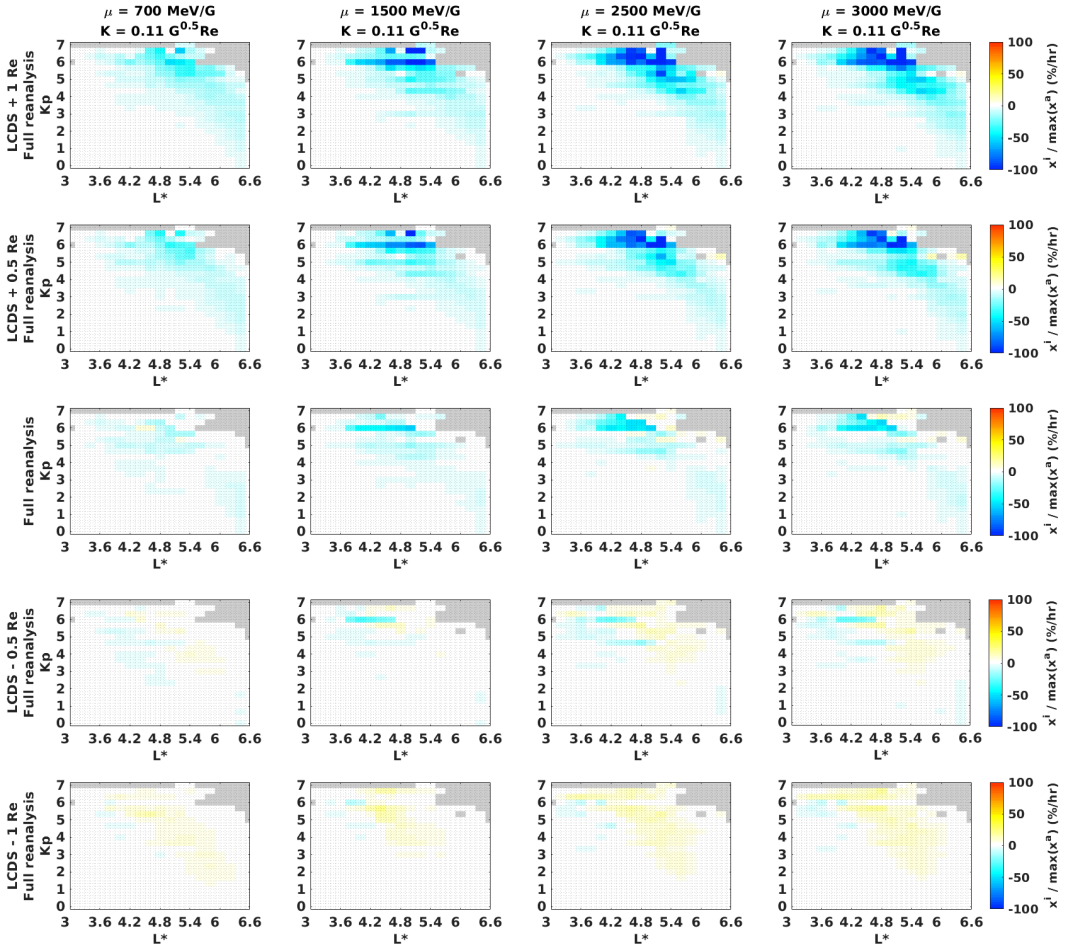

FIGURE 8.16: Normalised innovation vector $\mathbf{x}^i$ of the "full" run for several simulations with different locations of the LCDS: (i) first row: adding 1 R_E to the LCDS (i.e. moving the LCDS 1 R_E farther from Earth); (ii) second row: adding 0.5 R_E to the LCDS, (iii) third row: LCDS corresponding to the one employed in the paper, as calculated using TS07 model and the IRBEM library (i.e. no values were added or subtracted to the LCDS in this simulation); (iv) fourth row: subtracting 0.5 R_E to the LCDS (i.e. moving the LCDS 0.5 R_E closer to Earth); and (v) fifth row: subtracting 1 R_E to the LCDS.

library and TS07 model (with no added or subtracted values in R_E). This implies that the inclusion of this "displaced" LCDS does not bring enough loss to the model, hence a further missing loss process (as shown by the darker blue) is needed to account for such lack of PSD removal. In contrast, when the LCDS is shifted towards the Earth by subtracting 0.5 and 1 R_E, the normalised innovations $\mathbf{x}^i$ show a predominance of positive yellow values (particularly in the last case). This means that, after introducing magnetopause shadowing, a source process (which adds PSD) is missing to account for the PSD that is depleted in excess by the LCDS located too close to Earth. As a result, it is not necessary to subtract or add any distance in R_E to the LCDS location in order to achieve the best agreement with observations.

The results of this study imply the existence of a μ- and geomagnetic activity-dependent boundary fluctuating between $L^* = 3.5$ and $L^* = 5.2$ defining two regions in space where these two distinct loss mechanisms are mostly effective. EMIC induced scattering dominates below the boundary, whereas magnetopause shadowing coupled with outward radial diffusion is active above it (see Section 3.3.2).

Turner et al. (2014b) suggested this boundary to be located at $L^* \sim 4$. Yu, Koller, and Morley (2013) found it to be around $L^* \sim 5$, above which more than 90%/hr of the total loss is due to magnetopause shadowing together with outward radial diffusion, and below which only 60%/hr can be explained by this coupled mechanism. Dropouts, however, can encompass the entire outer radiation belt, and either mechanism can induce loss beyond the above-mentioned boundary. In other words, magnetopause shadowing can deplete electrons below it, and EMIC waves can efficiently scatter electrons beyond it, in particular during times of enhanced geomagnetic activity.

A similar conclusion with a boundary identified around $L^* \sim 4$ was reached by Xiang et al. (2017), based on a comprehensive investigation of three distinct radiation belt dropout events observed by the Van Allen Probes. In a later study, Xiang et al. (2018) extended its statistical analysis to four years of electron PSD measurements and found that EMIC wave scattering is the dominant dropout mechanism at low L^*, while dropouts at high L^* are due to a combination of EMIC wave scattering and magnetopause shadowing. The important effects of outward radial diffusion coupled with magnetopause shadowing and precipitation loss due to EMIC waves as described by Boynton, Mourenas, and Balikhin (2016) and Boynton, Mourenas, and Balikhin (2017) at GEO and $L \sim 4.2$, respectively, are also consistent with the findings from this chapter.

This statistical study relying on four years of data has shown that, in general, loss due to magnetopause shadowing tends to exceed loss produced by EMIC scattering. Nevertheless, this is not always the case, as during disturbed conditions (i.e. geomagnetic storms) the effect of EMIC waves can be comparable, or even exceed, the effect of magnetopause shadowing. Figure 8.17 shows two of these events, which correspond to intense storms following the classification of Gonzalez et al. (1994). The maximum depletion due to both EMIC waves and magnetopause shadowing (between 10%/hr and 20%/hr of the maximum PSD) is observed during the main phase of each storm, with smaller contributions during the initial phase and the beginning of the recovery phase. In these events, loss due to EMIC waves dominates in the heart of the outer radiation belt and is within the same order of magnitude as loss produced by magnetopause shadowing, demonstrating that EMIC waves are an indispensable agent in the dynamics of ultrarelativistic electrons.

The statistical model of ULF waves from Brautigam and Albert (2000) was employed in the current work. Recent studies (e.g. Mann and Ozeke, 2016; Olifer et al., 2018; Ozeke et al., 2020; Pinto et al., 2020) have employed stronger event-specific ULF wave diffusion rates derived from ground-based measurements and a low LCDS and have found a dominant role of magnetopause shadowing and outward radial diffusion down to $L = 3.5$ during storm times. Therefore, for individual events with $Dst < -50$ nT, the contribution of magnetopause shadowing can be larger than suggested in this statistical study and can even dominate down to between $L = 3$ and 3.6.

Additionally, and in order to assess the effect of stronger radial diffusion rates in the current statistical analysis, a series of simulations multiplying the ULF wave model from Brautigam and Albert (2000) by 10, 2, 0.5, and 0.1, was performed for the period 01 October 2012 to 01 October 2013. The corresponding innovations for the original "full" run and for the set of "full" runs with scaled radial diffusion coefficients are presented in Figure 8.18. Negative blue innovations, indicative of an overestimation of electron PSD by the model, are mainly present in the first two rows that employ increased radial diffusion rates. Conversely, such a difference is not observed when the ULF wave model is divided by 2 and by 10 (last two rows),

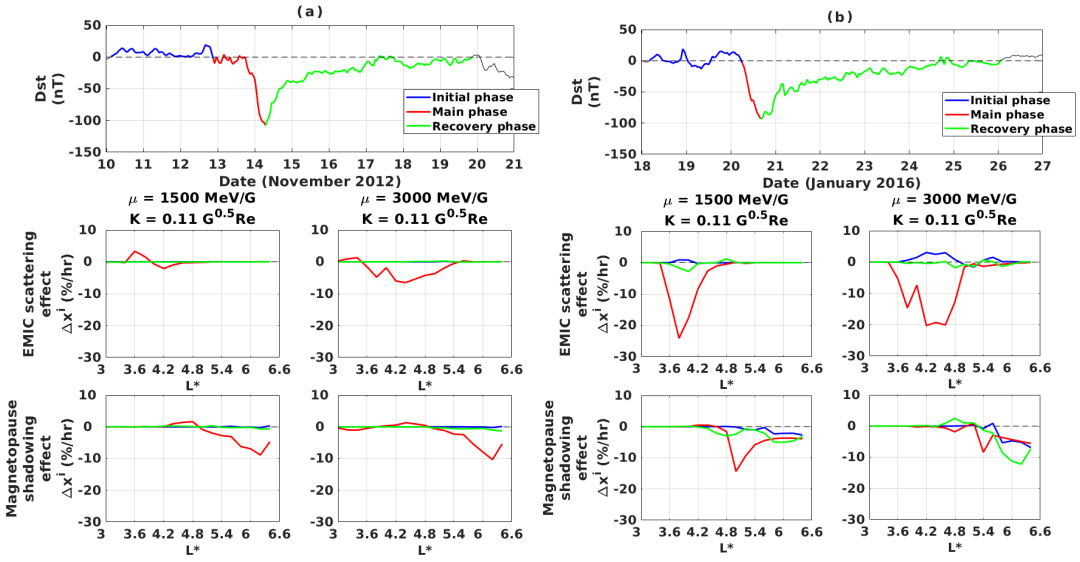

FIGURE 8.17: Difference of innovations for two geomagnetic storms. First row: evolution of Dst index for the storm with (a) $Dst_{\min} = -108$ nT on 14 November 2012 07 UT, and (b) $Dst_{\min} = -93$ nT on 20 January 2016 16 UT. The initial, main, and recovery phases are highlighted in blue, red, and green, respectively. Second row: difference of innovations $\Delta \mathbf{x}^i$ binned by L^* denoting losses due to scattering by EMIC waves for the indicated pairs of adiabatic invariants μ and K during different phases of the storm. Third row: same as second row, for magnetopause shadowing.

compared with the non-scaled case. This shows that, although stronger than average ULF wave models are able to reproduce individual events (as in the above-mentioned studies), for the current multi-year statistics the Brautigam and Albert (2000) radial diffusion rates adequately describe the majority of events.

The effects of scattering by EMIC waves and magnetopause shadowing have been studied individually in the current thesis, i.e. only one process was excluded from the model at a time. However, these two mechanisms can act simultaneously and complement each other in driving the dynamics of the outer belt. Magnetopause shadowing and the consequent outward radial diffusion develop negative PSD gradients at higher L shells (e.g. Turner et al., 2012a), while localised and fast loss driven by EMIC waves produces deepening minimums in PSD around $L^* = 3.5$ to $L^* = 4.5$ (e.g. Aseev et al., 2017; Shprits et al., 2017), and therefore can influence the rate of outward diffusion. The combination of both processes results in efficient dropouts of radiation belt electrons, creating several localised peaks in PSD. Moreover, EMIC wave scattering and LCDS location (and consequently, magnetopause shadowing) are also pitch angle (or K) dependent. EMIC waves are only effective at scattering electrons with lower pitch angles (e.g. Usanova et al., 2014; Drozdov et al., 2017), whereas magnetopause shadowing affects mainly high pitch angles (e.g. Roederer, 1967; West, Buck, and Walton, 1972). As a result, both mechanisms can remove together a broad range of particles. This can irreversibly alter the content of the outer belt and can lead to almost total depletion of the pre-existing electron population. Future work will focus on estimating the K dependence of scattering by EMIC waves and magnetopause shadowing via the analysis of the innovation vector.

After adding EMIC waves and magnetopause shadowing in the model (i.e. performing the "full" run), a region of positive innovation (in yellow and red) remains

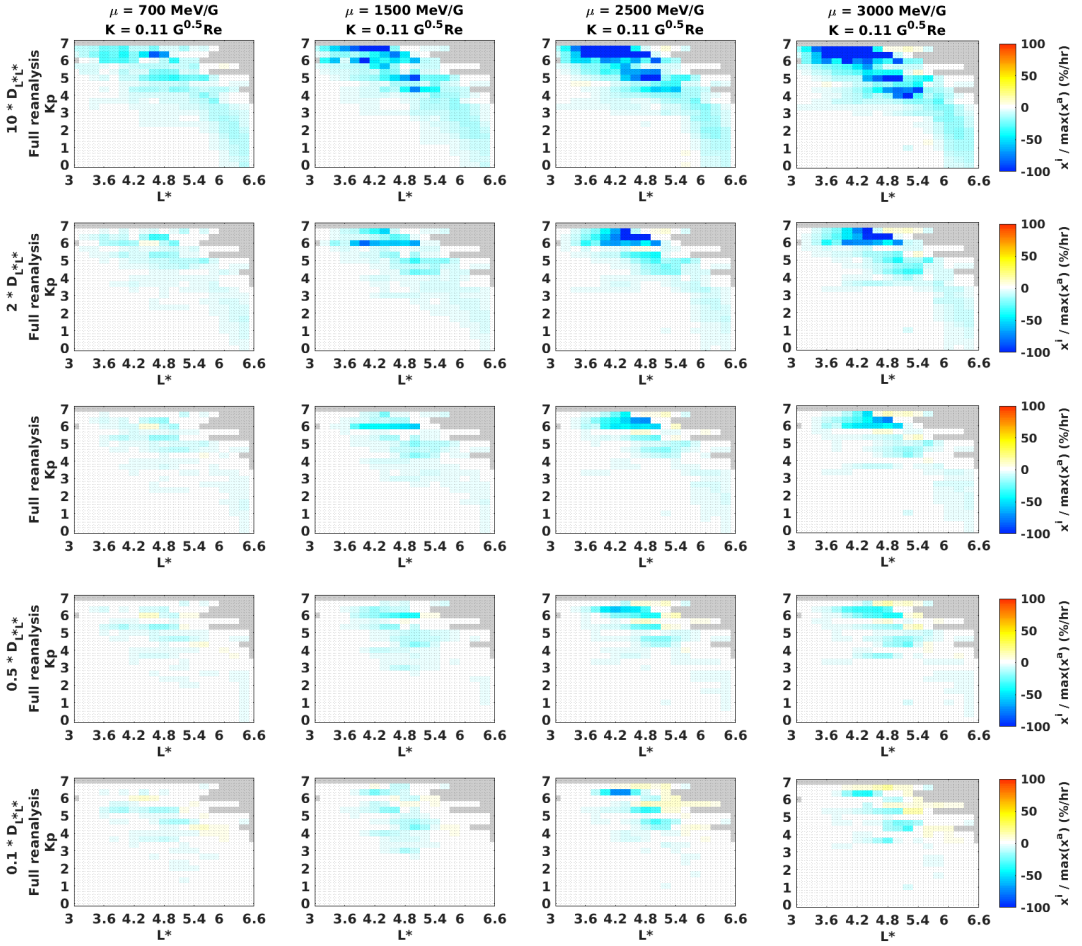

FIGURE 8.18: Normalised innovation vector $\mathbf{x}^i$ of the "full" run for several simulations scaling $D_{L^*L^*}$ from Brautigam and Albert (2000) by several factors as indicated in each row.

at $L^* > 4.2$ and $Kp > 6$. This underestimation of electron PSD could be due to the fact that the calculation of the LCDS does not account for DOB, as mentioned, thus depleting electron PSD in excess. Another explanation for this underestimation of PSD is related to the electric field induced by the compression of the magnetopause. Such electric field might mitigate some of the ensuing loss by radially transporting the electron population inwards.

In this study only two processes leading to radiation belt dropouts have been examined: atmospheric precipitation due to EMIC wave-induced pitch-angle scattering, and magnetopause shadowing combined with outward radial diffusion. Nevertheless, there are other mechanisms through which energetic electrons in Earth's outer radiation belt may be depleted. For instance, Chaston et al. (2018) showed that the drift-bounce motion of electrons in the magnetic field of broadband kinetic Alfvén waves may lead to outward transport sufficient to account for electron depletion during the main phase of geomagnetic storms. In a later case study, Chaston et al. (2019) employed the properties of such Alfvénic fluctuations to build a model for pitch-angle scattering. At energies of hundreds of keV to several MeV, kinetic Alfvén waves provided pitch-angle diffusion rates competitive with those estimated for chorus and drift averaged EMIC waves. They concluded that such pitch-angle scattering may lead to the transport of electrons into the loss cone on timescales on the order of hours and account for significant loss in the radiation belts.

A second mechanism that leads to electron dropouts and that is not included in the VERB-3D model is deceleration due to nonlinear electron phase bunching by high-amplitude whistler waves. Vainchtein et al. (2018) investigated the nonlinear resonant electron interaction with long and intense chorus wave packets in the outer belt, and derived a generalised kinetic equation for electrons that encompasses nonlinear interactions, such as phase trapping and phase bunching effects not described by quasi-linear diffusion. Zhang et al. (2019) performed a statistical analysis of lower-band chorus wave packets and concluded that the evolution of 0.1 to 1 MeV electron fluxes at L between 4 and 6 in the outer belt should mainly result from fast nonlinear effects, such as phase trapping and bunching, rather than from quasi-linear diffusion as commonly assumed. More recently, Gan et al. (2020) performed test particle simulations to model the interaction between electrons and chorus waves, and found that wave amplitude modulations can extend the nonlinear regime and enhance the scattering due to phase bunching.

As argued by Onsager et al. (2002), flux dropouts can also occur due the development of a localised, tail-like stretching of the magnetic field, typically associated with substorms (e.g. Nagai, 1982; Baker and McPherron, 1990). Spacecraft observations have shown that these substorm-related dropouts are mostly localised to the midnight sector, within approximately two hours of local midnight (Baker and McPherron, 1990). Onsager et al. (2002) investigated the response to a moderate magnetic storm and found that $E > 2$ MeV electron fluxes drop abruptly but not concurrently at different local times. Moreover, they also showed that the dropout extended as low as $L \sim 4$, and noted that the loss was related to stretched field topographies. The scattering effect of increased field line curvature on stretched field lines is an important process which has not been accounted for in this work.

The technique that has been presented in this chapter can be applied to other geophysical systems where the relative contribution of specific mechanisms needs to be quantified. This comes with several caveats, however. First of all, while this technique relies on spacecraft observations, the results are not completely independent of the assumptions of the model, such as the times when EMIC waves operate, the neglect of hydrogen band EMIC waves, or the location of the LCDS. Second, the metric that has been introduced, $\Delta\mathbf{x}^i$, does not indicate the actual number of electrons lost (an integration would be necessary), but rather expresses the loss in each time step as a function of the hourly maximum PSD. In this regard, the normalisation factor has been chosen to be the maximum value of assimilated PSD over all L^*, instead of the current state at each individual L^*, to avoid division by small values, which would have yielded large percentage differences at some locations. Lastly, errors in the model may arise, e.g. from the employed wave parametrisations or the dynamic pressure threshold used to turn on EMIC waves in the model, and in turn, may affect the reconstructed electron PSD and the innovation vector. Nevertheless, the difference of innovations $\Delta\mathbf{x}^i$ can be used to indicate when discrepancies between predictions and observations arise and to pinpoint possible sources of error in the model. In the current study, values of $\Delta\mathbf{x}^i$ are mainly negative and hence, indicate that loss by EMIC waves and magnetopause shadowing decrease the modelled PSD and generally bring the model output closer to observations.

Chapter 9

Summary and Future Work

9.1 Summary

The Earth is surrounded by two toroidal shaped regions of electrons trapped in the geomagnetic field, known as the Van Allen electron radiation belts. In the highly dynamic outer belt, fluxes change dramatically and may vary by up to several orders of magnitude on timescales ranging from minutes and hours, up to months and years. Understanding the variability of electrons in the outer radiation belt is a complex problem involving a variety of source, transport, and loss processes.

The research presented in this thesis explored the fast loss of electrons from the outer radiation belt during dropouts. In order to obtain a comprehensive picture of the outer belt and understand its dynamic variability, data assimilation was used to reconstruct radial profiles of electron PSD. In comparison to previous studies, this approach accounted and corrected for limited data coverage, instrumental errors, and inaccurate model physics. Observations from the twin Van Allen Probes A and B and satellites 13 and 15 from the GOES fleet were assimilated into the VERB-3D model by means of a split-operator Kalman filter, from 01 October 2012 to 01 October 2016.

The applicability of the innovation vector to pinpoint when and where missing physics in the model become apparent was presented in Chapter 7. For this purpose, three processes were systematically added to the data assimilative scheme: mixed pitch angle-energy diffusion by chorus and hiss waves, pitch-angle scattering due to EMIC waves, and magnetopause shadowing; and the innovation was inspected for chosen values of the invariants μ and K. The results, on the basis of a six-month reconstruction of electron PSD, showed that mixed pitch angle-energy diffusion removes PSD from the model, and its effect is stronger at lower values of the equatorial pitch angle than at higher values.

The analysis of the innovation vector in Chapter 7 also highlighted that EMIC waves mostly induce loss of $E > 2$ MeV electrons with equatorial pitch angles less than 60^{o}, on average. For a fixed invariant K, the scattering effect of EMIC waves was observed to increase for larger values of μ (and therefore, of energy), than for lower μ. Furthermore, inclusion of magnetopause shadowing driven by the LCDS brought loss into the model as well, particularly at $L^* > 5$. The resulting innovation vector illustrated a region of large underestimation of electron PSD at large radial distances and low energies, caused by the absence of magnetospheric convection in the model.

Based on a four-year reanalysis of electron PSD, Chapter 8 aimed to further characterise the effect of two of the above-mentioned mechanisms: scattering due to EMIC waves and magnetopause shadowing, by identifying where (in L^*) and under

which conditions (as described by Kp and Dst as well as solar wind dynamic pressure) they operate. The loss produced by these non-adiabatic processes was quantified through a metric based on the difference of the innovation before and after their inclusion in the model. The energy dependence of these two distinct mechanisms was also explored, with μ ranging from 300 to 3000 MeV/G (E between $\sim$ 800 keV and $\sim$ 3.6 MeV).

On average, it was found that loss due to EMIC wave scattering (between 10%/hr and 30%/hr of the maximum PSD) is energy-dependent (consistent with the results of Chapter 7), and mostly affects higher-energy electrons over a wider range of L^*. The analysis of the difference of innovations showed that the largest loss induced by EMIC waves occurred during disturbed times between $L^* = 4$ and $L^* = 4.8$. On the other hand, loss produced by magnetopause shadowing reached between 50%/hr and 70%/hr of the maximum PSD, and was mostly evident between $L^* = 5$ and $L^* = 6.6$, although it reached below $L^* = 4$ under very disturbed conditions, i.e. high values of Kp or enhanced solar wind dynamic pressure.

The statistical analysis of the four-year innovation vector suggested that, for the range of μ values studied in this work, loss produced by magnetopause shadowing tends to exceed loss induced by EMIC wave interactions. However, for individual events during disturbed conditions, the effect of EMIC waves was shown to reach the same level, or even exceed, the effect of magnetopause shadowing. Moreover, an energy- and geomagnetic activity-dependent boundary separating both mechanisms, located between $L^* = 3.5$ and $L^* = 5.2$, was evident in the reanalysis. Scattering by EMIC waves tends to be active below it, while magnetopause shadowing mostly dominates above it.

Several important approximations were employed in the current study, e.g. statistical models of ULF, whistler mode chorus and hiss, and helium band EMIC waves, density and composition of the multi-ion magnetospheric plasma, lack of hydrogen band EMIC waves, and external magnetic field model. These numerous approximations might lead to significant uncertainties in the estimation of the actual effect of the two loss processes leading to dropouts that were examined in this work. Nevertheless, the findings of this thesis are consistent with other observational and modelling studies, both regarding the location and the relative contribution of scattering due to EMIC waves and magnetopause shadowing.

The work carried out in this dissertation has resulted in the first publicly available long-term reconstruction of the Van Allen belts. This product will undoubtedly provide a tool to further understand the acceleration, loss, and transport processes which dictate the dynamics of the radiation belts. In turn, this overall physical understanding will be then transitioned into accurate space weather and radiation forecasts.

9.2 Outlook for Future Studies

The technique presented in this thesis, based on the analysis of the innovation before and after including a specific mechanism in the model, will be extended in future studies to quantify and assess the contribution of other waves, such as plasmaspheric hiss and whistler mode chorus, to the dynamic evolution of electron PSD. As mentioned in Chapter 3, chorus waves play a dual role in both the loss and acceleration of radiation belt electrons. The methodology presented in Chapter 8 will be useful in differentiating under which geomagnetic conditions chorus waves contribute most, either to scattering loss or to local acceleration. The effect of individual

mechanisms, e.g. radial diffusion driven by ULF waves, can also be explored via the innovation vector. Furthermore, the same methodology will be applied to the analysis of the dynamics of other geophysical systems of interest, such as the plasmasphere and the ring current.

In contrast to the statistical four-year analysis of the role of scattering by EMIC waves and magnetopause shadowing conducted in Chapter 8, the effect of these two processes will be inspected in detail for selected events, such as the 110 geomagnetic storms identified by Turner et al. (2019) during the Van Allen Probes era. Such analysis will allow to determine the percentage of dropout events dominated by either mechanism, and to identify drivers in the solar wind (e.g. CME and CIR driven storms) contributing to magnetopause shadowing dominant and/or to EMIC wave scattering dominant events. It can also reveal any dependence of the effect of these processes with respect to the temporal evolution of a given geomagnetic storm. Figure 8.17 showed that, for two selected storms, the largest loss due to both mechanisms occurs during the main phase. However, does magnetopause shadowing contribute exclusively throughout the main phase of a storm? Do EMIC waves play also role during the recovery phase of a storm? Do the effects of EMIC wave scattering and magnetopause shadowing are contemporaneous during storms? A temporal analysis of the differences of innovation might shed some light on these questions.

This study, and in particular Chapter 8, mostly focused on the μ dependence of EMIC wave scattering and magnetopause shadowing during radiation belt dropouts. In the future, the dependence of electron loss on the first two invariants μ and K will be investigated via the difference of innovations as presented in this thesis. Turner et al. (2014b), Xiang et al. (2017), and Xiang et al. (2018) performed an analysis of the loss of electron PSD based on Van Allen Probes data, for selected events and specific values of both invariants. The four-year reconstruction of electron PSD produced in this thesis, along with the newly-derived innovation-based metric, will be employed to further investigate this μ, K dependence, as typical limitations from observational studies, e.g. incomplete PSD profiles, can be overcome with this approach. Such analysis will provide critical clues to distinguish the dominant loss mechanisms at different radial distances over the outer radiation belt.

Finally, the data assimilative framework presented in this thesis will be extended to assimilate measurements from the last three years of the Van Allen Probes (October 2016 to October 2019) and from ongoing missions such as Arase (Miyoshi et al., 2018). In this regard, recent work has been undertaken to perform intercalibration between Van Allen Probes and Arase data during the overlap period between both missions. LEO spacecraft can also be incorporated into our scheme. However, as LEO-spacecraft measured fluxes are typically two to three orders of magnitude lower than e.g. Van Allen Probes observed fluxes, new methods that can incorporate measurements that differ by orders of magnitude will need to be developed. All these efforts will be ultimately directed towards achieving a better understanding of the dominant mechanisms during radiation belt enhancements and dropouts.

Bibliography

Akasofu, S. (1964). "The development of the auroral substorm". In: *Planetary and Space Science*, 12,4, pp. 273–282.

Albert, J.M. (2003). "Evaluation of quasi-linear diffusion coefficients for EMIC waves in a multispecies plasma". In: *Journal of Geophysical Research: Space Physics*, 108,A6.

Albert, J.M., N.P. Meredith, and R.B. Horne (2009). "Three-dimensional diffusion simulation of outer radiation belt electrons during the 9 October 1990 magnetic storm". In: *Journal of Geophysical Research: Space Physics*, 114,A9.

Albert, J.M. and Y.Y. Shprits (2009). "Estimates of lifetimes against pitch angle diffusion". In: *Journal of Atmospheric and Solar-Terrestrial Physics*, 71,16, pp. 1647–1652.

Albert, J.M. and S. Young (2005). "Multidimensional quasi-linear diffusion of radiation belt electrons". In: *Geophysical Research Letters*, 32,14.

Albert, J.M. et al. (2018). "Calculation of last closed drift shells for the 2013 GEM radiation belt challenge events". In: *Journal of Geophysical Research: Space Physics*, 123,11, pp. 9597–9611.

Aseev, N.A. and Y.Y. Shprits (2019). "Reanalysis of ring current electron phase space densities using Van Allen Probe observations, convection model, and log-normal Kalman filter". In: *Space Weather*, 17,4, pp. 619–638.

Aseev, N.A. et al. (2016). "Numerical applications of the advective-diffusive codes for the inner magnetosphere". In: *Space Weather*, 14,11, pp. 993–1010.

Aseev, N.A. et al. (2017). "Signatures of ultrarelativistic electron loss in the heart of the outer radiation belt measured by Van Allen Probes". In: *Journal of Geophysical Research: Space Physics*, 122,10, pp. 10–102.

Baker, D. et al. (2013). "The Relativistic Electron-Proton Telescope (REPT) instrument on board the Radiation Belt Storm Probes (RBSP) spacecraft: Characterization of Earth's radiation belt high-energy particle populations". In: *The Van Allen Probes Mission*. Springer, pp. 337–381.

Baker, D.N. (2002). "How to cope with space weather". In: *Science*, 297.5586, pp. 1486–1487.

Baker, D.N. and R.L. McPherron (1990). "Extreme energetic particle decreases near geostationary orbit: A manifestation of current diversion within the inner plasma sheet". In: *Journal of Geophysical Research: Space Physics*, 95,A5, pp. 6591–6599.

Baker, D.N. et al. (1986). "Highly relativistic electrons in the Earth's outer magnetosphere: 1. Lifetimes and temporal history 1979–1984". In: *Journal of Geophysical Research: Space Physics*, 91,A4, pp. 4265–4276.

Baker, D.N. et al. (1996). "Neutral line model of substorms: Past results and present view". In: *Journal of Geophysical Research: Space Physics*, 101,A6, pp. 12975–13010.

Baker, D.N. et al. (1998). "Disturbed space environment may have been related to pager satellite failure". In: *Eos, Transactions American Geophysical Union*, 79.40, pp. 477–483.

Baker, D.N. et al. (2004). "An extreme distortion of the Van Allen belt arising from the 'Hallowe'en'solar storm in 2003". In: *Nature*, 432,7019, pp. 878–881.

Baker, D.N. et al. (2014). "An impenetrable barrier to ultrarelativistic electrons in the Van Allen radiation belts". In: *Nature*, 515,7528, pp. 531–534.

Baker, D.N. et al. (2018). "Space weather effects in the Earth's radiation belts". In: *Space Science Reviews*, 214,1, p. 17.

Bartels, J., N.H. Heck, and H.F. Johnston (1939). "The three-hour-range index measuring geomagnetic activity". In: *Terrestrial Magnetism and Atmospheric Electricity*, 44,4, pp. 411–454.

Bartels, J. and J. Veldkamp (1949). "International data on magnetic disturbances, first quarter, 1949". In: *Journal of Geophysical Research*, 54,3, pp. 295–299.

Baumjohann, W. and R. Treumann (2012). *Basic space plasma physics*. Imperial College Press.

Beutier, T. and D. Boscher (1995). "A three-dimensional analysis of the electron radiation belt by the Salammbô code". In: *Journal of Geophysical Research: Space Physics*, 100,A8, pp. 14853–14861.

Blake, J. et al. (2013). "The Magnetic Electron Ion Spectrometer (MagEIS) instruments aboard the Radiation Belt Storm Probes (RBSP) spacecraft". In: *The Van Allen Probes Mission*. Springer, pp. 383–421.

Blake, J.B. et al. (1992). "Injection of electrons and protons with energies of tens of MeV into $L < 3$ on 24 March 1991". In: *Geophysical Research Letters*, 19,8, pp. 821–824.

Borovsky, J.E. and M.H. Denton (2006). "Differences between CME-driven storms and CIR-driven storms". In: *Journal of Geophysical Research: Space Physics*, 111,A7.

Bortnik, J., R.M. Thorne, and N.P. Meredith (2007). "Modeling the propagation characteristics of chorus using CRRES suprathermal electron fluxes". In: *Journal of Geophysical Research: Space Physics*, 112,A8.

— (2008). "The unexpected origin of plasmaspheric hiss from discrete chorus emissions". In: *Nature*, 452,7183, pp. 62–66.

Bortnik, J. et al. (2006). "Observation of two distinct, rapid loss mechanisms during the 20 November 2003 radiation belt dropout event". In: *Journal of Geophysical Research: Space Physics*, 111,A12.

Bortnik, J. et al. (2009). "An observation linking the origin of plasmaspheric hiss to discrete chorus emissions". In: *Science*, 324,5928, pp. 775–778.

Boscher, D. et al. (2010). "IRBEM library v4. 3, 2004–2008". In: *ONERA-DESP*.

Bourdarie, S. and V. Maget (2012). "Electron radiation belt data assimilation with an ensemble Kalman filter relying on the Salammbô code". In: *Annales Geophysicae*, 30,6, pp. 929–943.

Bourdarie, S. et al. (1996). "Magnetic storm modeling in the Earth's electron belt by the Salammbô code". In: *Journal of Geophysical Research: Space Physics*, 101,A12, pp. 27171–27176.

Bourdarie, S. et al. (1997). "Electron and proton radiation belt dynamic simulations during storm periods: A new asymmetric convection-diffusion model". In: *Journal of Geophysical Research: Space Physics*, 102,A8, pp. 17541–17552.

Boyd, A.J. et al. (2014). "Quantifying the radiation belt seed population in the 17 March 2013 electron acceleration event". In: *Geophysical Research Letters*, 41,7, pp. 2275–2281.

Boyd, A.J. et al. (2019). "RBSP-ECT Combined Spin-Averaged Electron Flux Data Product". In: *Journal of Geophysical Research: Space Physics*, 124.11, pp. 9124–9136.

Boynton, R.J., D. Mourenas, and M.A. Balikhin (2016). "Electron flux dropouts at Geostationary Earth Orbit: Occurrences, magnitudes, and main driving factors". In: *Journal of Geophysical Research: Space Physics*, 121,9, pp. 8448–8461.

— (2017). "Electron flux dropouts at $L \sim 4.2$ from Global Positioning System satellites: Occurrences, magnitudes, and main driving factors". In: *Journal of Geophysical Research: Space Physics*, 122,11, pp. 11–428.

Brautigam, D. and J.M. Albert (2000). "Radial diffusion analysis of outer radiation belt electrons during the October 9, 1990, magnetic storm". In: *Journal of Geophysical Research: Space Physics*, 105,A1, pp. 291–309.

Carpenter, D. and R. Anderson (1992). "An ISEE/whistler model of equatorial electron density in the magnetosphere". In: *Journal of Geophysical Research: Space Physics*, 97,A2, pp. 1097–1108.

Cervantes, S. et al. (2020a). "Identifying radiation belt electron source and loss processes by assimilating spacecraft data in a three-dimensional diffusion model". In: *Journal of Geophysical Research: Space Physics*, 125,1.

Cervantes, S. et al. (2020b). "Quantifying the effects of EMIC wave scattering and magnetopause shadowing in the outer electron radiation belt by means of data assimilation". In: *Journal of Geophysical Research: Space Physics*, 125,1.

Chaston, C.C. et al. (2018). "Radiation belt "dropouts" and drift-bounce resonances in broadband electromagnetic waves". In: *Geophysical Research Letters*, 45,5, pp. 2128–2137.

Chaston, C.C. et al. (2019). "Pitch angle scattering and loss of radiation belt electrons in broadband electromagnetic waves". In: *Geophysical Research Letters*, 45,18, pp. 9344–9352.

Chen, Y., G.D. Reeves, and R.H.W. Friedel (2007). "The energization of relativistic electrons in the outer Van Allen radiation belt". In: *Nature Physics*, 3,9, pp. 614–617.

Claudepierre, S.G., S.R. Elkington, and M. Wiltberger (2008). "Solar wind driving of magnetospheric ULF waves: Pulsations driven by velocity shear at the magnetopause". In: *Journal of Geophysical Research: Space Physics*, 113,A5.

Claudepierre, S.G. et al. (2009). "Magnetospheric cavity modes driven by solar wind dynamic pressure fluctuations". In: *Geophysical Research Letters*, 36,13.

Claudepierre, S.G. et al. (2015). "A background correction algorithm for Van Allen Probes MagEIS electron flux measurements". In: *Journal of Geophysical Research: Space Physics*, 120,7, pp. 5703–5727.

Claudepierre, S.G. et al. (2017). "The hidden dynamics of relativistic electrons (0.7–1.5 MeV) in the inner zone and slot region". In: *Journal of Geophysical Research: Space Physics*, 122,3, pp. 3127–3144.

Cornwall, J.M., F.V. Coroniti, and R. M. Thorne (1970). "Turbulent loss of ring current protons". In: *Journal of Geophysical Research*, 75,25, pp. 4699–4709.

Craven, J.D. (1966). "Temporal variations of electron intensities at low altitudes in the outer radiation zone as observed with satellite Injun 3". In: *Journal of Geophysical Research*, 71,23, pp. 5643–5663.

Daae, M. et al. (2011). "Reanalysis of radiation belt electron phase space density using various boundary conditions and loss models". In: *Advances in Space Research*, 48,8, pp. 1327–1334.

Daglis, I.A. et al. (1999). "The terrestrial ring current: Origin, formation, and decay". In: *Reviews of Geophysics*, 37,4, pp. 407–438.

Daley, R. (1991). *Atmospheric data analysis*. Cambridge University Press.

Davis, T.N. and M. Sugiura (1966). "Auroral electrojet activity index AE and its universal time variations". In: *Journal of Geophysical Research*, 71,3, pp. 785–801.

Denton, M.H. et al. (2006). "Geomagnetic storms driven by ICME-and CIR-dominated solar wind". In: *Journal of Geophysical Research: Space Physics*, 111,A7.

Dessler, A.J. and R. Karplus (1961). "Some effects of diamagnetic ring currents on Van Allen radiation". In: *Journal of Geophysical Research*, 66,8, pp. 2289–2295.

Dessler, A.J. and E.N. Parker (1959). "Hydromagnetic theory of geomagnetic storms". In: *Journal of Geophysical Research*, 64,12, pp. 2239–2252.

Drozdov, A.Y. et al. (2015). "Energetic, relativistic, and ultrarelativistic electrons: Comparison of long-term VERB code simulations with Van Allen Probes measurements". In: *Journal of Geophysical Research: Space Physics*, 120,5, pp. 3574–3587.

Drozdov, A.Y. et al. (2017). "EMIC wave parameterization in the long-term VERB code simulation". In: *Journal of Geophysical Research: Space Physics*, 122,8, pp. 8488–8501.

Drozdov, A.Y. et al. (2020). "The Role of Hiss, Chorus, and EMIC Waves in the Modeling of the Dynamics of the Multi-MeV Radiation Belt Electrons". In: *Journal of Geophysical Research: Space Physics*, 125,9, e2020JA028282.

Dungey, J.W. (1961). "Interplanetary magnetic field and the auroral zones". In: *Physical Review Letters*, 6,2, p. 47.

Echer, E., W.D. Gonzalez, and B.T. Tsurutani (2011). "Statistical studies of geomagnetic storms with peak $Dst \leq -50$ nT from 1957 to 2008". In: *Journal of Atmospheric and Solar-Terrestrial Physics*, 73,11-12, pp. 1454–1459.

Elkington, S.R. (2006). "A review of ULF interactions with radiation belt electrons". In: *Magnetospheric ULF waves: Synthesis and new directions*, 169, pp. 177–193.

Elkington, S.R., M.K. Hudson, and A.A. Chan (1999). "Acceleration of relativistic electrons via drift-resonant interaction with toroidal-mode Pc-5 ULF oscillations". In: *Geophysical Research Letters*, 26,21, pp. 3273–3276.

Evensen, G. (1994). "Sequential data assimilation with a nonlinear quasi-geostrophic model using Monte Carlo methods to forecast error statistics". In: *Journal of Geophysical Research: Oceans*, 99,C5, pp. 10143–10162.

— (2009). *Data assimilation: the ensemble Kalman filter*. Springer Science & Business Media.

Fälthammar, C.-G. (1965). "Effects of time-dependent electric fields on geomagnetically trapped radiation". In: *Journal of Geophysical Research*, 70,11, pp. 2503–2516.

Fennell, J.F. et al. (2005). "The energetic electron response to magnetic storms: HEO satellite observations". In: *The Inner Magnetosphere: Physics and Modeling*, 155, pp. 87–95.

Fennell, J.F. et al. (2015). "Van Allen Probes show that the inner radiation zone contains no MeV electrons: ECT/MagEIS data". In: *Geophysical Research Letters*, 42,5, pp. 1283–1289.

Foster, J.C. et al. (2014). "Prompt energization of relativistic and highly relativistic electrons during a substorm interval: Van Allen Probes observations". In: *Geophysical Research Letters*, 41,1, pp. 20–25.

Fraser, B.J. and T.S. Nguyen (2001). "Is the plasmapause a preferred source region of electromagnetic ion cyclotron waves in the magnetosphere?" In: *Journal of Atmospheric and Solar-Terrestrial Physics*, 63,11, pp. 1225–1247.

Friedel, R.H.W., G.D. Reeves, and T. Obara (2002). "Relativistic electron dynamics in the inner magnetosphere — A review". In: *Journal of Atmospheric and Solar-Terrestrial Physics*, 64,2, pp. 265–282.

Friedel, R.H.W. et al. (2001). "Plasma sheet access to the inner magnetosphere". In: *Journal of Geophysical Research: Space Physics*, 106,A4, pp. 5845–5858.

Gan, L. et al. (2020). "Nonlinear interactions between radiation belt electrons and chorus waves: dependence on wave amplitude modulation". In: *Geophysical Research Letters*, 47,4.

Ganushkina, N.Y. et al. (2014). "Low-energy electrons (5–50 keV) in the inner magnetosphere". In: *Journal of Geophysical Research: Space Physics*, 119,1, pp. 246–259.

Gary, S.P. (1992). "What is a plasma instability?" In: *Eos, Transactions American Geophysical Union*, 73,49, pp. 529–533.

Ghil, M. and P. Malanotte-Rizzoli (1991). "Data assimilation in meteorology and oceanography". In: *Advances in Geophysics*, vol. 33, Elsevier, pp. 141–266.

Godinez, H.C. et al. (2016). "Ring current pressure estimation with RAM-SCB using data assimilation and Van Allen Probe flux data". In: *Geophysical Research Letters*, 43,23, pp. 11–948.

Gombosi, T.I. (1998). *Physics of the space environment*. Cambridge University Press.

Gonzalez, W.D. et al. (1994). "What is a geomagnetic storm?" In: *Journal of Geophysical Research: Space Physics*, 99,A4, pp. 5771–5792.

Green, J.C. and M.G. Kivelson (2004). "Relativistic electrons in the outer radiation belt: Differentiating between acceleration mechanisms". In: *Journal of Geophysical Research: Space Physics*, 109,A3.

Green, J.C., J. Likar, and Y.Y. Shprits (2017). "Impact of space weather on the satellite industry". In: *Space Weather*, 15.6, pp. 804–818.

Green, J.C. et al. (2004). "Testing loss mechanisms capable of rapidly depleting relativistic electron flux in the Earth's outer radiation belt". In: *Journal of Geophysical Research: Space Physics*, 109,A12.

Hanser, F. (2011). "EPS/HEPAD calibration and data handbook". In: *Tech. Rep. GOESN-ENG-048D*.

Hargreaves, J.K. (1992). *The solar-terrestrial environment: an introduction to geospace*. Cambridge University Press.

Hikishima, M. et al. (2009). "Coherent nonlinear scattering of energetic electrons in the process of whistler mode chorus generation". In: *Journal of Geophysical Research: Space Physics*, 114,A10.

Horne, R.B and R.M. Thorne (1998). "Potential waves for relativistic electron scattering and stochastic acceleration during magnetic storms". In: *Geophysical Research Letters*, 25,15, pp. 3011–3014.

Horne, R.B. and R.M. Thorne (2003). "Relativistic electron acceleration and precipitation during resonant interactions with whistler-mode chorus". In: *Geophysical Research Letters*, 30,10.

Horne, R.B. et al. (2003). "Evolution of energetic electron pitch angle distributions during storm time electron acceleration to megaelectronvolt energies". In: *Journal of Geophysical Research: Space Physics*, 108,A1, SMP–11.

Horne, R.B. et al. (2005a). "Timescale for radiation belt electron acceleration by whistler mode chorus waves". In: *Journal of Geophysical Research: Space Physics*, 110,A3.

Horne, R.B. et al. (2005b). "Wave acceleration of electrons in the Van Allen radiation belts". In: *Nature*, 437,7056, pp. 227–230.

Horne, R.B. et al. (2013). "Space weather impacts on satellites and forecasting the Earth's electron radiation belts with SPACECAST". In: *Space Weather*, 11,4, pp. 169–186.

Hudson, M.K. et al. (1997). "Simulations of radiation belt formation during storm sudden commencements". In: *Journal of Geophysical Research: Space Physics*, 102,A7, pp. 14087–14102.

Hwang, J.A. et al. (2007). "Statistical significance of association between whistler-mode chorus enhancements and enhanced convection periods during high-speed streams". In: *Journal of Geophysical Research: Space Physics*, 112,A9.

Jaynes, A.N. et al. (2015). "Source and seed populations for relativistic electrons: Their roles in radiation belt changes". In: *Journal of Geophysical Research: Space Physics*, 120,9, pp. 7240–7254.

Jazwinski, A. (1970). *Stochastic and Filtering Theory. Mathematics in Sciences and Engineering Series*. Academic Press.

Jordanova, V.K. et al. (1998). "Effect of wave-particle interactions on ring current evolution for January 10–11, 1997: Initial results". In: *Geophysical Research Letters*, 25,15, pp. 2971–2974.

Kalman, R. (1960). "A new approach to linear filtering and prediction problems". In: *Journal of Basic Engineering*, 82,1, pp. 35–45.

Kalnay, E. (2003). *Atmospheric modeling, data assimilation and predictability*. Cambridge University Press.

Kataoka, R. and Y. Miyoshi (2006). "Flux enhancement of radiation belt electrons during geomagnetic storms driven by coronal mass ejections and corotating interaction regions". In: *Space Weather*, 4,9, pp. 1–11.

Kellerman, A. et al. (2014). "Three-dimensional data assimilation and reanalysis of radiation belt electrons: Observations of a four-zone structure using five spacecraft and the VERB code". In: *Journal of Geophysical Research: Space Physics*, 119,11, pp. 8764–8783.

Kersten, T. et al. (2014). "Electron losses from the radiation belts caused by EMIC waves". In: *Journal of Geophysical Research: Space Physics*, 119,11, pp. 8820–8837.

Kim, H. and A.A. Chan (1997). "Fully adiabatic changes in storm time relativistic electron fluxes". In: *Journal of Geophysical Research: Space Physics*, 102,A10, pp. 22107–22116.

Kim, K. et al. (2008). "Numerical calculations of relativistic electron drift loss effect". In: *Journal of Geophysical Research: Space Physics*, 113,A9.

King, J.H. and N.E. Papitashvili (2005). "Solar wind spatial scales in and comparisons of hourly Wind and ACE plasma and magnetic field data". In: *Journal of Geophysical Research: Space Physics*, 110,A2.

Kivelson, M.G. and C.T. Russell (1995). *Introduction to space physics*. Cambridge University Press.

Koller, J. et al. (2007). "Identifying the radiation belt source region by data assimilation". In: *Journal of Geophysical Research: Space Physics*, 112,A6.

Kondrashov, D., M. Ghil, and Y.Y. Shprits (2011). "Lognormal Kalman filter for assimilating phase space density data in the radiation belts". In: *Space Weather*, 9,11.

Kondrashov, D. et al. (2007). "A Kalman filter technique to estimate relativistic electron lifetimes in the outer radiation belt". In: *Journal of Geophysical Research: Space Physics*, 112,A10.

Kozyra, J.U. et al. (1984). "Effects of energetic heavy ions on electromagnetic ion cyclotron wave generation in the plasmapause region". In: *Journal of Geophysical Research: Space Physics*, 89,A4, pp. 2217–2233.

Kronberg, E.A. et al. (2017). "Comparing and contrasting dispersionless injections at geosynchronous orbit during a substorm event". In: *Journal of Geophysical Research: Space Physics*, 122,3, pp. 3055–3072.

Lahoz, W., B. Khattatov, and R. Ménard (2010). "Data assimilation and information". In: *Data Assimilation*, Springer, pp. 3–12.

Lam, M.M. et al. (2010). "Origin of energetic electron precipitation $>$ 30 keV into the atmosphere". In: *Journal of Geophysical Research: Space Physics*, 115,A4.

Landau, L.D. and E.M. Lifshits (1973). *Theoretical physics, vol. 1: Mechanics I*. Nauka Press.

Le Dimet, F. X. and O. Talagrand (1986). "Variational algorithms for analysis and assimilation of meteorological observations: theoretical aspects". In: *Tellus* 38,2, pp. 97–110.

Lenchek, A.M., S.F. Singer, and R.C. Wentworth (1961). "Geomagnetically trapped electrons from cosmic ray albedo neutrons". In: *Journal of Geophysical Research*, 66,12, pp. 4027–4046.

Li, W. and M.K. Hudson (2019). "Earth's Van Allen radiation belts: From discovery to the Van Allen Probes era". In: *Journal of Geophysical Research: Space Physics,* 124,11, pp. 8319–8351.

Li, W., Y.Y. Shprits, and R.M. Thorne (2007). "Dynamic evolution of energetic outer zone electrons due to wave-particle interactions during storms". In: *Journal of Geophysical Research: Space Physics,* 112,A10.

Li, W. et al. (2009). "Evaluation of whistler-mode chorus intensification on the nightside during an injection event observed on the THEMIS spacecraft". In: *Journal of Geophysical Research: Space Physics,* 114,A1.

Li, W. et al. (2010). "THEMIS analysis of observed equatorial electron distributions responsible for the chorus excitation". In: *Journal of Geophysical Research: Space Physics,* 115,A6.

Li, W. et al. (2014). "Radiation belt electron acceleration by chorus waves during the 17 March 2013 storm". In: *Journal of Geophysical Research: Space Physics,* 119,6, pp. 4681–4693.

Li, X. et al. (1993). "Simulation of the prompt energization and transport of radiation belt particles during the March 24, 1991 SSC". In: *Geophysical Research Letters,* 20,22, pp. 2423–2426.

Li, X. et al. (2015). "Upper limit on the inner radiation belt MeV electron intensity". In: *Journal of Geophysical Research: Space Physics,* 120,2, pp. 1215–1228.

Liu, S. et al. (2018). "Quantifying extremely rapid flux enhancements of radiation belt relativistic electrons associated with radial diffusion". In: *Geophysical Research Letters,* 45,3, pp. 1262–1270.

Liu, W.W., G. Rostoker, and D.N. Baker (1999). "Internal acceleration of relativistic electrons by large-amplitude ULF pulsations". In: *Journal of Geophysical Research: Space Physics,* 104,A8, pp. 17391–17407.

Lyons, L.R. and R.M. Thorne (1973). "Equilibrium structure of radiation belt electrons". In: *Journal of Geophysical Research,* 78,13, pp. 2142–2149.

Lyons, L.R. and D.J. Williams (1984). *Quantitative aspects of magnetospheric physics*. Vol. 23. Springer Science & Business Media.

Mann, I.R. and L.G. Ozeke (2016). "How quickly, how deeply, and how strongly can dynamical outer boundary conditions impact Van Allen radiation belt morphology?" In: *Journal of Geophysical Research: Space Physics,* 121,6, pp. 5553–5558.

Mann, I.R. et al. (2016). "Explaining the dynamics of the ultra-relativistic third Van Allen radiation belt". In: *Nature Physics,* 12.10, pp. 978–983.

Matsumura, C. et al. (2011). "Outer radiation belt boundary location relative to the magnetopause: Implications for magnetopause shadowing". In: *Journal of Geophysical Research: Space Physics,* 116.A6.

Mauk, B. et al. (2012). "Science objectives and rationale for the Radiation Belt Storm Probes mission". In: *The Van Allen Probes Mission*. Springer, pp. 3–27.

McAdams, K.L. and G.D. Reeves (2001). "Non-adiabatic response of relativistic radiation belt electrons to GEM magnetic storms". In: *Geophysical Research Letters,* 28,9, pp. 1879–1882.

McIlwain, C.E. (1961). "Coordinates for mapping the distribution of magnetically trapped particles". In: *Journal of Geophysical Research,* 66,11, pp. 3681–3691.

McPherron, R.L., C.T. Russell, and M.P. Aubry (1973). "Satellite studies of magnetospheric substorms on August 15, 1968: 9. Phenomenological model for substorms". In: *Journal of Geophysical Research,* 78,16, pp. 3131–3149.

Meredith, N.P., R.B. Horne, and R.R. Anderson (2001a). "Substorm dependence of chorus amplitudes: Implications for the acceleration of electrons to relativistic energies". In: *Journal of Geophysical Research: Space Physics,* 106,A7, pp. 13165–13178.

Meredith, N.P., R.B. Horne, and R.R. Anderson (2001b). "Substorm dependence of chorus amplitudes: Implications for the acceleration of electrons to relativistic energies". In: *Journal of Geophysical Research: Space Physics*, 106,A7, pp. 13165–13178.

Meredith, N.P. et al. (2003a). "Evidence for chorus-driven electron acceleration to relativistic energies from a survey of geomagnetically disturbed periods". In: *Journal of Geophysical Research: Space Physics*, 108,A6.

Meredith, N.P. et al. (2003b). "Favored regions for chorus-driven electron acceleration to relativistic energies in the Earth's outer radiation belt". In: *Geophysical Research Letters*, 30,16.

Meredith, N.P. et al. (2003c). "Statistical analysis of relativistic electron energies for cyclotron resonance with EMIC waves observed on CRRES". In: *Journal of Geophysical Research: Space Physics*, 108,A6.

Meredith, N.P. et al. (2004). "Substorm dependence of plasmaspheric hiss". In: *Journal of Geophysical Research: Space Physics*, 109,A6.

Meredith, N.P et al. (2006). "Energetic outer zone electron loss timescales during low geomagnetic activity". In: *Journal of Geophysical Research: Space Physics*, 111,A5.

Meredith, N.P. et al. (2007). "Slot region electron loss timescales due to plasmaspheric hiss and lightning-generated whistlers". In: *Journal of Geophysical Research: Space Physics*, 112,A8.

Meredith, N.P. et al. (2009). "Relativistic electron loss timescales in the slot region". In: *Journal of Geophysical Research: Space Physics*, 114,A3.

Meredith, N.P. et al. (2014). "Global morphology and spectral properties of EMIC waves derived from CRRES observations". In: *Journal of Geophysical Research: Space Physics*, 119,7, pp. 5328–5342.

Millan, R.M. and D.N. Baker (2012). "Acceleration of particles to high energies in Earth's radiation belts". In: *Space Science Reviews*, 173,1-4, pp. 103–131.

Millan, R.M. and R.M. Thorne (2007). "Review of radiation belt relativistic electron losses". In: *Journal of Atmospheric and Solar-Terrestrial Physics*, 69,3, pp. 362–377.

Miyoshi, Y. et al. (2018). "Geospace exploration project ERG". In: *Earth, Planets and Space*, 70.1, p. 101.

Morley, S.K. et al. (2010). "A rapid, global and prolonged electron radiation belt dropout observed with the Global Positioning System constellation". In: *Geophysical Research Letters*, 37,6.

Mourenas, D. et al. (2016). "Fast dropouts of multi-MeV electrons due to combined effects of EMIC and whistler mode waves". In: *Geophysical Research Letters*, 43,9, pp. 4155–4163.

Naehr, S.M. and F.R. Toffoletto (2005). "Radiation belt data assimilation with an extended Kalman filter". In: *Space Weather*, 3,6, pp. 1–15.

Nagai, T. (1982). "Local time dependence of electron flux changes during substorms derived from multi-satellite observation at synchronous orbit". In: *Journal of Geophysical Research: Space Physics*, 87,A5, pp. 3456–3468.

Nakano, S. et al. (2008). "A method for estimating the ring current structure and the electric potential distribution using energetic neutral atom data assimilation". In: *Journal of Geophysical Research: Space Physics*, 113,A5.

Ni, B. et al. (2008). "Resonant scattering of plasma sheet electrons by whistler-mode chorus: Contribution to diffuse auroral precipitation". In: *Geophysical Research Letters*, 35,11.

Ni, B. et al. (2009). "Reanalysis of relativistic radiation belt electron phase space density using multisatellite observations: Sensitivity to empirical magnetic field models". In: *Journal of Geophysical Research: Space Physics*, 114,A12.

Ni, B. et al. (2013a). "Resonant scattering and resultant pitch angle evolution of relativistic electrons by plasmaspheric hiss". In: *Journal of Geophysical Research: Space Physics,* 118,12, pp. 7740–7751.

Ni, B. et al. (2013b). "Responses of Earth's radiation belts to solar wind dynamic pressure variations in 2002 analyzed using multisatellite data and Kalman filtering". In: *Journal of Geophysical Research: Space Physics,* 118,7, pp. 4400–4414.

Nishimura, Y. et al. (2010). "Identifying the driver of pulsating aurora". In: *Science,* 330,6000, pp. 81–84.

Ohtani, S. et al. (2009). "On the loss of relativistic electrons at geosynchronous altitude: Its dependence on magnetic configurations and external conditions". In: *Journal of Geophysical Research: Space Physics* 114,A1.

Olifer, L. et al. (2018). "On the role of last closed drift shell dynamics in driving fast losses and Van Allen radiation belt extinction". In: *Journal of Geophysical Research: Space Physics,* 123,5, pp. 3692–3703.

Onsager, T. et al. (1996). "Operational uses of the GOES energetic particle detectors". In: *GOES-8 and Beyond*. Vol. 2812, International Society for Optics and Photonics, pp. 281–291.

Onsager, T.G. et al. (2002). "Radiation belt electron flux dropouts: Local time, radial, and particle-energy dependence". In: *Journal of Geophysical Research: Space Physics,* 107,A11.

Orlova, K. and Y.Y. Shprits (2014). "Model of lifetimes of the outer radiation belt electrons in a realistic magnetic field using realistic chorus wave parameters". In: *Journal of Geophysical Research: Space Physics,* 119,2, pp. 770–780.

Orlova, K., M. Spasojevic, and Y.Y. Shprits (2014). "Activity-dependent global model of electron loss inside the plasmasphere". In: *Geophysical Research Letters,* 41,11, pp. 3744–3751.

Ozeke, L.G. et al. (2012). "ULF wave derived radiation belt radial diffusion coefficients". In: *Journal of Geophysical Research: Space Physics,* 117,A4.

Ozeke, L.G. et al. (2019). "The March 2015 superstorm revisited: Phase space density profiles and fast ULF wave diffusive transport". In: *Journal of Geophysical Research: Space Physics,* 124,2, pp. 1143–1156.

Ozeke, L.G. et al. (2020). "Rapid outer radiation belt flux dropouts and fast acceleration during the March 2015 and 2013 storms: the role of ultra-low frequency wave transport from a dynamic outer boundary". In: *Journal of Geophysical Research: Space Physics,* 125,2.

Park, C.G. (1974). "Some features of plasma distribution in the plasmasphere deduced from Antarctic whistlers". In: *Journal of Geophysical Research,* 79,1, pp. 169–173.

Pinto, V.A. et al. (2020). "On the confinement of ultrarelativistic electronremnant belts to low L-shells". In: *Journal of Geophysical Research: Space Physics,* 125,1.

Podladchikova, T.V. et al. (2014a). "Noise statistics identification for Kalman filtering of the electron radiation belt observations: 2. Filtration and smoothing". In: *Journal of Geophysical Research: Space Physics,* 119,7, pp. 5725–5743.

Podladchikova, T.V. et al. (2014b). "Noise statistics identification for Kalman filtering of the electron radiation belt observations I: Model errors". In: *Journal of Geophysical Research: Space Physics,* 119,7, pp. 5700–5724.

Qin, M. et al. (2019). "Investigating loss of relativistic electrons associated with EMIC waves at low L values on 22 June 2015". In: *Journal of Geophysical Research: Space Physics,* 124,6, pp. 4022–4036.

Reeves, G.D. et al. (1998a). "The global response of relativistic radiation belt electrons to the January 1997 magnetic cloud". In: *Geophysical Research Letters*, 25,17, pp. 3265–3268.

Reeves, G.D. et al. (1998b). "The relativistic electron response at geosynchronous orbit during the January 1997 magnetic storm". In: *Journal of Geophysical Research: Space Physics*, 103,A8, pp. 17559–17570.

Reeves, G.D. et al. (2003). "Acceleration and loss of relativistic electrons during geomagnetic storms". In: *Geophysical Research Letters*, 30,10.

Reeves, G.D. et al. (2013). "Electron acceleration in the heart of the Van Allen radiation belts". In: *Science*, 341,6149, pp. 991–994.

Rodriguez, J.V. (2014a). "GOES 13-15 MAGE/PD pitch angles algorithm theoretical basis document, version 1.0". In: *NOAA Nat. Geophys. Data Center*.

— (2014b). "GOES EPEAD science-quality electron fluxes algorithm theoretical basis document". In: *NOAA Nat. Geophys. Data Center*.

Roederer, J.G. (1967). "On the adiabatic motion of energetic particles in a model magnetosphere". In: *Journal of Geophysical Research*, 72,3, pp. 981–992.

Roederer, J.G. and H. Zhang (2016). *Dynamics of magnetically trapped particles*. Springer.

Rothwell, P. and C.E. McIlwain (1960). "Magnetic storms and the Van Allen radiation belts–Observations from satellite 1958ε (Explorer IV)". In: *Journal of Geophysical Research* 65,3, pp. 799–806.

Russell, C. T., J. G. Luhmann, and R. J. Strangeway (2016). *Space physics: an introduction*. Cambridge University Press.

Santolík, O. et al. (2003). "Spatio-temporal structure of storm-time chorus". In: *Journal of Geophysical Research: Space Physics*, 108,A7.

Scherliess, L. et al. (2004). "Development of a physics-based reduced state Kalman filter for the ionosphere". In: *Radio Science*, 39,1, pp. 1–12.

Scherliess, L. et al. (2006). "Utah State University global assimilation of ionospheric measurements Gauss-Markov Kalman filter model of the ionosphere: Model description and validation". In: *Journal of Geophysical Research: Space Physics*, 111,A11.

Schiller Q .and Li, X. et al. (2012). "A parametric study of the source rate for outer radiation belt electrons using a Kalman filter". In: *Journal of Geophysical Research: Space Physics* 117,A9.

Schulz, M. and L.J. Lanzerotti (1974). *Particle diffusion in the radiation belts*. Vol. 7. Springer Science & Business Media.

Sckopke, N. (1966). "A general relation between the energy of trapped particles and the disturbance field near the Earth". In: *Journal of Geophysical Research*, 71,13, pp. 3125–3130.

Selesnick, R.S. (2015). "High-energy radiation belt electrons from CRAND". In: *Journal of Geophysical Research: Space Physics*, 120,4, pp. 2912–2917.

Selesnick, R.S. and J.B. Blake (1997). "Dynamics of the outer radiation belt". In: *Geophysical Research Letters*, 24,11, pp. 1347–1350.

— (1998). "Radiation belt electron observations following the January 1997 magnetic cloud event". In: *Geophysical Research Letters*, 25,14, pp. 2553–2556.

Selesnick, R.S., M.D. Looper, and R.A. Mewaldt (2007). "A theoretical model of the inner proton radiation belt". In: *Space Weather*, 5,4.

Sheeley, B.W. et al. (2001). "An empirical plasmasphere and trough density model: CRRES observations". In: *Journal of Geophysical Research: Space Physics*, 106,A11, pp. 25631–25641.

Shprits, Y.Y., L. Chen, and R.M. Thorne (2009). "Simulations of pitch angle scattering of relativistic electrons with MLT-dependent diffusion coefficients". In: *Journal of Geophysical Research: Space Physics*, 114,A3.

Shprits, Y.Y., M. Daae, and B. Ni (2012). "Statistical analysis of phase space density buildups and dropouts". In: *Journal of Geophysical Research: Space Physics*, 117,A1.

Shprits, Y.Y., N.P. Meredith, and R.M. Thorne (2007). "Parameterization of radiation belt electron loss timescales due to interactions with chorus waves". In: *Geophysical Research Letters*, 34,11.

Shprits, Y.Y. and B. Ni (2009). "Dependence of the quasi-linear scattering rates on the wave normal distribution of chorus waves". In: *Journal of Geophysical Research: Space Physics*, 114,A11.

Shprits, Y.Y., D. Subbotin, and B. Ni (2009). "Evolution of electron fluxes in the outer radiation belt computed with the VERB code". In: *Journal of Geophysical Research: Space Physics*, 114,A11.

Shprits, Y.Y. and R.M. Thorne (2004). "Time dependent radial diffusion modeling of relativistic electrons with realistic loss rates". In: *Geophysical Research Letters*, 31,8.

Shprits, Y.Y. et al. (2005). "Radial diffusion modeling with empirical lifetimes: Comparison with CRRES observations". In: *Annales Geophysicae*, 23, pp. 1467–1471.

Shprits, Y.Y. et al. (2006a). "Acceleration mechanism responsible for the formation of the new radiation belt during the 2003 Halloween solar storm". In: *Geophysical Research Letters*, 33.5.

Shprits, Y.Y. et al. (2006b). "Bounce-averaged diffusion coefficients for field-aligned chorus waves". In: *Journal of Geophysical Research: Space Physics*, 111,A10.

Shprits, Y.Y. et al. (2006c). "Outward radial diffusion driven by losses at magnetopause". In: *Journal of Geophysical Research: Space Physics*, 111,A11.

Shprits, Y.Y. et al. (2007). "Reanalysis of relativistic radiation belt electron fluxes using CRRES satellite data, a radial diffusion model, and a Kalman filter". In: *Journal of Geophysical Research: Space Physics*, 112,A12.

Shprits, Y.Y. et al. (2008). "Review of modeling of losses and sources of relativistic electrons in the outer radiation belt II: Local acceleration and loss". In: *Journal of Atmospheric and Solar-Terrestrial Physics*, 70,14, pp. 1694–1713.

Shprits, Y.Y. et al. (2013a). "Application of a new data operator-splitting data assimilation technique to the 3-D VERB diffusion code and CRRES measurements". In: *Geophysical Research Letters*, 40,19, pp. 4998–5002.

Shprits, Y.Y. et al. (2013b). "Unusual stable trapping of the ultrarelativistic electrons in the Van Allen radiation belts". In: *Nature Physics*, 9,11, p. 699.

Shprits, Y.Y. et al. (2015). "Combined convective and diffusive simulations: VERB-4D comparison with 17 March 2013 Van Allen Probes observations". In: *Geophysical Research Letters*, 42,22, pp. 9600–9608.

Shprits, Y.Y. et al. (2016). "Wave-induced loss of ultra-relativistic electrons in the Van Allen radiation belts". In: *Nature Communications*, 7, p. 12883.

Shprits, Y.Y. et al. (2017). "Multi-MeV electron loss in the heart of the radiation belts". In: *Geophysical Research Letters*, 44,3, pp. 1204–1209.

Singer, H. et al. (1996). "Monitoring space weather with the GOES magnetometers". In: *GOES-8 and Beyond*. Vol. 2812, International Society for Optics and Photonics, pp. 299–309.

Singer, S.F. (1958). "Radiation belt and trapped cosmic-ray albedo". In: *Physical Review Letters*, 1,5, p. 171.

Sorenson, H. (1985). *Kalman filtering: theory and application*. IEEE.

Southwood, D.J., J.W. Dungey, and R.J. Etherington (1969). "Bounce resonant interaction between pulsations and trapped particles". In: *Planetary and Space Science*, 17,3, pp. 349–361.

Southwood, D.J. and M.G. Kivelson (1981). "Charged particle behavior in low-frequency geomagnetic pulsations 1. Transverse waves". In: *Journal of Geophysical Research: Space Physics*, 86,A7, pp. 5643–5655.

Spasojević, M. et al. (2003). "Global response of the plasmasphere to a geomagnetic disturbance". In: *Journal of Geophysical Research: Space Physics*, 108,A9.

Spence, H. et al. (2013). "Science goals and overview of the Radiation Belt Storm Probes (RBSP) Energetic particle, Composition, and Thermal plasma (ECT) suite on NASA's Van Allen Probes mission". In: vol. 179, 1-4. Springer, pp. 311–336.

Stratton, J., R. Harvey, and G. Heyler (2012). "Mission overview for the Radiation Belt Storm Probes mission". In: *The Van Allen Probes Mission*. Springer, pp. 29–57.

Su, Z. et al. (2011). "CRRES observation and STEERB simulation of the 09 October 1990 electron radiation belt dropout event". In: *Geophysical Research Letters*, 38,6.

Su, Z. et al. (2015). "Ultra-low-frequency wave-driven diffusion of radiation belt relativistic electrons". In: *Nature Communications*, 6,1, pp. 1–8.

Subbotin, D., Y.Y. Shprits, and B. Ni (2010). "Three-dimensional VERB radiation belt simulations including mixed diffusion". In: *Journal of Geophysical Research: Space Physics*, 115,A3.

Subbotin, D.A. and Y.Y. Shprits (2009). "Three-dimensional modeling of the radiation belts using the Versatile Electron Radiation Belt (VERB) code". In: *Space Weather*, 7,10, pp. 1–15.

Sugiura, M. (1964). "Hourly values of equatorial *Dst* for the IGY." In: *Annals of the International Geophysical Year*, 35, pp. 7–45.

Summers, D., B. Ni, and N.P. Meredith (2007). "Timescales for radiation belt electron acceleration and loss due to resonant wave-particle interactions: 2. Evaluation for VLF chorus, ELF hiss, and electromagnetic ion cyclotron waves". In: *Journal of Geophysical Research: Space Physics*, 112,A4.

Summers, D. and R.M. Thorne (2003). "Relativistic electron pitch-angle scattering by electromagnetic ion cyclotron waves during geomagnetic storms". In: *Journal of Geophysical Research: Space Physics*, 108,A4.

Summers, D., R.M. Thorne, and F. Xiao (1998). "Relativistic theory of wave-particle resonant diffusion with application to electron acceleration in the magnetosphere". In: *Journal of Geophysical Research: Space Physics*, 103,A9, pp. 20487–20500.

Takahashi, K. and Y. Miyoshi (2016). "Introduction to wave-particle interactions and their impact on energetic particles in geospace". In: *Waves, Particles, and Storms in Geospace: A Complex Interplay*, pp. 35–50.

Talagrand, O. (1997). "Assimilation of observations, an introduction". In: *Journal of the Meteorological Society of Japan*, 75,1B, pp. 191–209.

Thébault, E. et al. (2015). "International Geomagnetic Reference Field: the 12th generation". In: *Earth, Planets and Space*, 67,1, p. 79.

Thorne, R.M. and R.B. Horne (1997). "Modulation of electromagnetic ion cyclotron instability due to interaction with ring current O^+ during magnetic storms". In: *Journal of Geophysical Research: Space Physics*, 102,A7, pp. 14155–14163.

Thorne, R.M. and C.F. Kennel (1971). "Relativistic electron precipitation during magnetic storm main phase". In: *Journal of Geophysical Research*, 76,19, pp. 4446–4453.

Thorne, R.M. et al. (1973). "Plasmaspheric hiss". In: *Journal of Geophysical Research*, 78,10, pp. 1581–1596.

Thorne, R.M. et al. (2010). "Scattering by chorus waves as the dominant cause of diffuse auroral precipitation". In: *Nature*, 467,7318, pp. 943–946.

Thorne, R.M. et al. (2013). "Rapid local acceleration of relativistic radiation-belt electrons by magnetospheric chorus". In: *Nature*, 504,7480, pp. 411–414.

Tsurutani, B.T. and G.S. Lakhina (1997). "Some basic concepts of wave-particle interactions in collisionless plasmas". In: *Reviews of Geophysics*, 35,4, pp. 491–501.

Tsurutani, B.T and E.J. Smith (1974). "Postmidnight chorus: A substorm phenomenon". In: *Journal of Geophysical Research*, 79,1, pp. 118–127.

Tsurutani, B.T. and E.J. Smith (1977). "Two types of magnetospheric ELF chorus and their substorm dependences". In: *Journal of Geophysical Research*, 82,32, pp. 5112–5128.

Tsyganenko, N. and M. Sitnov (2007). "Magnetospheric configurations from a high-resolution data-based magnetic field model". In: *Journal of Geophysical Research: Space Physics*, 112,A6.

Turner, D.L. and V. Angelopoulos (2016). "Extreme variability of relativistic electrons in Earth's outer radiation belt: an overview and recent revelations". In: *Waves, Particles, and Storms in Geospace: A Complex Interplay*, pp. 296–332.

Turner, D.L. et al. (2012a). "Explaining sudden losses of outer radiation belt electrons during geomagnetic storms". In: *Nature Physics*, 8,3, pp. 208–212.

Turner, D.L. et al. (2012b). "Radial distributions of equatorial phase space density for outer radiation belt electrons". In: *Geophysical Research Letters*, 39,9.

Turner, D.L. et al. (2014a). "Competing source and loss mechanisms due to wave-particle interactions in Earth's outer radiation belt during the 30 September to 3 October 2012 geomagnetic storm". In: *Journal of Geophysical Research: Space Physics*, 119,3, pp. 1960–1979.

Turner, D.L. et al. (2014b). "On the cause and extent of outer radiation belt losses during the 30 September 2012 dropout event". In: *Journal of Geophysical Research: Space Physics*, 119,3, pp. 1530–1540.

Turner, D.L. et al. (2015). "The effects of geomagnetic storms on electrons in Earth's radiation belts". In: *Geophysical Research Letters*, 42,21, pp. 9176–9184.

Turner, D.L. et al. (2017). "Investigating the source of near-relativistic and relativistic electrons in Earth's inner radiation belt". In: *Journal of Geophysical Research: Space Physics*, 122,1, pp. 695–710.

Turner, D.L. et al. (2019). "The response of Earth's electron radiation belts to geomagnetic storms: Statistics from the Van Allen Probes era including effects from different storm drivers". In: *Journal of Geophysical Research: Space Physics*, 124.2, pp. 1013–1034.

Ukhorskiy, A.Y and M.I. Sitnov (2012). "Dynamics of radiation belt particles". In: *The Van Allen Probes Mission*. Springer, pp. 545–578.

Ukhorskiy, A.Y. et al. (2006). "Impact of ULF oscillations in solar wind dynamic pressure on the outer radiation belt electrons". In: *Geophysical Research Letters*, 33,6.

Usanova, M.E. et al. (2008). "Multipoint observations of magnetospheric compression-related EMIC Pc1 waves by THEMIS and CARISMA". In: *Geophysical Research Letters*, 35,17.

Usanova, M.E. et al. (2012). "THEMIS observations of electromagnetic ion cyclotron wave occurrence: Dependence on AE, SYMH, and solar wind dynamic pressure". In: *Journal of Geophysical Research: Space Physics*, 117,A10.

Usanova, M.E. et al. (2014). "Effect of EMIC waves on relativistic and ultrarelativistic electron populations: Ground-based and Van Allen Probes observations". In: *Geophysical Research Letters*, 41,5, pp. 1375–1381.

Vainchtein, D. et al. (2018). "Evolution of electron distribution driven by nonlinear resonances with intense field-aligned chorus waves". In: *Journal of Geophysical Research: Space Physics*, 123,10, pp. 8149–8169.

Van Allen, J.A. (1959). "The geomagnetically trapped corpuscular radiation". In: *Journal of Geophysical Research*, 64,11, pp. 1683–1689.

Van Allen, J.A. et al. (1958). "Observation of high intensity radiation by satellites 1958 Alpha and Gamma". In: *Journal of Jet Propulsion*, 28,9, pp. 588–592.

Varotsou, A. et al. (2005). "Simulation of the outer radiation belt electrons near geosynchronous orbit including both radial diffusion and resonant interaction with whistler-mode chorus waves". In: *Geophysical Research Letters*, 32,19.

Vernov, S.N. and A.E. Chudakov (1960). "Investigations of cosmic radiation and of the terrestrial corpuscular radiation by means of rockets and satellites". In: *Physics-Uspekhi*, 3,2, pp. 230–250.

Walt, M. (1994). *Introduction to geomagnetically trapped radiation*. Cambridge University Press.

Wang, C. et al. (2011). "The relations between magnetospheric chorus and hiss inside and outside the plasmasphere boundary layer: Cluster observation". In: *Journal of Geophysical Research: Space Physics*, 116,A7.

West, H.I., R.M. Buck, and J.R. Walton (1972). "Shadowing of electron azimuthal-drift motions near the noon magnetopause". In: *Nature Physical Science*, 240,97, pp. 6–7.

Xiang, Z. et al. (2017). "Understanding the mechanisms of radiation belt dropouts observed by Van Allen Probes". In: *Journal of Geophysical Research: Space Physics*, 122,10, pp. 9858–9879.

Xiang, Z. et al. (2018). "A statistical survey of radiation belt dropouts observed by Van Allen Probes". In: *Geophysical Research Letters*, 45,16, pp. 8035–8043.

Xiao, F. et al. (2010). "Three-dimensional simulations of outer radiation belt electron dynamics including cross-diffusion terms". In: *Journal of Geophysical Research: Space Physics*, 115,A5.

Yu, Y., J. Koller, and S. Morley (2013). "Quantifying the effect of magnetopause shadowing on electron radiation belt dropouts". In: *Annales Geophysicae*, 31,11, pp. 1929–1939.

Zhang, X.J. et al. (2017). "Contemporaneous EMIC and whistler mode waves: Observations and consequences for MeV electron loss". In: *Geophysical Research Letters*, 44,16, pp. 8113–8121.

Zhang, X.J. et al. (2019). "Nonlinear electron interaction with intense chorus waves: statistics of occurrence rates". In: *Geophysical Research Letters*, 46,13, pp. 7182–7190.